In compliance with the
Canadian Privacy Legislation
some supporting forms
may have been removed from
this dissertation.

While these forms may be included
in the document page count,
their removal does not represent
any loss of content from the dissertation.

University of Alberta

Planar Concave Grating Demultiplexers for Coarse WDM

by

Xianling Chen ©

A thesis submitted to the Faculty of Graduate Studies and Research
in partial fulfillment of the requirements for
the degree of Master of Science.

Department of Electrical and Computer Engineering

Edmonton, Alberta

Fall 2003

National Library
of Canada

Acquisitions and
Bibliographic Services

395 Wellington Street
Ottawa ON K1A 0N4
Canada

Bibliothèque nationale
du Canada

Acquisisitons et
services bibliographiques

395, rue Wellington
Ottawa ON K1A 0N4
Canada

Your file Votre référence
ISBN: 0-612-87735-3
Our file Notre référence
ISBN: 0-612-87735-3

The author has granted a non-exclusive licence allowing the National Library of Canada to reproduce, loan, distribute or sell copies of this thesis in microform, paper or electronic formats.

The author retains ownership of the copyright in this thesis. Neither the thesis nor substantial extracts from it may be printed or otherwise reproduced without the author's permission.

L'auteur a accordé une licence non exclusive permettant à la Bibliothèque nationale du Canada de reproduire, prêter, distribuer ou vendre des copies de cette thèse sous la forme de microfiche/film, de reproduction sur papier ou sur format électronique.

L'auteur conserve la propriété du droit d'auteur qui protège cette thèse. Ni la thèse ni des extraits substantiels de celle-ci ne doivent être imprimés ou aturement reproduits sans son autorisation.

Canada

University of Alberta

Library Release Form

Name of Author: *Xianling Chen*

Title of Thesis: *Planar Concave Grating Demultiplexers for Coarse WDM*

Degree: *Master of Science*

Year this Degree Granted: *2003*

Permission is hereby granted to the University of Alberta Library to reproduce single copies of this thesis and to lend or sell such copies for private, scholarly or scientific research purposes only.

The author reserves all other publication and other rights in association with the copyright in the thesis, and except as herein before provided, neither the thesis nor any substantial portion thereof may be printed or otherwise reproduced in any material form whatever without the author's prior written permission.

Date: Aug. 14, 2003

University of Alberta

Faculty of Graduate Studies and Research

The undersigned certify that they have read, and recommend to the Faculty of Graduate Studies and Research for acceptance, a thesis entitled *Planar Concave Grating Demultiplexers for Coarse WDM* submitted by *Xianling Chen* in partial fulfillment of the requirements for the degree of *Master of Science*.

Date thesis approved: Aug. 13, 2003

Abstract

Two flat field planar concave grating demultiplexers (DMUXes) are presented for Wavelength Division Multiplexing (WDM) based on concentric circles and confocal ellipses, respectively. Theoretical derivations and scalar electromagnetic simulations are given. Effects of microfabrication imperfections on grating performance are numerically analyzed.

The elliptic DMUX is designed to minimize its sensitivity to microfabrication imperfections. With double parabolic waveguide horns to flatten channel passbands, an 18-channel elliptic DMUX working on the ITU coarse WDM wavelength grid gives promising performance according to simulation.

Reactive Ion Etching (RIE) of polymers has been optimized to achieve deep, vertical and smooth sidewalls. Both the circular and elliptic DMUXes have been designed for coarse WDM applications in the 820 *nm* wavelength range with multimode optical fibers. A circular DMUX has been fabricated in BCB polymers with deep RIE, and an elliptic DMUX in PMMA polymer with the LIGA process. Preliminary test results are given.

To Hui and Daniel

Acknoledgement

I am forever indebted to my wife Hui and my son Daniel for their patience, understanding, encouragement and continuing support during the years I spent pursuing this degree. It would be totally impossible without the happiness God had given to me through them.

My sincere gratitude goes to my supervisor Dr. James N. McMullin and co-supervisor Dr. Christopher J. Haugen of TRLabs Edmonton for providing the research opportunity, for the many helpful disscusions, and for their mentoring during this program. The financial and technical resources provided by TRLabs are instrumental in carrying out this research project. Many thanks to the staff of TRLabs and my fellow graduate students in its Photonics division. Dr. Ray G. Decorby is gratefully thanked for the technical discussions offered. Also thanked are David Clegg for his help in setting up experiemental instruments, and Hue Nguyen for her help in microfabrication processing techinques. Harini Gopaluni is thanked for her help in MMI design and simulation. Sven Achenbach of the Institute of Microstructure Technology, Germany, David M. Klymyshyn and Venkat R. Subramanian of TRLabs Saskatoon are thanked for fabricating DMUX samples with the LIGA process.

I would also like to thank the other members of my examination committee, Drs. Christopher J. Backhouse and M. David Checkel, for spending time reviewing my thesis, and for the many useful corrections and suggestions.

Table of Contents

1. Introduction 1

1.1. WDM Technology 1

1.2. Coarse WDM vs. Dense WDM 3

1.3. WDM Demultiplexer Technologies 5

1.4. Objectives of the Thesis 8

1.5. Organization of the Thesis 9

2. Circular Concave Grating Demultiplexer 10

2.1. Theory of Circular Concave Grating DMUX 10

2.2. Simulation of Circular Concave Grating DMUX 12

2.3. Microfabrication Considerations 14

2.4. Device Design and Simulation Results 17

3. Microfabrication Imperfection Analysis 22

3.1. Facet Surface Roughness 23

3.2. Facet Corner Rounding 27

3.3. Grating Sidewall Tilt 29

3.4. Use of Retro-Reflecting TIR Facets 35

3.5. Etching Undercut 37

3.6. Material Index Variation 38

3.7. Summary 40

4. Elliptic Concave Grating Demultiplexer 41

4.1. Theory of Elliptic Concave Grating DMUX 41

4.1.1. Grating Facet Construction 41

4.1.2. Facet Shadowing Elimination 45

4.1.3. Maximum Grating Order 45

4.1.4. Total Number of Grating Facets Required 46

4.2. Simulation of Elliptic Concave Grating DMUX 47

4.3. Multimode Elliptic DMUX Design 50

4.4. Singlemode Elliptic DMUX Design 53

4.4.1. Basic Design 53

4.4.2. Approximate Focal Planes 56

4.4.3. Passband Optimization 58
4.5. Elliptic Grating vs. Circular Grating 61

5. Microfabrication Processing and Optimizations 63
5.1. DMUX Fabrication with Dry Etching 63
5.1.1. BCB Polymers 63
5.1.2. Processing Procedures 64
5.1.3. Optimizations of DRIE for BCB 67
5.2. DMUX Fabrication with LIGA Process 73
5.3. Summary 76

6. Test of Waveguides and Demultiplexers 78
6.1. Test Setups 78
6.2. Test Results of BCB DMUXes and Waveguides 79
6.3. Test Results of LIGA PMMA DMUXes and Waveguides 83
6.4. Summary 85

7. Conclusions and Suggestions for Future Work 86
7.1. Conclusions 86
7.2. Suggestions for Future Work 88

References 90

Appendix A. Characterization and Numerical Generation of Random Rough Surfaces 99

Appendix B. Numeric Solutions of Electromagnetic Field in Optical Waveguides 103

Appendix C. Processing Parameters for DMUX Fabrication in BCB Polymers 107

List of Tables

Table 2-1. Parameters of multimode circular CWDM DMUX..... 18

Table 3-1. Comparison of grating loss caused by individual microfabrication imperfections for multimode circular CWDM DMUX. 40

Table 4-1. Design parameters of multimode elliptic concave grating DMUX. 50

Table 4-2. Design parameters of singlemode elliptic CWDM DMUX..... 53

Table 5-1. BCB etching conditions for device testing. 72

List of Figures

Fig. 1-1. A simplified point-to-point optical WDM link. 2

Fig. 1-2. Transmission windows of SMFs (solid) and LWPFs (dashed), and the ITU recommended CWDM wavelength grid. 5

Fig. 1-3. Principles of (a) etched planar concave grating and (b) AWG. 7

Fig. 2-1. Geometry of circular concave grating DMUX. 11

Fig. 2-2. SEM picture of Al angled-sputtered on dry-etched polymer sidewalls of circular concave grating. 17

Fig. 2-3. Layout of multimode circular CWDM DMUX (solid) and with retro-reflecting TIR facets (dashed). 19

Fig. 2-4. Simulation results of multimode circular CWDM DMUX with TIR facets. 20

Fig. 2-5. Performance of multimode circular CWDM DMUX with TIR facets. 21

Fig. 3-1. Grating facets with numerically generated surface roughness (solid) compared to original smooth facets (dashed). 24

Fig. 3-2. Effect of facet surface roughness RMS height on output field. 25

Fig. 3-3. Effect of facet surface roughness correlation length on output field. 26

Fig. 3-4. Effect of roughness RMS height on channel performance. 27

Fig. 3-5. (a) Facet corner rounding model and (b) the effect on output field. 28

Fig. 3-6. Effect of facet corner rounding on channel performance. 29

Fig. 3-7. (a) Grating facet sidewall tilt loss and (b) its equivalent EM model. 30

Fig. 3-8. Sidewall tilt loss of fundamental mode for different waveguide core thickness: comparison of EM model (solid) to Gaussian model (dotted). 32

Fig. 3-9. Sidewall tilt loss with all guided modes considered using EM model. 33

Fig. 3-10. Effect of core thickness on grating reflectivity for fundamental mode. 34

Fig. 3-11. Effect of wavelength on sidewall tilt loss for fundamental mode. 34

Fig. 3-12. Retro-reflecting TIR facets and image error on grating facets. 35

Fig. 3-13. Effect of retro-reflecting TIR facets on output field 36

Fig. 3-14. (a) Etching undercut model and (b) the effect on output field. 38

Fig. 3-15. Effect of core material index variation on output field. 39

Fig. 4-1. Geometry of elliptic concave grating DMUX. 42

Fig. 4-2. Simulation flowchart for elliptic concave grating DMUX 49

Fig. 4-3. Layout of multimode elliptic concave grating DMUX. 51

Fig. 4-4. Output fields of multimode elliptic concave grating DMUX with only fundamental modes simulated. 52

Fig. 4-5. Spectral responses of singlemode elliptic CWDM DMUX without optimization. 54

Fig. 4-6. Spectral responses of extreme and central channels on designed flat output plane (dashed) and optimized focal planes (solid) 55

Fig. 4-7. (a) Ideal algorithm and (b) approximate algorithm for channel focal point searching. 56

Fig. 4-8. Optimal focal plane tilt angles according to approximate algorithm. 57

Fig. 4-9. Double parabolic waveguide horns and field cuts at 1430 nm 59

Fig. 4-10. Field propagation of 1430 nm in double parabolic waveguide horns. 59

Fig. 4-11. Spectral responses of passband-optimized singlemode elliptic CWDM DMUX w.r.t. nominal channel wavelengths. 60

Fig. 5-1. Process procedures for circular DMUX fabricated with BCB polymers. 65

Fig. 5-2. Etching depth vs. etching time with different metal masks. 66

Fig. 5-3. Effect of etching gas composition on BCB etching rate. 68

Fig. 5-4. Effect of RIE power on BCB etching rate. 69

Fig. 5-5. BCB waveguides etched at RIE powers of 30 W (left) and 100 W (right). 69

Fig. 5-6. BCB sidewalls etched at RIE power of 100 W (left) and 200 W (right). 70

Fig. 5-7. BCB etched with $SF_6 + O_2$. 71

Fig. 5-8. BCB etched with $CF_4 + O_2$. 71

Fig. 5-9. BCB etched with $SF_6 + CF_4 + O_2$. 71

Fig. 5-10. waveguide cross-section (left), grating (middle) and sidewall surface (right) of BCB etched with Set 1 conditions. 73

Fig. 5-11. waveguide cross-section (left), grating (middle) and sidewall surface (right) of BCB etched with Set 2 conditions. 73

Fig. 5-12. waveguide cross-section (left), grating (middle) and sidewall surface (right) of BCB etched with Set 3 conditions. 73

Fig. 5-13. LIGA version 1 process: cracks in PMMA. 74

Fig. 5-14. waveguide cross-section (left), grating (middle) and sidewall surface (right) of PMMA fabricated with LIGA version 1 process. 75

Fig. 5-15. LIGA version 2 process: small cracks in the joints between waveguides and slab region. 75

Fig. 5-16. LIGA version 2 process: waveguide moved due to poor adhesion. 76

Fig. 6-1. Test setup for circular concave grating DMUX chracterization. 78

Fig. 6-2. Insertion loss of BCB waveguides etched with Set 2 conditions. 80

Fig. 6-3. Insertion loss of BCB waveguides etched with Set 3 conditions. 81

Fig. 6-4. Waveguide insertion loss vs. input wavelength for 0.64 cm long BCB waveguide etched with Set 2 conditions.....82

Fig. 6-5. Insertion loss of LIGA PMMA waveguides.....83

Fig. 6-6. Circular DMUX fabricated with LIGA version 2 process under testing.....84

Fig. 7-1. Spectral responses of multimode elliptic concave grating DMUX with 50 μm (dashed) and 100 μm (solid) LIGA PMMA resist thickness, with only fundamental mode considered. 89

Fig. A-1. An example of random rough surface generated with spectral method. 102

Fig. B-1. Geometry of elliptic grating DMUX used for field calculation..... 104

List of Abbreviations

Al	Aluminum
Au	Gold
AWG	Arrayed Waveguide Grating
BCB	Benzocyclobutene
BPM	Beam Propagation Method
CAD	Computer Aided Design
Cl	Chlorine
Cr	Chromium
CWDM	Coarse WDM
DFB	Distributed Feed-Back
DFT	Discrete Fourier Transform
DI	de-ionized
DMUX	demultiplexer
DRIE	Deep RIE
DWDM	Dense WDM
ECR	Electron Cyclotron Resonance
EDFA	Erbium-Doped Fiber Amplifier
F	Fluorine
FBG	Fiber Bragg Grating
FOM	Figure of Merit
FSR	Free Spectral Region
ICP	Inductively Coupled Plasma
IR	Infrared

ITU	International Telecommunication Union
LED	Light Emitting Diode
LIGA	German acronym for x-ray lithography (x-ray lithographie), electrodeposition (galvanoformung) and molding (absormetchnik)
LWPF	Low Water Peak Fiber
MEMS	Micro-Electro-Mechanic System
MMF	MultiMode Fiber
MMI	MultiMode Interference
MON	Metropolitan Optical Network
MUX	multiplexer
NA	Numerical Aperture
PDL	Polarization Dependent Loss
PECVD	Plasma Enhanced Chemical Vapor Deposition
PLC	Planar Lightwave Circuit
PMMA	poly(methylmethacrylate)
POF	Plastic Optical Fiber
RIE	Reactive Ion Etching
RMS	Root Mean Square
SDH	Synchronous Digital Hierarchy
SDM	Space Division Multiplexing
SEM	Scanning Electron Microscope
SMF	SingleMode Fiber
SONET	Synchronous Optical Network

TDM	Time Division Multiplexing
TE	Transverse Electric
Ti/Au	Titanium/Gold
TIR	Total Internal Reflection
TM	Transverse Magnetic
TTF	Thin Film Filter
UV	Ultra-Violet
VCSEL	Vertical Cavity Surface Emitting Laser
WDM	Wavelength Division Multiplexing
WWDM	Wide WDM

1. Introduction

1.1. WDM Technology

Since the invention of low attenuation glass optical fibers in the 1970s, fiber optical communication has experienced several revolutions fueled by the Synchronous Optical Network/Synchronous Digital Hierarchy (SONET/SDH), the invention of Erbium-Doped Fiber Amplifiers (EDFAs), and the development of Wavelength Division Multiplexing (WDM) technology [1]. Optical fibers are now the dominant carrier media in long haul transport networks, and are expected to eventually penetrate into metropolitan and access networks.

Higher capacity and lower cost are the main motivations that drive optical network revolutions. One approach to increase optical network capacity is to increase the modulation frequencies of Time Division Multiplexing (TDM) optical signals. TDM works well up to OC-192 (10 *Gbit/s*) or higher at which point cost and fiber dispersion become major concerns. Space Division Multiplexing (SDM) using arrayed fiber links is not a sustainable solution because of the linearly proportional increase in network cost. An attractive characteristic of optical fibers is that optical signals at different optical wavelengths traveling down the same fiber do not interfere with each other under normal conditions when nonlinear effects such as four-wave mixing can be ignored. This has led to the use of WDM as a cost-effective solution to the exponential increase in demands for communication bandwidth in the last decade.

Other important potential benefits to be explored with all-optical WDM networks include dynamic provisioning, data transparency and network flexibility offered by wavelength-based switching. For the sake of simplicity, Fig. 1-1 shows a point-to-point optical link using WDM technology. A number, n, of optical signals with different wavelengths are combined into a single optical fiber using a wavelength multiplexer (MUX). These wavelengths travel through the fiber independently and, if necessary, can be amplified by a common optical amplifier,

usually an EDFA. At the receiving end, a wavelength demultiplexer (DMUX) splits the wavelengths and routes them to their respective destinations. Assuming each wavelength channel works at the same transmission speed, this n channel WDM link increases total link capacity by a factor of n compared to a single wavelength link at the same speed. System cost increases but with a factor much smaller than n, because the fiber and the amplifier need not to be multiplied by n. In long haul optical networks where total network cost is dominated by outdoor facilities such as right-of-way estate and the deployment of new fiber cables instead of in-office terminal equipment, capacity upgrading through WDM is a cost-effective solution.

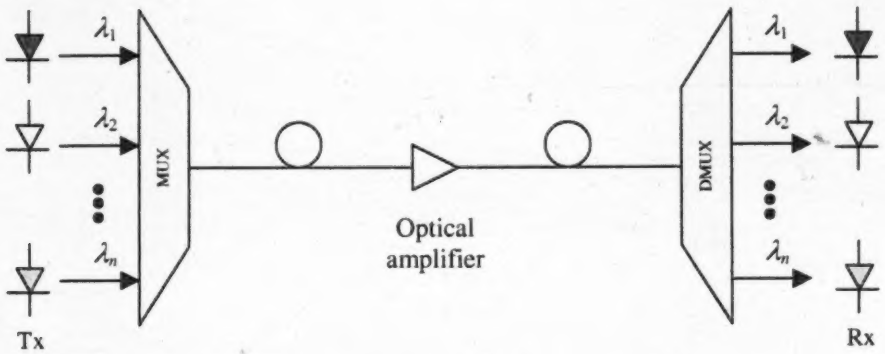

Fig. 1-1. A simplified point-to-point optical WDM link.

Historically, the two low attenuation windows of legacy fibers at 1310 *nm* and 1550 *nm* were used to transmit upstream and downstream broadcasting signals in a single fiber. Multiplexing with a few other wavelengths had also been used, especially in early CATV systems [2]. This is the first version of WDM technology and is now often referred to as Wide WDM (WWDM). Multiplexing with closely spaced wavelength channels had long been tested in laboratories but did not gain massive field deployments until late 1990s due to the lack of low cost and high performance optical components, and the fact that there was still much room for improvement with TDM. The explosion of Internet traffic in the late 90s pushed for wider deployment of Dense WDM (DWDM) optical networks. Today DWDM systems with channel spacing from 50 *GHz* to 200 *GHz* have been

standardized [3] and are commercially available. Researchers are working toward even denser multiplexing at 25 *GHz* and below.

Since WDM is essentially a frequency division multiplexing in the optical frequency domain, the International Telecommunication Union (ITU) recommendation ITU G.694.1 [3] specifies the DWDM wavelength channel grid in frequencies referenced to 193.100 *THz* (1552.524 *nm* in glass) and with channel spacing at 12.5 *GHz*, 25 GHz, 50 *GHz*, 100 *GHz* and above, respectively. Translation between frequency and wavelength grids can be obtained easily from the basic relationship between optical wavelength λ and frequency ν,

$$\lambda = c/\nu, \tag{1-1}$$

where c is the light speed in vacuum. For Coarse WDM (CWDM), channel spacing is specified in wavelength as described later.

1.2. Coarse WDM vs. Dense WDM

With the boom of DWDM in long haul optical networks in recent years, current bottleneck and focus are in metropolitan and access networks. Though not a standard definition, Metropolitan Optical Networks (MONs) are usually defined as optical networks spanning distances up to several hundred kilometers, serving large metropolitan centers. They act as the bridge between long haul and access networks. For MON and other shorter haul applications such as Ethernet, CATV, optical interconnection and so on, total network cost is dominated by terminal equipment. With the current lack of integration and methods of mass production of optical components, DWDM proves to be expensive to apply.

Lower cost can be achieved with CWDM where channel wavelength spacing is relaxed to tens of nanometers. The saving comes from the following advantages associated with the relaxed channel spacing:

- Uncooled lasers can be used in CWDM. Laser wavelength drift with temperature and age, and relaxed wavelength tolerance in laser manufacture

can all be accommodated with the wide channel spacing. The removal of temperature stabilization units of diode lasers reduces transmitter cost through the saving in thermoelectric cooling units and control circuitry, and eases packaging. Relaxed wavelength tolerance also enhances laser manufacture yield. The cost of a CWDM laser is estimated to be 1/3 of that for DWDM [4]. Low cost Light Emitting Diodes (LEDs) may also be used in some very short haul applications using MultiMode Fibers (MMFs).

- Low cost MUX/DMUX passive optical components can be used. This is especially true for Thin Film Filters (TFFs) that are made by precisely depositing over 100 layers of dielectric films for DWDM applications. Fewer layers need to be deposited for CWDM filters and thus yield can be enhanced and cost reduced. The cost of a TFF for CWDM is estimated to be half of that for DWDM [4].
- The cost of electronics for transmitter and receiver terminals can also be greatly reduced when moving from DWDM to CWDM.

Wider channel spacing means lower cost for optical components. However, there will be fewer channels that can be squeezed into the low attenuation windows of optical fibers. To provide adequate capacity, more fiber links might be needed and this increases total cost. Also a filter's Figure of Merit (FOM), defined as the ratio of its channel passband width to its skirt width, will be more expensive to achieve either with TFFs or other filter technologies. An optimal channel spacing of 20-25 *nm* exists according to practical economic considerations of total network cost [5]. To increase the number of available channels with certain channel wavelength spacing, the water peak in the E-band of conventional SingleMode Fibers (SMFs) can be eliminated, as shown in Fig. 1-2. Low Water Peak Fibers (LWPFs) are specified by ITU G.652.C and are commercially available (such as Lucent AllWave® fibers).

The CWDM wavelength grid is specified in wavelength rather than frequency as in DWDM. This is due to the fact that the most likely candidates for CWDM light sources in MONs, Distributed Feed-Back (DFB) lasers and Vertical

Cavity Surface Emitting Lasers (VCSELs), both have a thermal wavelength drift of ~ 0.1 *nm/°C*, independent of the emitted wavelength. Based on the availability of LWPFs, ITU G.694.2 [6] recommends a CWDM wavelength grid consisting of 18 channels from 1270 *nm* to 1610 *nm* spaced at 20 *nm*, covering O, E, S, C and L bands as shown in Fig. 1-2. With an outside operating temperature variation of ±50 *°C* which gives a thermal drift of ±5 *nm*, and ±(1-2) *nm* wavelength tolerance for laser manufacture, a ±(6-7) *nm* channel passband is also specified.

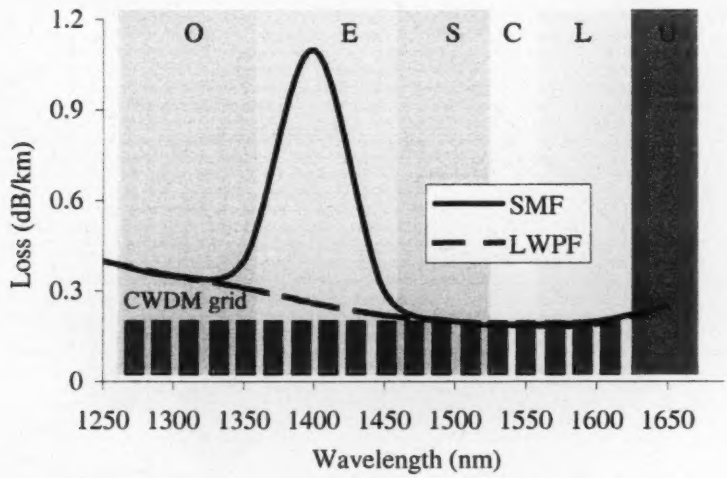

Fig. 1-2. Transmission windows of SMFs (solid) and LWPFs (dashed), and the ITU recommended CWDM wavelength grid.

Although standards have not been set, research is also active on CWDM with wavelengths in the range from 780 *nm* to 900 *nm* where VCSELs are commercially available. For low cost very short haul applications using Plastic Optical Fibers (POFs) or MMFs, CWDM with wavelengths in the transmission windows of POFs or MMFs and with available LEDs and lasers emitting at 460 *nm*, 520 *nm*, 650 *nm* and 850 *nm* ranges can also be used.

1.3. WDM Demultiplexer Technologies

MUXes and DMUXes are basic and critical components used in WDM. Wavelength multiplexing can be achieved with fused fiber couplers, or

wavelength DMUXes used in reverse in some cases. Many technologies have been considered for DMUXes [7], including TFFs, Fiber Bragg Gratings (FBGs), bulk gratings, etched planar concave gratings and Arrayed Waveguide Gratings (AWGs).

Both TFFs and FBGs are sequential components in the sense that they filter wavelengths one by one. Despite excellent channel efficiency, channel isolation and polarization insensitivity characteristics, lack of integration raises concerns of packaging, cost and reliability. FBGs are fiber compatible and can be easily coupled to optical fibers. Miniaturized bulk gratings are broadband in nature and have competitive characteristics as TFFs and FBGs, but share the similar drawbacks as well: labor intensive manufacture, complicated packaging and low reliability. Optical aberration is difficult to control in bulk gratings, but is less an issue in etched planar concave gratings and AWGs since grating facet geometry and waveguide length can be individually and precisely controlled and adjusted in photomask design with Computer Aided Design (CAD) tools.

Etched planar concave grating DMUXes are based on light diffraction from reflective gratings, as schematically shown in Fig. 1-3 (a). The grating facets serve both the functions of light diffraction and focusing. Light from the input waveguide is allowed to expand in the slab region until it hits the reflective facets and returns to the output waveguides. Different wavelengths form constructive interferences at different locations and are picked up by their respective waveguides or photodetectors.

For AWG shown in Fig. 1-3(b), grating facets are replaced by a series of waveguides having a constant optical path length difference between each other. The diffraction arms imitate the diffraction function of grating facets. Light is allowed to expand and focus, respectively, in the two slab regions of an AWG. Both these devices are broadband and integrated, promising for high channel count, high wavelength density, small size, low cost, easy packaging and high reliability. Planar technology also offers the potential for integration of multi-functional Planar Lightwave Circuits (PLCs).

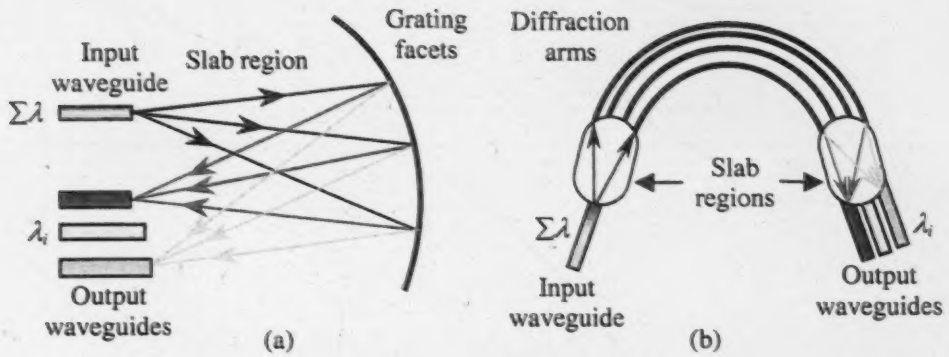

Fig. 1-3. Principles of (a) etched planar concave grating and (b) AWG.

The primary difficulty with etched planar concave gratings is the requirement for a deep, vertical and smooth etching of grating facets [8]. Grating loss increases exponentially with the tilt angle of the etched grating sidewall with respect to vertical. By replacing reflective grating facets with shallow-etched diffraction arms, AWGs ease device fabrication at the price of larger chip size, reduced fabrication yield, and extremely strict control of material and process uniformity across the wafer. The size concern is more severe when low index contrast material systems are used as required for good mode matching between optical fibers and slab waveguides. Low waveguide bending loss requires large arc radii of the diffraction arms and thus large overall chip size for AWGs.

TFF is currently the most popular technology for low channel count DWDM applications, and AWG for high channel count DWDM. Channel loss of AWGs has been pushed down to as low as 2 *dB* [9]. Etched planar concave grating DMUXes have been demonstrated on many material systems including SiO_2/Si [10], *InP/InGaAsP/InP* [11]-[13], *InGaAs/AlGaAs/GaAs* [14], $SiON/SiO_2$ [15], *InP* [16] and polymers [17]. Channel efficiencies reported to date are generally worse than 8 *dB* and not comparable with those of TFFs or AWGs.

Rowland circle [18] or its modifications and flat field spectrographs [19] are common configurations for etched planar concave grating DMUXes. In Rowland circles, the focal curve is a circle with its center at the grating pole and its radius half of the radius of the grating curve. The foci of all wavelengths are

located in a flat plane in flat field spectrographs, offering the potential to couple an array of fibers or photodetectors directly to the cleaved edge of device without input and output waveguides. Backside reflective metal coating is commonly used to enhance the reflectivity of etched grating facets. Retro-reflecting grating facets using Total Internal Reflection (TIR) have also been reported in Refs. [13] and [15] and theoretically have 100% reflectivity, as well as ease of microfabrication. However, retro-reflecting TIR facets degrade grating performance in the presence of non-vertical etched grating sidewalls, as discussed in Chapter 3 of this thesis.

Low cost is the most attractive feature of CWDM and is expected to be an important criterion in determining technology options for CWDM DMUXes. Planar integrated concave grating DMUXes with small chip size are promising for low cost, and could be a competitive technology option if channel efficiencies can be enhanced and fabrication difficulties can be solved.

1.4. Objectives of the Thesis

The objective of this thesis is to explore new planar concave grating DMUX designs targeting CWDM applications, either with SMFs as in ITU recommendation G.692.4 or with MMFs for very short haul applications in access and enterprise networks. As previously mentioned, high channel loss is the primary challenge faced by etched planar concave grating DMUXes. It is also the goal of this thesis to investigate the effects of microfabrication imperfections on grating performance, so that relative contributions from individual effects can be analyzed and new grating configurations and device designs can be devised to minimize these effects.

Since low cost is the most important requirement for CWDM optical components, polymers are proposed as low-cost material systems for the fabrication of DMUXes. Although polymers normally have thermo-optical coefficients one order of magnitude greater than those of glasses or semiconductor materials [20], channel wavelength drift with temperature is not expected to be a major concern for CWDM with wide channel spacing and flat-

top passbands. Polarization Dependent Loss (PDL) is not a concern in multimode systems and can also be accommodated by the wide channel spacing and flat-top passbands of DMUXes in singlemode cases. This is because PDL is effectively a small shift in wavelength between the Transverse Electric (TE) mode and the Transverse Magnetic (TM) mode.

Material and processing options need to be explored to find a practical fabrication solution. Optimizations of polymer dry etching process need to be carried out to achieve deep, vertical and smooth grating facets and thus maximize the performance of fabricated devices.

1.5. Organization of the Thesis

The organization of the thesis is described below. Chapter 2 presents the theory and two-dimensional scalar electromagnetic simulations of a planar concave grating DMUX based on concentric circles, together with practical considerations for microfabrication and a detailed device design for multimode applications. Chapter 3 discusses the effects of microfabrication imperfections on device performance, taking the circular DMUX described in Chapter 2 as an example. Chapter 4 presents another planar concave grating DMUX based on confocal ellipses, aiming to minimize the effects of microfabrication imperfections, especially the non-vertical etched grating facets. Again, theory and simulations are given, together with optimizations of a singlemode device designed to work on the TIU-recommended CWDM wavelength grid with flat-top passbands. Chapter 5 discusses processing techniques used to fabricate both the circular and elliptic grating DMUXes, with emphasis on achieving deep vertical etching of polymers with high-density plasma Reactive Ion Etching (RIE). Chapter 6 presents and analyzes test results of fabricated devices and waveguides. Finally, conclusions and suggestions for future work are given in Chapter 7.

2. Circular Concave Grating Demultiplexer

2.1. Theory of Circular Concave Grating DMUX

Details of the theory and simulation method for a planar concave grating DMUX based on concentric circles have been developed by McMullin and published in Ref. [21]. Here, a brief description is presented serving as references for later discussions. The circular concave grating features a flat output plane, a compact configuration and a good uniformity in channel performance.

According to geometric optics, light emanating from a point source at the center of a circle should be reflected by the circle and converges at its center. Assume that the width of the input waveguide is small compared to the radii of the circles so that a point light source approximation is valid, and that the grating facets are sections of concentric circles with the input waveguide placed at their common center O, as shown in Fig. 2-1. For light of a design wavelength λ_d to form constructive interference at the center, $\Delta R = R_{j+1}-R_j$, the difference in radii between adjacent concentric circles, must satisfy

$$\Delta R = \frac{N_g \lambda_d}{2n_1}, \tag{2-1}$$

where N_g is the grating diffraction order and n_1 is the refractive index of the core material in the slab region. The output waveguides are located on a flat output plane on the x-axis and are distributed evenly (with a center-to-center physical spacing of S_1) on both sides of the input waveguide. For the i^{th} channel with a wavelength of $\lambda_d+i\delta\lambda$, where $\delta\lambda$ is the channel wavelength spacing, to form constructive interference at the i^{th} output waveguide located iS_1 from the center O on the flat output plane, the following equation can be obtained governing the angle $\Delta\theta$ between adjacent facets after proper approximations are taken:

$$\Delta\theta = \frac{N_g \delta\lambda}{n_1 S_1}. \tag{2-2}$$

Non-overlapping of the output fields of adjacent grating orders among wavelength channels is required to minimize crosstalk between channels, and the following is obtained concerning the maximum grating order allowed:

$$N_g < \frac{\lambda_d}{\delta\lambda N_{ch}}, \tag{2-3}$$

where N_{ch} is the number of wavelength channels and the product $N_{ch}\delta\lambda$ is normally called the Free Spectral Region (FSR) of a grating.

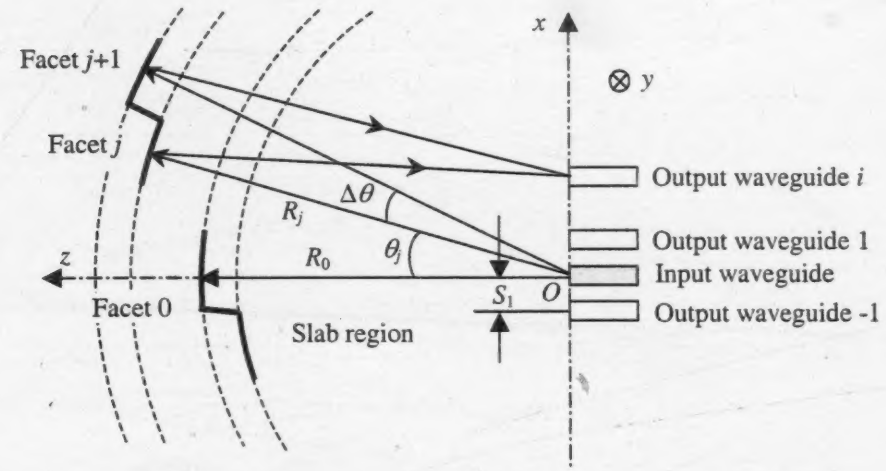

Fig. 2-1. Geometry of circular concave grating DMUX.

For CWDM applications using MMFs, the thickness H and width W of the waveguide core layer should be comparable to the core diameter of MMFs, usually 50 μm, to minimize the coupling loss caused by the dismatch in mode sizes. Hence the slab region will support multiple vertical modes with their effective mode wavelengths between λ/n_1 and λ/n_2, where n_2 is the refractive index of the cladding material. Non-overlapping of the highest order mode of a channel with the fundamental mode of its longer wavelength adjacent channel results in the following requirement for the channel wavelength spacing:

$$\delta\lambda > \lambda_i \Delta, \tag{2-4}$$

where λ_i is the channel wavelength and

$$\Delta = \frac{n_1^2 - n_2^2}{2n_1^2} \tag{2-5}$$

is the index contrast of the waveguide materials.

Once the material indices n_1 and n_2, the central facet radius R_0, the number of channels N_{ch}, the design wavelength λ_d and the channel wavelength spacing $\delta\lambda$ satisfying Eq. (2-4) are chosen, a proper grating order N_g can be selected based on Eq. (2-3), then the grating facets can be constructed with Eqs. (2-1) and (2-2). The ends of grating facet j are at R_j and $\theta_j \pm \Delta\theta/2$ from the center O so that there will be no facet shadowing.

For singlemode applications where the slab region supports the fundamental mode only, the circular concave grating can be designed with the constraint imposed by Eq. (2-4) being removed. However, only the multimode case of the circular concave grating is of interest for this thesis and is discussed below.

2.2. Simulation of Circular Concave Grating DMUX

Since polarization effects are negligible in multimode systems and grating facets are normally large compared to operating optical wavelengths, a scalar electromagnetic simulation considering TE modes only should suffice. Hard boundary conditions (zero electromagnetic fields outside the waveguide core region) can be used due to the large dimensions of the waveguides. For each wavelength, the field in the slab region can be expressed as a linear combination of the *vertical*[1] modes $\{\sin(K_m y), m = 1 \ldots M_v\}$ supported by the slab region,

$$E(x, y, z) = \sqrt{\frac{2}{H}} \sum_{m=1}^{M_v} A_m e^{i\phi_m} E_m(x, z) \sin(K_m y), \tag{2-6}$$

where $K_m = m\pi/H$, A_m and ϕ_m are the wavenumber, amplitude and phase of the m^{th} vertical mode, respectively. The maximum number of vertical slab modes M_v is

[1] *Vertical* means perpendicular to the slab and parallel to the y-axis in Fig. 2-1

determined by the thickness H and the Numerical Aperture (NA), defined as $NA \approx n_1\sqrt{2\Delta}$, of the waveguide as

$$M_v = 1 + 2NA \cdot H/\lambda, \tag{2-7}$$

The initial input field $E_m(x, 0)$ for mode m in the slab waveguide can be approximated as a linear combination of the *horizontal*[2] modes in the input waveguide, and is expressed as

$$E_m(x,0) = \sqrt{\frac{2}{W}} \sum_{n=1}^{M_h} B_n e^{i\phi_n} \sin(n\pi x/W), \tag{2-8}$$

where B_n and ϕ_n are the amplitude and phase of the n^{th} horizontal mode in the input waveguide, respectively. M_h is the maximum number of horizontal modes supported by the input waveguide and can be calculated similarly as in Eq. (2-7).

Random phases are given for the horizontal and vertical modes reflecting the incoherent nature of the LED light sources used. As in Ref. [21], the optical power distribution among modes is assumed to follow the cosine square law. Therefore,

$$A_m = \cos\left(\frac{m\pi}{2M_v}\right), \quad B_n = \cos\left(\frac{n\pi}{2M_h}\right). \tag{2-9}$$

Total power in the input waveguide is normalized so that grating efficiencies can be easily calculated.

The field at a sample point (x_g, z_g) on the grating facets is calculated using the two-dimensional Fresnel diffraction integral as

$$E_m^g(x_g, z_g) = \int E_m(x,0) \sqrt{\frac{ik_m^{eff}}{2\pi\Delta z}} \exp\left(-ik_m^{eff}\Delta z - \frac{ik_m^{eff}(\Delta x)^2}{2\Delta z}\right) dx, \tag{2-10}$$

where $\Delta x = x_g - x$, $\Delta z = z_g - z$ and

$$k_m^{eff} = \sqrt{n_1^2(2\pi/\lambda)^2 - (m\pi/H)^2} \tag{2-11}$$

---

[2] *Horizontal* means horizontal to the slab and parallel to the x-axis in Fig. 2-1.

is the effective wavenumber of the m^{th} vertical mode in the slab region. Fields on the output plane can be similarly calculated in the opposite direction with the grating field as the source.

Channel efficiency is approximately calculated as the power of the output field falling within the multimode output waveguide core region. Crosstalk is calculated as the total power of the output fields of all other channel wavelengths falling within the output waveguide core region. This approximation should be valid for multimode waveguides with large physical dimensions. A more rigorous calculation of channel efficiencies and crosstalk would take mode-coupling efficiencies into account. This can be done by first calculating the grating field and output field for each horizontal mode in the input waveguide without using the total field in Eq. (2-8), and then calculating the coupling efficiency to each horizontal mode in the channel output waveguide (other waveguides) for channel efficiency (crosstalk). These calculations would then be repeated for each vertical slab mode of each input wavelength. However, this is extremely time-consuming due to the large number of modes involved.

2.3. Microfabrication Considerations

Any design parameters (N_{ch}, λ_d, $\delta\lambda$, R_0) can be realized with the circular concave grating if facet feature size is not a concern, providing that the grating order N_g can be a positive integer according to Eq. (2-3). However, facets with a small feature size will require expensive and time consuming e-beam lithography, or become too sensitive to microfabrication imperfections such as facet corner rounding during photolithography and RIE processes. Details of the device fabrication will be discussed in Chapter 5. The requirement for a large feature size (at least a few microns based on the capacity of available facilities) and thus a reasonably low aspect ratio is especially important since a deep etching up to tens of micrometers is required for multimode devices.

The grating facet step ΔR is constant for all facets and is determined by Eq. (2-1). The width w_j of any facet j is close to w_0 of the central facet (facet 0), and can be approximated as

$$w_j \approx w_0 \approx R_0 \Delta\theta = R_0 \frac{N_g \delta\lambda}{n_1 S_1}. \tag{2-12}$$

Based on Eqs. (2-1) and (2-12), a high grating order N_g is preferred as far as facet feature size is concerned. So N_g should take the maximum integer allowed by Eq. (2-3). Combining Eqs. (2-1) and (2-12) with Eq. (2-3) where the inequality sign is replaced by the equality sign, it can then be obtained that

$$\Delta R = \frac{\lambda_d^{\,2}}{2 n_1 \delta\lambda N_{ch}}, \tag{2-13}$$

$$w_j \approx R_0 \frac{\lambda_d}{N_{ch} n_1 S_1}. \tag{2-14}$$

The following observations can be made based on Eqs. (2-13) and (2-14):

- Both the facet step ΔR and the facet width w_j increase with longer design wavelength λ_d, so it is more difficult to fabricate the circular concave grating for shorter wavelength applications. This is especially true when R_0 is large enough so that the critical dimension is associated with the facet step ΔR instead of the facet width w_j, since ΔR has a square power dependence on λ_d.
- The critical dimension is normally associated with the facet step since the facet width can be enlarged with R_0, although resulting in a larger overall chip size. Once the design wavelength λ_d and material index n_1 are determined, a maximal FSR (= $N_{ch}\delta\lambda$) is allowed for a particular critical dimension according to Eq. (2-13). For example, if the design wavelength is 820 *nm* and the core material index is 1.5, a critical dimension of 4 μm allows a FSR of only 56 *nm*. This requires either a small channel count or dense channel wavelength spacing. For CWDM, this means only a small channel count is possible under this microfabrication tolerance.

- For DWDM devices working in the 1550 *nm* range, the FSR is expanded to 200 *nm* for the same critical dimension of 4 μm. So critical dimension is not an issue for DWDM devices, which normally utilize only the 35 *nm* gain-band of EDFAs. Although a larger channel count N_{ch} is normally required for DWDM, the facet width w_j in Eq. (2-14) will not be scaled down significantly because the physical spacing S_1 of singlemode output waveguides used in DWDM devices can also be scaled down without affecting crosstalk performance.

The etched grating facets need to be coated with highly reflective metals to enhance reflectivity. Since the coating is applied on the surfaces of the deep vertical sidewalls, angled deposition (either sputtering or evaporation) is usually required. However, our trial experiments with angled sputtering of Aluminum (*Al*) proved to be of poor quality. As shown in the Scanning Electron Microscope (SEM) picture in Fig. 2-2, columnar structures with open spaces form in the sputtered *Al* thin films. It is believed that the roughness on the edge of the wet-etched dry-etch mask (*Al* in this case) is translated into the polymer sidewalls and forms microstructures due to the anisotropic nature of the dry etching process. These microstructures then serve as growth seeds in the crystallization phase during the subsequent sputtering of *Al*. The opening, more obvious in the bottom of the sidewalls, is due to the depth of the sidewalls. Test of the fabricated device shows poor reflectivity and light leaking through the facets due to the openings in the *Al* thin films.

Smooth etching is expected to reduce the microstructures but is difficult to achieve in practice. To avoid difficulties associated with the backside metal coating process, retro-reflecting facets based on TIR were used for the circular concave grating DMUX. Details of the TIR facets, their simulation method and effects on grating performance will be discussed in Chapter 3 under Section 3.4.

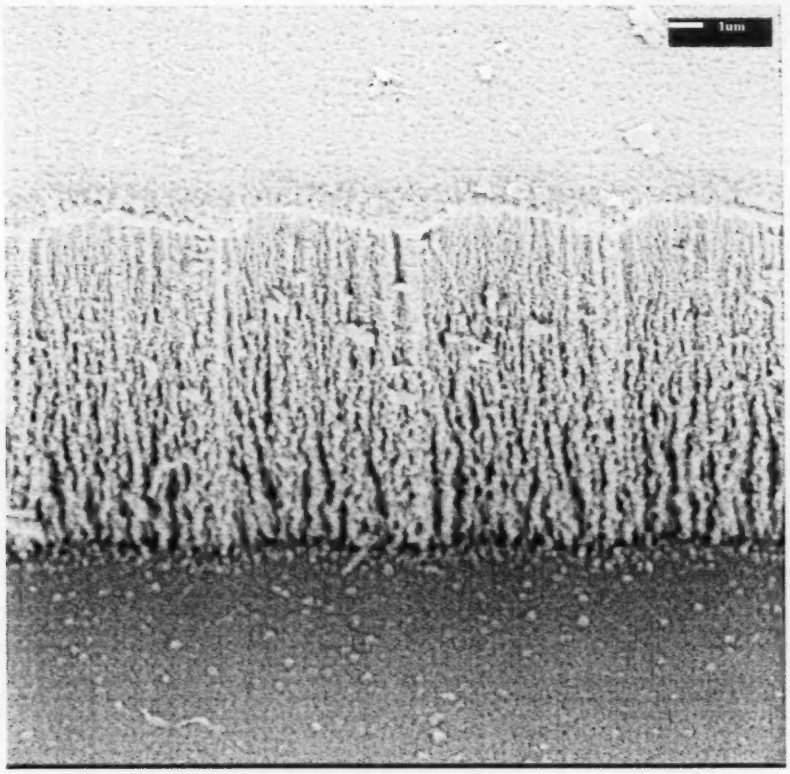

Fig. 2-2. SEM picture of Al angled-sputtered on dry-etched polymer sidewalls of circular concave grating.

2.4. Device Design and Simulation Results

The design parameters shown in Table 2-1 are chosen based on the following considerations: (1) the target applications of very short haul optical networks using MMFs and LED light sources, (2) the practical considerations of facet feature size in the previous section with a proper fabrication tolerance, and (3) the trial experiments with materials and processing, especially the capability of Deep RIE (DRIE) of polymers with available facilities. The resultant device parameters are also shown in Table 2-1. The device is designed for fabrication in Benzocyclobutene (BCB) polymers. The waveguide core and cladding materials are photosensitive BCB (Cyclotene™ 4024) polymer and dry-etch BCB polymer

(Cyclotene™ 3022), with refractive indices of 1.5435 and 1.544 at 820 *nm* wavelength, respectively.

Table 2-1. Parameters of multimode circular CWDM DMUX.

Material indices	$n_1 = 1.553$ (photo BCB), $n_2 = 1.544$ (dry-etch BCB) at 820 *nm*
Central facet radius	$R_0 = 1$ *cm*
Waveguide dimensions	$W = 50$ *μm*, $H = 10$ *μm*
Output waveguide spacing	$S_1 = 100$ *μm*
Design wavelength	$\lambda_d = 820$ *nm*
Channel wavelength spacing	$\delta\lambda = 10$ *nm*
Channel count	$N_{ch} = 4$
Grating order	$N_g = 16$
Grating facet size	$w_0 = 10.3$ *μm*, $\Delta R = 4.2$ *μm*
Number of modes supported	4 vertical slab modes, 20 horizontal modes in the input waveguide.

The resultant device layout is shown in Fig. 2-3, with the two insets showing the center and the top portions of the grating facets, respectively. The 9 *mm* long S-bends are used to expand waveguide spacing from 100 *μm* on the input/output plane to 1 *mm* on the right device edge so that an optical fiber array can be butt-coupled to the cut edge of the device using a silicon V-groove alignment chip with a standard groove-to-groove spacing of 250 *μm* (MMFs are positioned every 4 grooves). Solid lines in both insets are the designed grating facets and dashed lines are the retro-reflecting TIR facets actually used. Since the incident angle on the solid-line facet is zero, the incident angles on the retro-reflecting TIR facets are 45° and thus satisfy TIR with ambient air refractive index $n_0 = 1$. The central facet width w_0 is 10.3 *μm* as shown in the top inset. The upper end of the grating has wider facets (bottom inset) due to the longer radii R_j of the circles and the constant angle $\Delta\theta$. The lower end of the grating has narrower facets. The grating facet step is constant as can be verified in the two insets. The chip size is approximately 0.5 *cm* × 2.1 *cm*, and a 4 *in* wafer was used for photomask layout with C2V Odin™, a Micro-Electro-Mechanic System (MEMS) photomask layout CAD tool with script programming capability. The script programming is desired because it will be otherwise time consuming to layout hundreds of lines (grating facets) in arbitrary positions with manual layout.

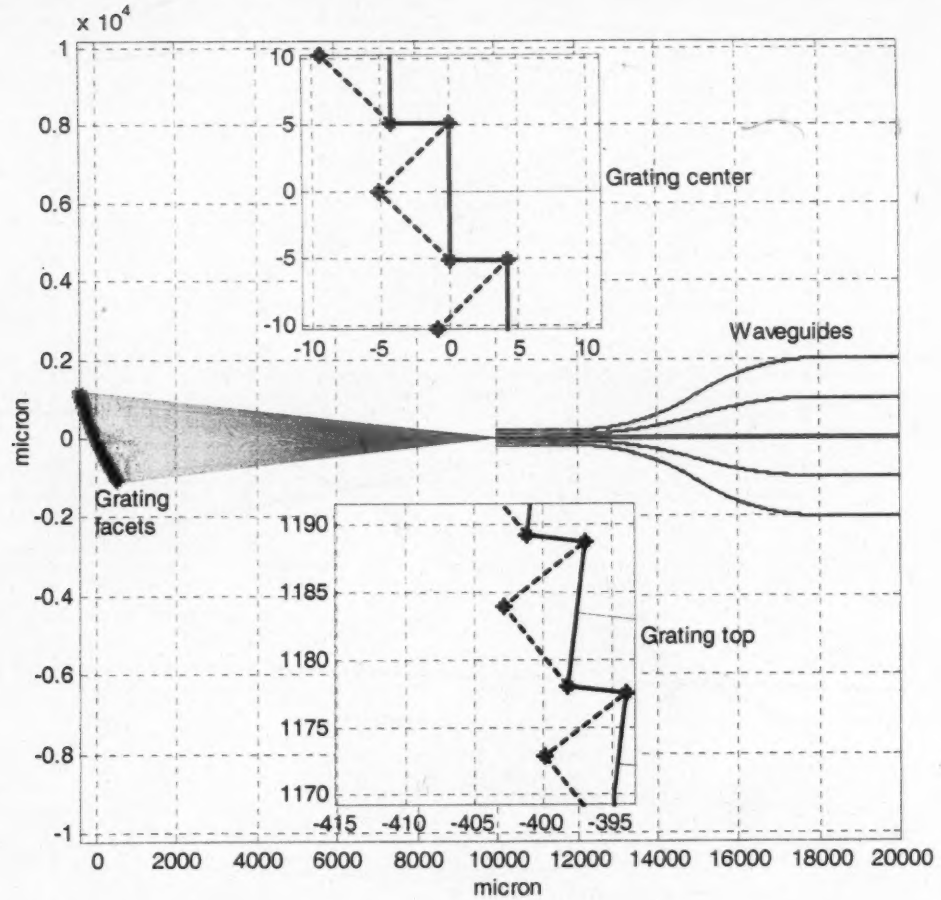

Fig. 2-3. Layout of multimode circular CWDM DMUX (solid) and with retro-reflecting TIR facets (dashed).

Simulation results are shown in Fig. 2-4 with the TIR facets used. The horizontal axis is the position relative the center *O* on the *x*-axis of Fig. 2-1. The input fields for all 4 channels overlap with each other in the central input waveguide. The output fields of the four channels with wavelengths of 840 *nm*, 830 *nm*, 810 *nm*, and 800 *nm* are shown from left to right. Because the input waveguide is placed in the center, there is no channel of the design wavelength 820 *nm*. The structures in the output fields are due to the superposition of the fields of multiple vertical slab modes. The exact field patterns change from run to run because of the random phases involved in the simulation, but the channel efficiencies and crosstalk levels were found to be near constant. For each channel,

higher order slab modes have longer effective mode wavelengths and thus their field peaks are shifted toward the left from the central position of the channel output waveguide. However, a significant portion of the output power can be captured by the 50 μm wide output waveguide.

With a design grating diffraction order of 16, the output fields of adjacent diffraction orders (orders 17 and 15) are also shown on the left and right ends of Fig. 2-4, respectively. The output field peaks of either adjacent order are located outside the fields of working order 16. Therefore, non-overlapping of grating orders is confirmed.

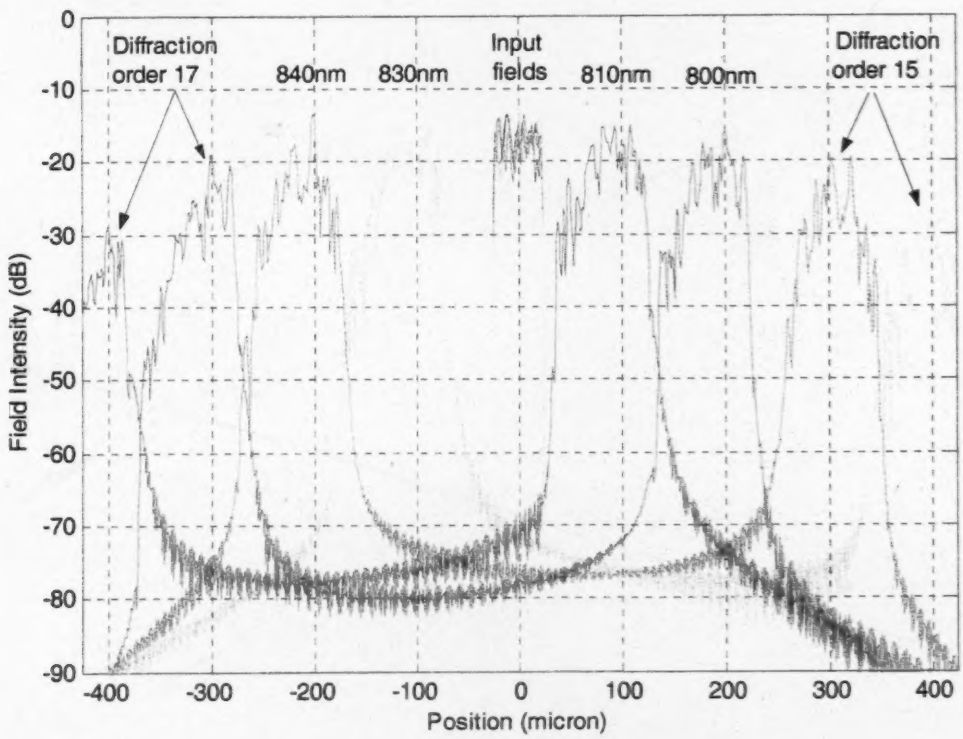

Fig. 2-4. Simulation results of multimode circular CWDM DMUX with TIR facets.

Channel efficiencies and crosstalk levels are shown in Fig. 2-5. The crosstalk levels, from both adjacent channels and non-adjacent channels, are better than 47 *dB* for all channels. The simulated channel efficiencies are between 1.5 *dB* and 3.8 *dB*. Since the adjacent diffraction orders, especially those of wavelengths 800 *nm* and 840 *nm*, have comparable field intensities as the working

order, as shown in Fig. 2-4, the lost optical power is mainly associated with these adjacent diffraction orders, as well as with those high order slab modes falling outside of the output waveguide core regions. Channel efficiencies can be slightly improved by expanding the output waveguides toward longer wavelength side, at the price of increased crosstalk levels.

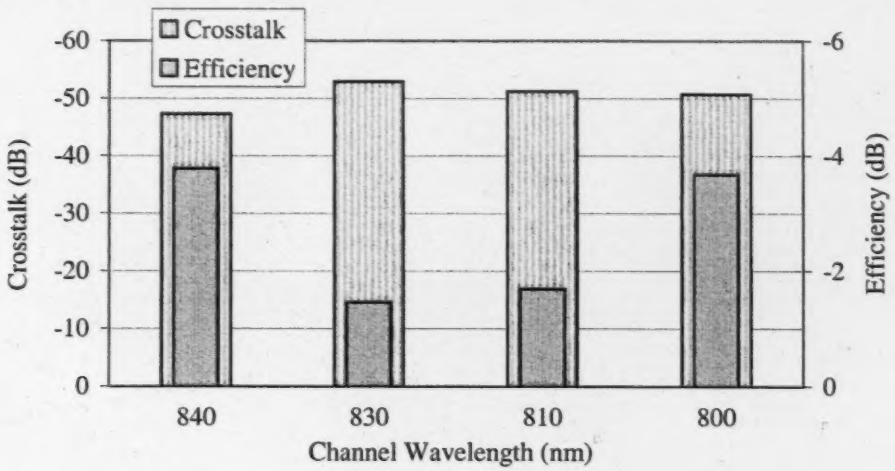

Fig. 2-5. Performance of multimode circular CWDM DMUX with TIR facets.

The simulated device performance is better than reported experimental results [10-17] for singlemode planar concave grating DMUXes, all based on Rowland circles. Although it is unfair to compare simulation results with experimental results, such a comparison provides justification to carry out further experimental work based on simulation predications.

3. Microfabrication Imperfection Analysis

Due to the presence of imperfections in microfabrication processing, both device geometry and material properties will deviate from the designed or ideal. The effects of these imperfections on device performance should be analyzed, so that a more realistic expectation for the device performance can be obtained. Of more importance, the individual contribution from each effect can be compared and optimizations can be carried out to minimize sensitivity to fabrication tolerance. In this chapter, the effect of each microfabrication imperfection is analyzed individually for the circular concave grating DMUX discussed in Chapter 2. These imperfections include grating facet surface roughness, facet corner rounding, grating sidewall tilt, use of retro-reflecting TIR facets, etching undercut and material index variation. Conclusions are then drawn as to the relative contribution from each effect and the dominant effect is identified. However, the principles and analytical methods used are applicable to other planar concave grating DMUXes in general.

Since higher order slab modes of a multimode circular concave grating DMUX act similarly to the fundamental mode except that they have longer effective mode wavelengths in the slab region and are shifted linearly on the flat output plane, for the sake of simplicity only the fundamental mode is considered in the following analysis wherever permitted. The analytical methods and conclusions drawn for the fundamental mode are equally applicable for those higher order slab modes.

The circular CWDM DMUX design shown in Table 2-1 is used as an example for the following analysis of microfabrication imperfections. Only the channel with a wavelength of 830 *nm* is analyzed, except for the analysis of grating sidewall tilt, which uses the design wavelength 820 *nm*. The results obtained are similar for other wavelength channels.

3.1. Facet Surface Roughness

Surface roughness on etched grating sidewalls causes channel loss and crosstalk. The roughness can come from two sources: roughness on the edge of the metal dry-etch mask can be translated into the grating sidewalls during DRIE; and the DRIE process itself. A deep vertical etching of the grating facets is required for low reflection loss. However, a highly anisotropic etching process faithfully translates the mask edge roughness into the etched sidewalls and results in columnar structures shown in Fig. 2-2. The mask edge roughness is usually significant for those high etching selectivity metals (such as *Al*) required to endure the deep etching process without significant mask erosion.

Rigorous theoretical treatments of light scattering caused by surface roughness for TIR waveguide turning mirrors have been reported in Ref. [22] and its references. Experimental results can be found in Ref. [23] for ruled echelle gratings and in Ref. [24] for waveguide mirrors. However, a rigorous treatment requiring significant computing resources is out of the scope of this thesis. For an approximate estimation of the surface roughness effect, a simple physical optical method [25] considering one-dimensional roughness is used. Light scattering caused by sidewall surface roughness of optical waveguides is by itself a complicated research topic and is not studied in this thesis.

In modeling the surface roughness effect, each grating facet (dashed) is replaced by a numerically generated random rough surface (solid) with a surface Root Mean Square (RMS) height *RMS* and a Gaussian correlation length *CL*. The definitions of these surface roughness parameters and the method for random rough surface generation are discussed in Appendix A. For each facet, the arithmetic average of the random rough surface is set to be the original smooth facet. This is achieved by adding the random variation to the facet radius at each facet sampling point. Fig. 3-1 shows an example of the generated grating facets with random surface roughness. An unrealistically high RMS height of 500 *nm* is used for the purpose of visualization, and a correlation length $CL = 1\ \mu m$ is used.

For the actual simulation, practically achievable RMS values less than 500 *nm* were used.

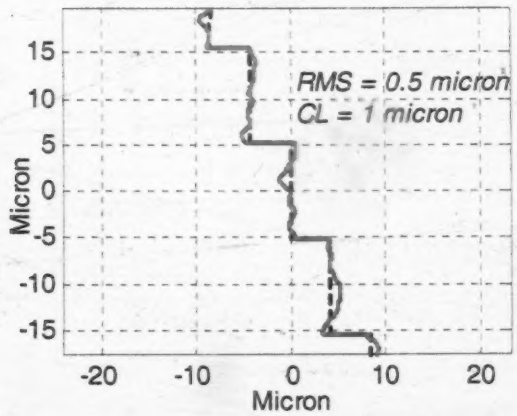

Fig. 3-1. Grating facets with numerically generated surface roughness (solid) compared to original smooth facets (dashed).

Fig. 3-2 shows the output fields of the channel with a wavelength of 830 *nm* at different surface RMS heights with a constant correlation length $CL = 1$ μm. The output field calculation range (-850 μm, +650 μm) covers the fields of the working order 16 and the two adjacent diffraction orders (orders 15 and 17). Since the facet width is around 10 μm, 31 sample points were taken on each facet to avoid aliasing effects for finite discrete sampling. This number is selected based on the Nyquist sampling theorem. It is also used for all the following simulation results in this chapter. The state of the random number generator was returned to zero before each run, so that the random pattern is repeated for all RMS heights and their output fields can be directly compared. As expected, the field peak intensity (thus grating efficiency) decreases and the side-lobe intensities (thus crosstalk) increase with increasing surface RMS height. With a normalized input power, the output powers (defined as the total power falling within the 1500 μm output field calculation range shown in Fig. 3-2) are 0.94, 0.92 and 0.52 for *RMS* of 0, 10 and 50 *nm*, respectively. With rough surfaces, light is scattered in all directions, therefore, the side-lobe intensities increase and the power falling within the output field calculation range decreases.

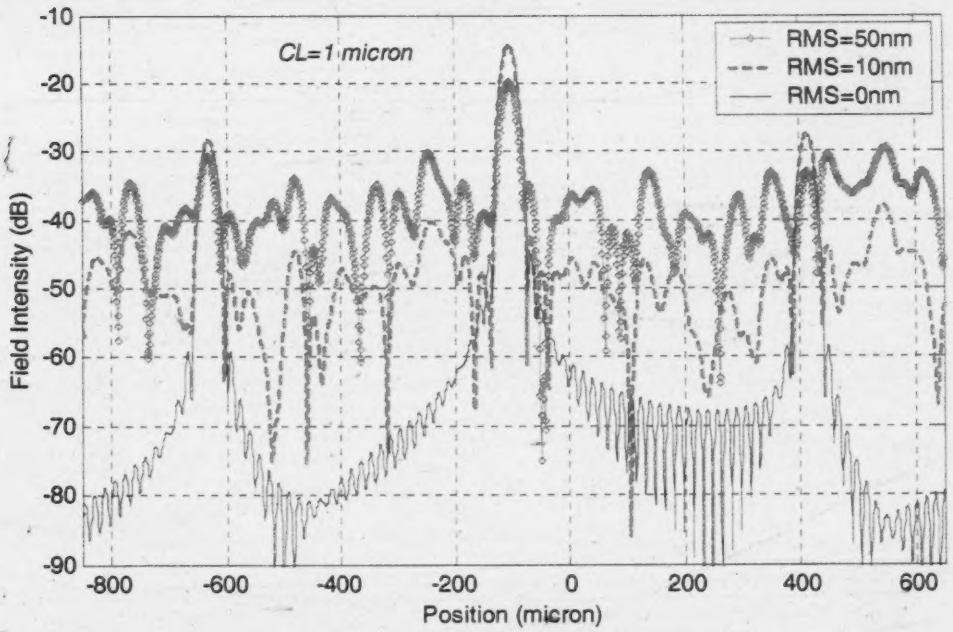

Fig. 3-2. Effect of facet surface roughness RMS height on output field.

Fig. 3-3 shows the output fields at different surface roughness correlation lengths with a constant $RMS = 20\ nm$. The correlation length is found to have much smaller effect on the output field than the RMS height, and the reason is explained below. Based on the geometry of the circular grating in Fig. 2-1, the optical path length difference between rays reflected from adjacent facets to any position x on the output plane can be expressed as

$$\Delta l \approx 2\Delta R - x\Delta\theta\,. \tag{3-1}$$

The surface roughness RMS height changes the radius difference ΔR for two points on adjacent facets and thus affects their relative phases for light interference. However, the angle $\Delta\theta$ is maintained with random variations along the radii of the facets. The angle θ of a facet point does not enter into Eq. (3-1), thus the position of a facet point on its facet curve is insignificant. Therefore, the roughness correlation length has a smaller effect on light interference and thus a smaller effect on the output field.

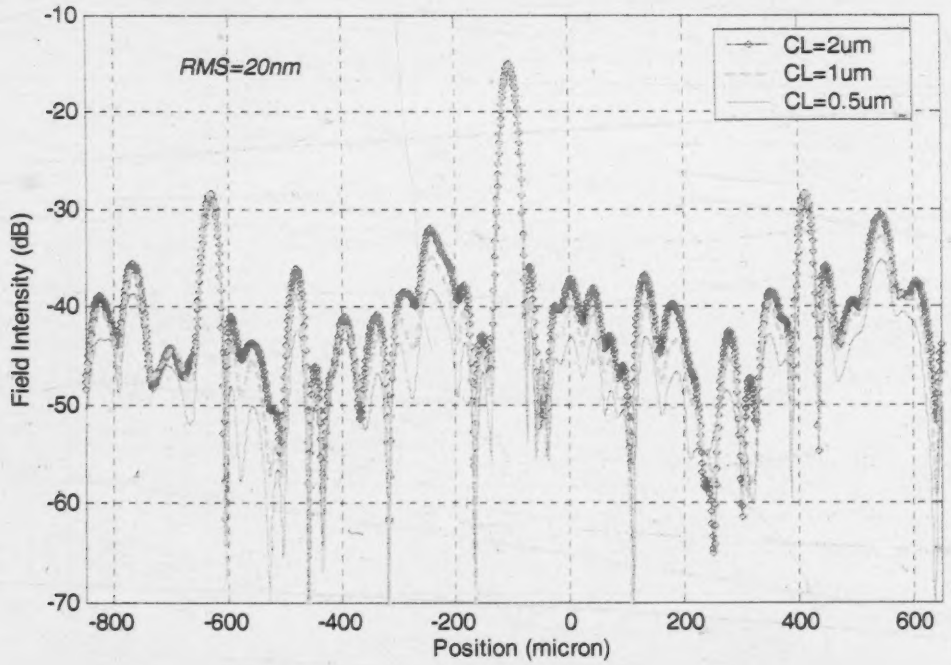

Fig. 3-3. Effect of facet surface roughness correlation length on output field.

Fig. 3-4 shows the effect of roughness RMS height on channel efficiency and the output power. For a totally random rough surface with no grating, light is reflected and scattered in all backward directions and the output power can be assumed to distribute uniformly on a semi-circle with its center at the grating center and its radius $R_0 = 1$ *cm*. The average power falling within the output field calculation range is thus $1500\mu m/(\pi R_0)$, which is the length ratio between the output field calculation range (1500 μm) and the circumference of the semi-circle (πR_0). The average power is also shown in Fig. 3-4. With a very high RMS height, the output power is expected to approach the average power. The channel efficiency decreases quickly with increasing RMS height, and reaches its first minimum at *RMS* = 110 *nm*. This agrees with the empiric rule used in grating efficiencies, which indicates that for a grating to have satisfying efficiencies the surface roughness RMS height must be well below $\lambda/10$.

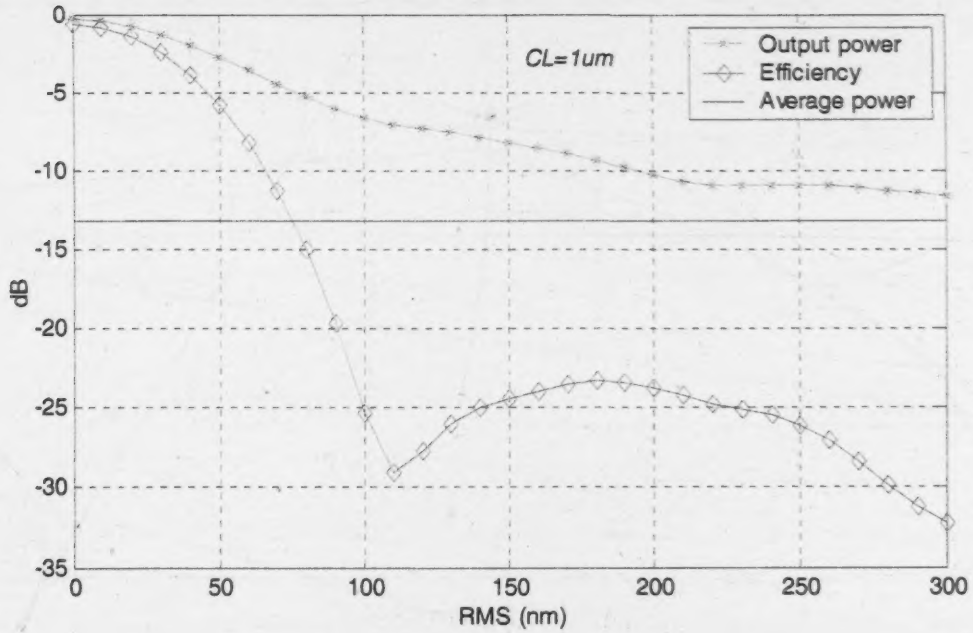

Fig. 3-4. Effect of roughness RMS height on channel performance.

3.2. Facet Corner Rounding

Corner rounding of grating facets degrades grating performance. For echelle gratings, ruling grooves with the included facet corner angles less than 90° can reduce this effect [26, 27]. This technique is applicable to planar concave gratings without retro-reflecting TIR facets. Numerical analysis of facet corner rounding has been reported in Refs. [28-30]. For etched planar concave gratings, corner rounding is the result of the imperfect photolithography and etching processes. Here we distinguish convex corners and concave corners because they tend to have different rounding rates during processing and different effects on grating performance as discussed below.

The facet corner rounding effect is modeled by rounding each facet corner geometrically with a uniform radius r as shown in Fig. 3-5(a), but concave and convex corners are analyzed separately. The effect of corner rounding on the

output field is shown in Fig. 3-5 (b). Again, only the fundamental mode of the channel with a wavelength of 830 *nm* is shown.

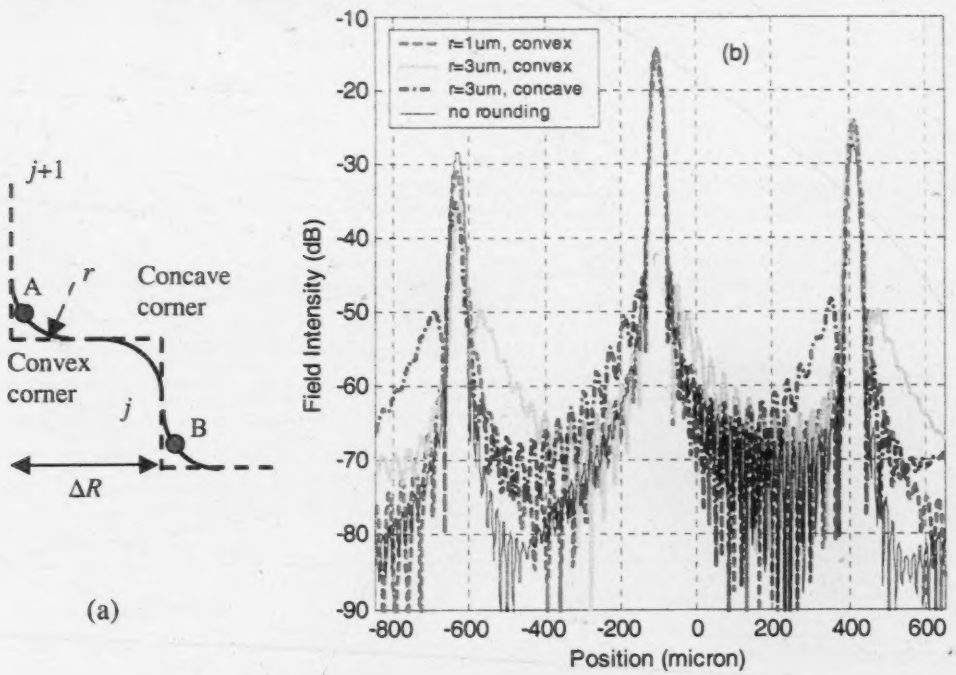

Fig. 3-5. (a) Facet corner rounding model and (b) the effect on output field.

With increasing rounding radius r, field peak intensity decreases and side-lobe intensities increase. The increase in side-lobe intensities is more significant on the right (shorter wavelength) side than on the left (longer wavelength) side for convex corner rounding, and the reverse is true for concave corner rounding. In Fig. 3-5(a), point B on the convex corner of facet j sees an increase in ΔR with respect to any point on facet j+1 above its corresponding point A, and is expected to form constructive interference of diffraction order N_g at a position with a larger x, according to Eq. (3-1). This results in increased side-lobe intensities on the right side. Similarly, point B with respect to points below point A sees a decrease in ΔR and contributes to side-lobes to the left side. However, there are more points above point A than under point A when point B is close to the bottom of facet j, where the variation of ΔR is also more significant. Therefore, the increase in side-lobe intensities is more significant on the right (shorter wavelength) side

for convex corner rounding. Similarly, more power is contributed to the side-lobes on the left (longer wavelength) side for concave corner rounding.

The effect of corner rounding on channel performance is shown in Fig. 3-6, with both the concave and convex corners rounded simultaneously with the same radius. The channel efficiency generally decreases with increasing corner rounding radius. Under normal microfabrication tolerances, this effect is less severe than the surface roughness effect. Obviously, a grating with a larger facet size is less sensitive to the corner rounding effect. Therefore, proper optimizations of a design should be taken to maximize its facet size.

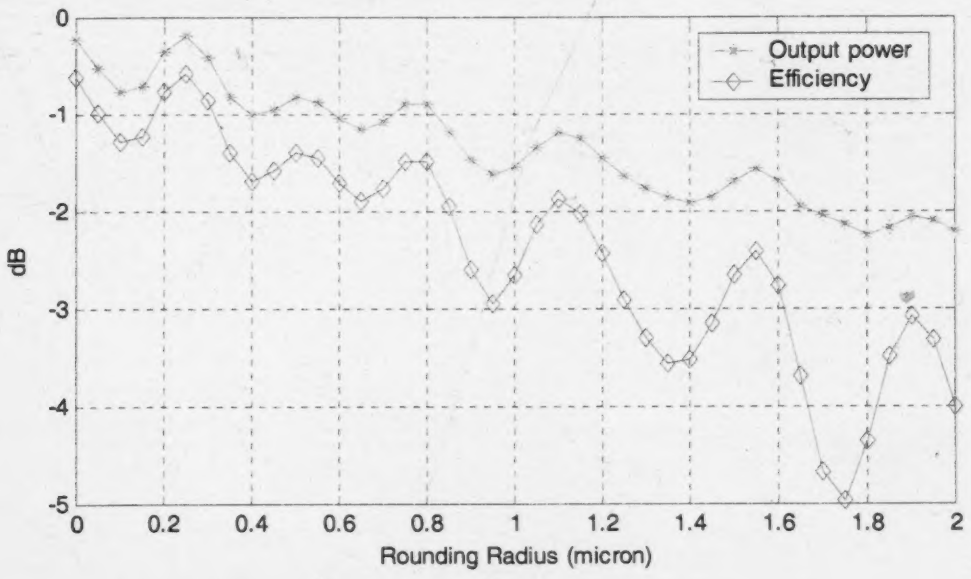

Fig. 3-6. Effect of facet corner rounding on channel performance.

3.3. Grating Sidewall Tilt

Since grating facets serve as reflective mirrors, high smoothness and verticality are required for good reflectivity. Optimizations for vertical and smooth sidewalls are only possible for certain materials even with highly anisotropic dry etching facilities and require numerous experiments. The etched

sidewall tilt angle δ can be either positive as shown in Fig. 3-7(a) or negative, depending on the material and processing details.

Based on ray theory, light incident angle at the waveguide core-cladding interface will be altered upon reflection on the tilted sidewall. It will then no longer satisfy waveguide mode angle and will result in radiation to the cladding layer, as schematically shown in Fig. 3-7(a). From an electromagnetic field point of view, this effect can be equivalently modeled as a mode-coupling problem between two identical waveguides joined with a title angle of 2δ, as shown in Fig. 3-7(b).

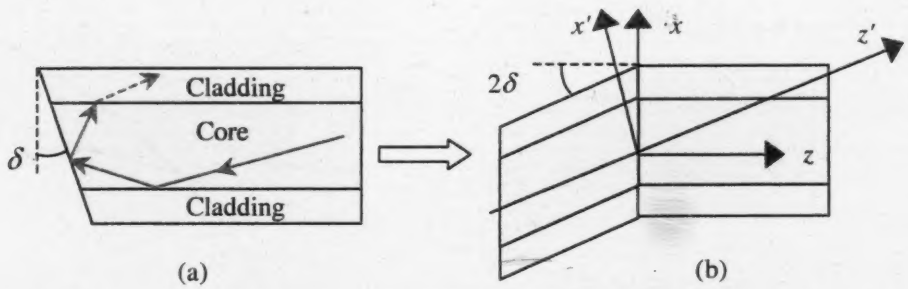

Fig. 3-7. (a) Grating facet sidewall tilt loss and (b) its equivalent EM model.

Since the coupling efficiency is highly sensitive to the actual field profile, a rigorous solution to the electromagnetic fields in the waveguides is necessary for the analysis of the sidewall tilt effect. Since only the slab waveguide is involved, a one-dimensional model is used. Vertical TE mode fields supported by the slab waveguide along the x-axis are obtained by numerically solving the slab waveguide eigenvalue equation, as detailed in Appendix B. The total field is then expressed as a linear combination of the fields of all guided modes, as in Eq. (2-6). The mode energy distribution is assumed to follow the cosine square law as in Eq. (2-9).

With the coordinate systems shown in Fig. 3-7(b), the field $E'(x)$ in the left waveguide can be expressed by rotating its coordinate system by a small angle 2δ and is

$$E'(x) = E(x)\exp\left(-i \cdot n(x) \cdot k \cdot 2\delta \cdot x\right), \tag{3-2}$$

where $n(x)$ is the material index distribution function along the x-axis, $k = 2\pi n_1/\lambda$ is the wavenumber in the slab core region, and $E(x)$ is the nominal field in the right waveguide. Using the overlap integral method, the coupling efficiency between mode m_1 in the left waveguide and mode m_2 in the right waveguide can be expressed as

$$T_{m_1-m_2} = \left| \int_{-\infty}^{+\infty} E_{m_2}(x) E'_{m_1}(x) dx \right|^2 . \tag{3-3}$$

Powers of both the fields E_{m_2} and E'_{m_1} must be normalized in the above equation. So the individual mode powers should be normalized first, and the reflection loss is then calculated as

$$Loss = 10 \log_{10} \left(\sum_{m_1=1}^{M} \left(P_{m_1} \sum_{m_2=1}^{M} T_{m_1-m_2} \right) \right), \tag{3-4}$$

where P_m is the power of mode m if the total power is normalized according to the mode power distribution law, and M is the total number of modes supported.

To verify this electromagnetic field coupling model (EM model), Fig. 3-8 compares its simulation results to those calculated with the Gaussian model [31]. Waveguide material indices are taken from Table 2-1 and the wavelength simulated is 820 *nm*. The Gaussian model is applicable to fundamental mode only because it assumes a Gaussian shaped field profile. Under this assumption, a simple analytical expression can be derived for the tilted coupling loss. For waveguides with large core layer thickness (multimode), only the coupling efficiency of the fundamental mode to itself was considered in the EM model in Fig. 3-8. For small core layer thickness (singlemode) waveguides and small sidewall tilt angles, the tilt loss increases exponentially with the tilt angle and the two models agree with each other. Discrepancies are obvious for large core thickness and large sidewall tilt angles, and are caused by the fact that the actual field profile of the fundamental mode in a multimode waveguide is no longer Gaussian shaped. These discrepancies have been reported in Ref. [32], which uses exact mode profiles and the overlap integral method as in the present EM model, but considers fundamental mode only as in the Gaussian mode.

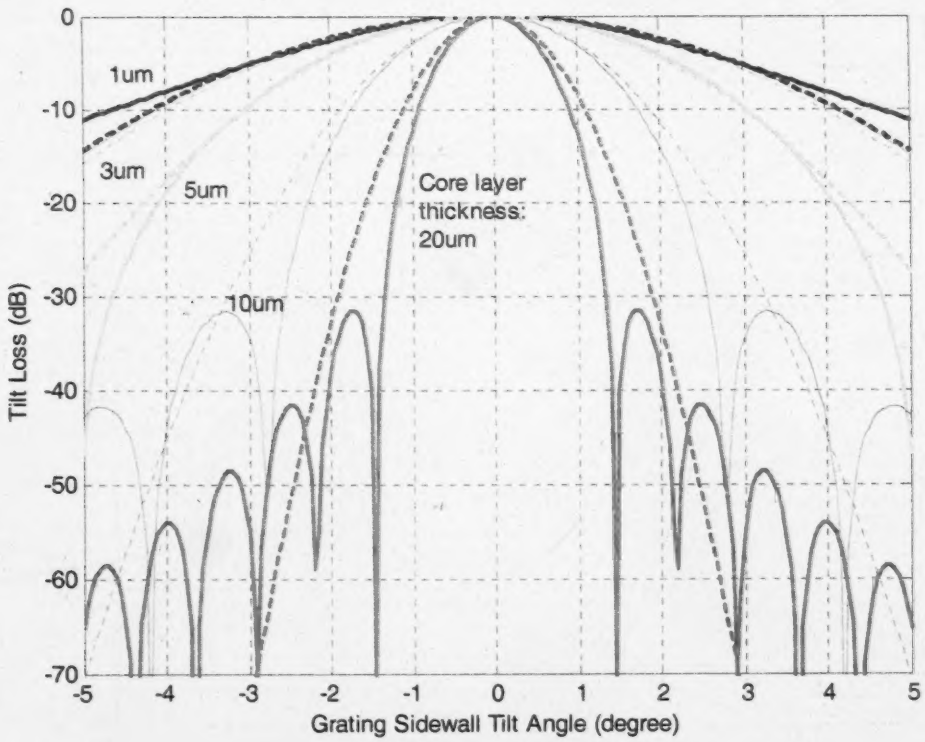

Fig. 3-8. Sidewall tilt loss of fundamental mode for different waveguide core thickness: comparison of EM model (solid) to Gaussian model (dotted).

Fig. 3-9 shows the EM model results where all guided modes are considered and the coupling between different modes are allowed. Comparing Fig. 3-9 to Fig. 3-8 for the same core thickness, it can be found that the tilt loss is much smaller when multiple modes are considered. An examination of the coupling between modes shows that with increasing tilt angle, the coupling within each mode decreases quickly as in Fig. 3-8, but the coupling between certain modes increases and thus the net loss grows at a much slower pace. For instance, for a core thickness of 5 μm which supports 4 vertical slab TE modes, it is found that the coupling from TE_0 mode to itself decreases quickly with increasing tilt angle, but the coupling from TE_0 mode to TE_2 mode increases, while those from TE_0 mode to TE_1 mode and TE_3 mode remain negligible. Therefore, as far as the sidewall tilt loss is considered, a multimode waveguide with large core layer

thickness is less demanding on the verticality of the etching process. However, it is more difficult to achieve high verticality when the etching depth is larger.

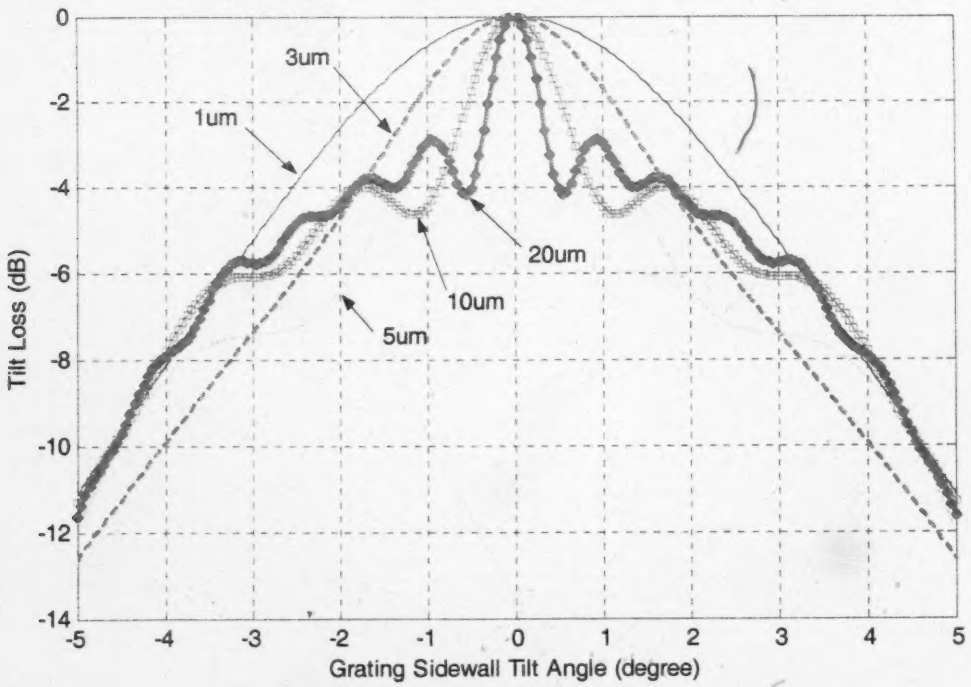

Fig. 3-9. Sidewall tilt loss with all guided modes considered using EM model.

Since the Gaussian model gives predictions close to the rigorous EM model for the fundamental mode when both the waveguide core thickness and the sidewall tilt angle are small, as shown in Fig. 3-9, a few observations based on it can be made. Fig. 3-10 plots the tilt loss of the fundamental mode as a function of the waveguide core layer thickness for different tilt angles. It is found that there is a constant optimal core layer thickness for all tilt angles, which is around 1.6 μm in this case. This optimal thickness corresponds to when the fundamental mode in the waveguides has a minimum mode size and thus is the least sensitive to the sidewall tilt effect. In principle, this optimal thickness is similar to that for waveguide bending loss explained in Ref. [33].

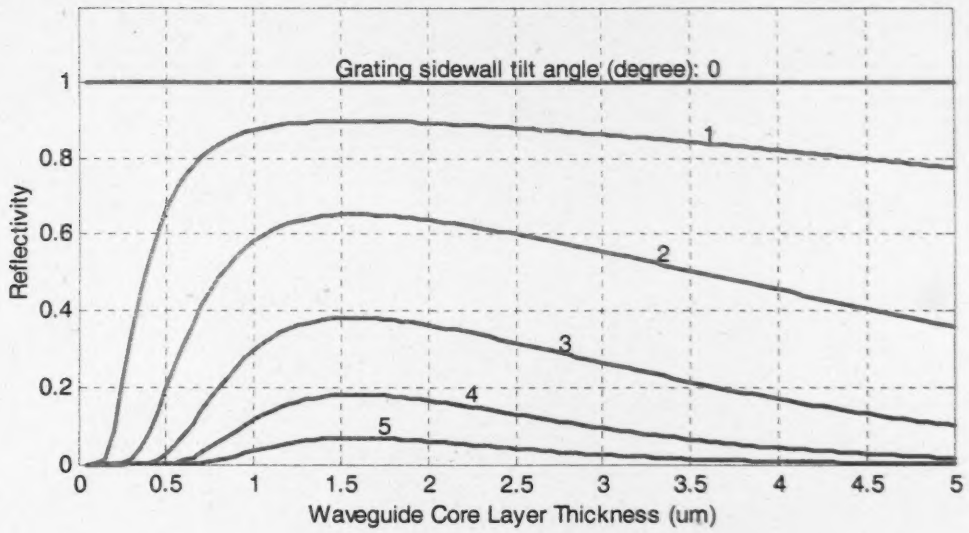

Fig. 3-10. Effect of core thickness on grating reflectivity for fundamental mode.

Fig. 3-11 plots the tilt loss of the fundamental mode at different wavelengths for a core thickness of 5 μm. For the fundamental mode, which usually possesses the largest portion of optical power among all guided modes, devices operating at longer wavelength are less sensitive to the tilt loss. Hence, it is more difficult to achieve low-loss etched planar concave grating DMUXes for applications in shorter wavelength ranges.

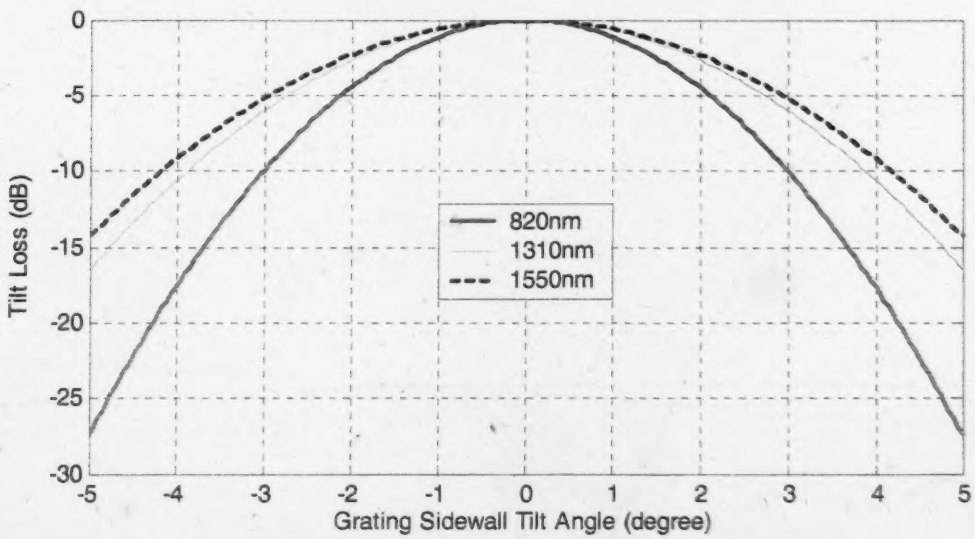

Fig. 3-11. Effect of wavelength on sidewall tilt loss for fundamental mode.

3.4. Use of Retro-Reflecting TIR Facets

Early demonstrated planar concave grating DMUXes use backside metal coating such as *Al* and Gold (*Au*) with angled sputtering or evaporation. The concept of retro-reflecting TIR facets shown in Fig. 3-12 was introduced in Refs. [13] and [15]. Two retro-reflecting facets are used to replace each original grating facet. Since light on both facets satisfies TIR, the reflectivity is 100% in theory, and there is no need to coat the grating sidewalls with reflective metals. Thus the fabrication processing is simplified and the grating efficiencies should be enhanced.

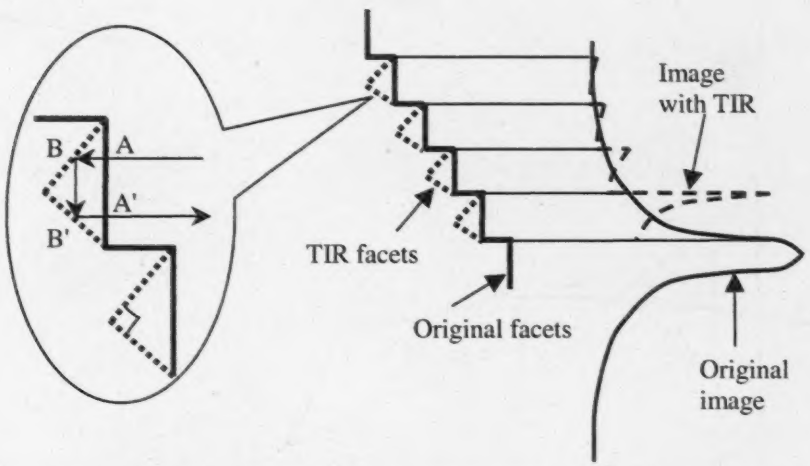

Fig. 3-12. Retro-reflecting TIR facets and image error on grating facets.

With the TIR facets, the field incident on point *A* emerges as reflection from point *A'* and vice versa. This introduces image error on facets in a similar manner as discussed in Ref. [34]. However, for the particular case of circular concave grating, the position of a point on its facet curve is insignificant according to Eq. (3-1), so this image error is not expected to degrade grating performance, as will be proved in the following simulation results. However, with two reflecting elements on each facet, the retro-reflecting TIR facets will double the grating sidewall tilt loss discussed in the previous section.

The use of the TIR facets is modeled by swapping the field at point *A* to its mirror point *A'* on the same facet *j*, and adding an extra optical path length of

w_j (width of facet j) in the grating field calculation. The path $\overline{ABB'A'}$ equals w_j, independent of A's position on facet j because of the isosceles right triangle consisting of the original facet and the two retro-reflecting TIR facets. The simulation results for the fundamental mode are shown in Fig. 3-13 for one channel. The inset shows the details of the field peaks around the channel output waveguide. The center of the channel output waveguide is designed at -100 μm but is shifted left due to the chromatic aberration of the circular grating.

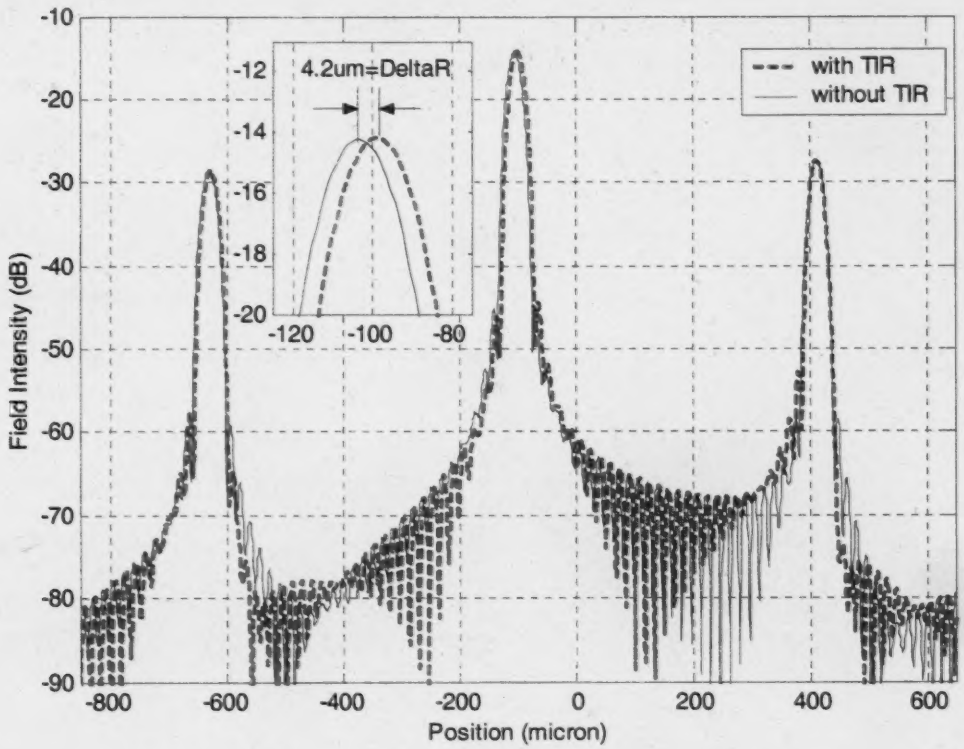

Fig. 3-13. Effect of retro-reflecting TIR facets on output field.

With the TIR facets, field peaks are shifted toward the shorter wavelength (right) side and there is little effect on peak intensities. A simulation with the point fields swapped on each facet but without adding the extra length w_j results in no field peak shift. Thus the field shift is caused by the addition of w_j, which varies from facet to facet. Adding the width difference between successive facets $\Delta w = \Delta R \times \Delta\theta$ to the LHS of Eq. (3-1), then the position x needs to be increased by ΔR to maintain the same grating order N_g. This results in a field peak shift of ΔR

towards $+x$ (the shorter wavelength) side. This field shift of ΔR can be confirmed from the inset of Fig. 3-13.

The output field shift can be easily compensated by adjusting positions of the output waveguides during photomask layout. For those planar concave gratings (such as the elliptic grating in Chapter 4) where the width difference Δw between successive facets is not constant as in the circular concave grating, the image error shown in Fig. 3-12 is expected to degrade grating performance, in addition to the doubling of the grating sidewall tilt loss. Therefore, TIR facets ease device fabrication processing at the price of increased grating loss and should ideally be avoided. These concerns will be addressed with a new planar concave grating design in Chapter 4.

3.5. Etching Undercut

Due to the non-ideal etching, a certain amount of undercut is always present, especially for DRIE. The amount of undercut depends on material, process and etching depth, and can be up to a few micrometers. Since grating facet surface roughness, sidewall tilt and facet corner rounding have already been addressed, a pure undercut (meaning a vertical sidewall with sharp corner and smooth surface) is assumed. This effect can be modeled as a constant decrease of radius R_j for each facet j, as schematically shown in Fig. 3-14(a). Fig. 3-14(b) shows the simulation results of the etching undercut on the output field with a relatively large 5 μm undercut compared to no undercut. Both output fields overlap closely with each other and thus it is concluded that the pure undercut has little effect on device performance. This is expected because there is effectively no change of ΔR with a constant decrease of R_j and thus no effect on the relative phases in light interference. Also, the undercut (up to a few micrometers) is a small dimension compared to the facet radius R_j (centimeters).

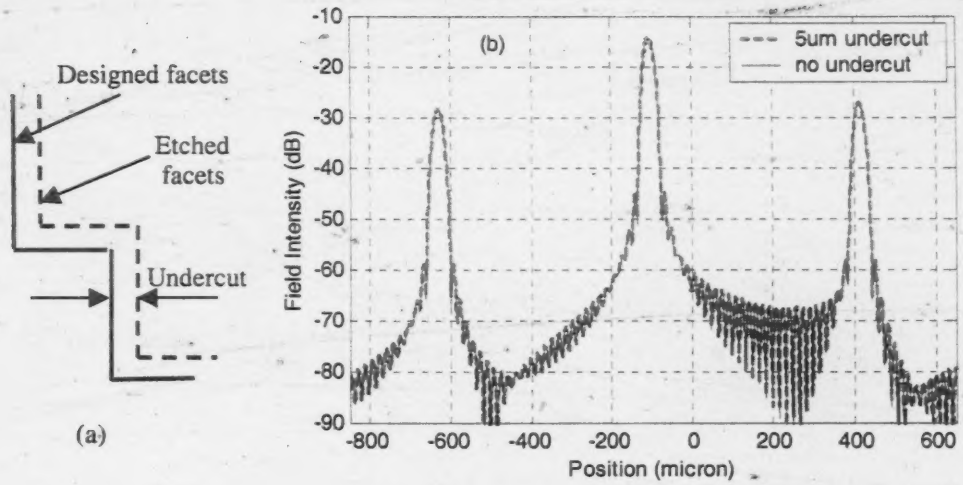

Fig. 3-14. (a) Etching undercut model and (b) the effect on output field.

3.6. Material Index Variation

Strict control on material refractive indices is not easy with polymers. Variation of the cladding material index will change the waveguide mode structure and profiles. An increase in material index contrast Δ may result in supporting more slab modes than desired. Those higher order modes will be shifted toward the longer wavelength channel because they have longer effective mode wavelengths and raise crosstalk levels. A decrease in Δ may reduce the number of modes supported for multimode waveguides, or in the case of singlemode waveguides, will increase mode field sizes and waveguide transmission loss through substrate absorption if the cladding layer is not thick enough. If the cladding index becomes higher than the core index, no waveguiding can be obtained.

To test how the circular concave grating DMUX is sensitive to the core material index variation, the device designed for n_1 = 1.553 in Table 2-1 was simulated with an actual core index of n_1 = 1.550 (a change of 0.19%). The effect on the output field is shown in Fig. 3-15. From Eqs. (3-1), (2-1) and (2-2), an output field peak shift of

$$dx = -\frac{\lambda_p S_1}{\delta\lambda n_1} dn_1, \tag{3-5}$$

or equivalently a channel wavelength shift of

$$d\lambda_p = -\lambda_p \frac{dn_1}{n_1} \tag{3-6}$$

is expected. The variation of channel physical spacing S_1 is proportional to the material index variation, and

$$S_1' = S_1 \frac{n_1}{n_1'}. \tag{3-7}$$

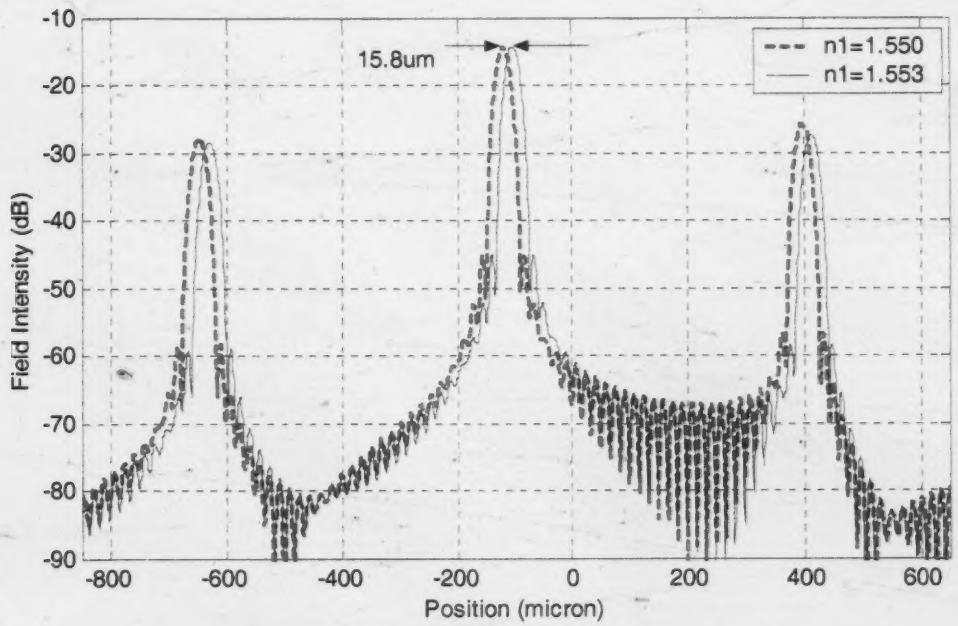

Fig. 3-15. Effect of core material index variation on output field.

With a channel physical spacing S_1 = 100 μm, the shift of the output field peak dx = 15.84 μm according to Eq. (3-5) and can be verified with Fig. 3-15. The change of the channel physical spacing S_1'-S_1 is only 0.65 μm according to Eq. (3-7). From Eq. (3-6), a certain percentage of variation in the core material index results in the same percentage of variation in the channel wavelength. This sensitivity of the channel wavelength to the material index variation can be used

to make thermally tunable polymeric WDM filters or to measure the actual material index.

3.7. Summary

To compare the relative contributions from individual microfabrication imperfections, Table 3-1 shows a typical set of microfabrication tolerances using conventional photolithography and DRIE. These tolerances are estimated from the trial fabrications of the circular concave grating DMUX (specified in Table 2-1) in BCB polymers before process optimizations. The respective contributions to the grating loss are also shown in Table 3-1, based on the simulation results in the previous sections. A comparison of the contributions from the different imperfections clearly suggests that the etched grating sidewall tilt is the dominant source of performance degradation under normal microfabrication tolerances. The retro-reflecting TIR facets using two reflective elements on each facet will double the dominant loss caused by grating sidewall tilt. In the next chapter, another planar concave grating DMUX based on intrinsic TIR will be presented to avoid the retro-reflecting TIR facets.

Table 3-1. Comparison of grating loss caused by individual microfabrication imperfections for multimode circular CWDM DMUX.

Imperfection	Tolerance	Grating loss	Reference
Facet surface roughness	$RMS = 40\ nm$, $CL = 0.5\ \mu m$	4 *dB*	Figs. 3-3, 3-4
Facet corner rounding	$R = 1\ \mu m$	2.7 *dB*	Fig. 3-6
Grating sidewall tilt	$\delta = -4°$	8 *dB*	Fig. 3-9
Etching undercut	$2\ \mu m$	0 *dB*	Fig. 3-14(b)
Use of TIR facets	yes	8 *dB*	Figs. 3-9, 3-13

4. Elliptic Concave Grating Demultiplexer

As discussed in the previous chapter, intrinsic TIR is desired to achieve low sensitivity to microfabrication imperfections and high efficiencies for planar concave grating DMUXes. This chapter presents another planar concave grating DMUX based on confocal ellipses and intrinsic TIR. The theoretical derivations and scalar electromagnetic simulations are presented. The design of a polymeric device for applications with MMFs is given. The elliptic concave grating has also been proposed for singlemode standard CWDM applications. Optimizations are carried out and flat-top passbands are achieved with a double parabolic waveguide horn structure. The simulation results for both designs are presented.

4.1. Theory of Elliptic Concave Grating DMUX

4.1.1. Grating Facet Construction

One important characteristic of an ellipse is that all rays emanating from one of its foci will be reflected by the ellipse and converge at the other focus. Assume that the input waveguide and the center of the output waveguides are located on the two foci of the confocal ellipses having the same focal length f, as shown in Fig. 4-1, and that the grating facets are sections of the confocal ellipses. For the ellipse denoted with an integer of j,

$$\overline{A_j F_1} + \overline{A_j F_2} = 2a_j, \tag{4-1}$$

where a_j is its semi-major axis and its semi-minor axis is

$$b_j = \sqrt{\left| a_j^{\,2} - f^2 \right|}. \tag{4-2}$$

Since the width of the input waveguide will be small compared to the dimensions of the ellipses, a point light source assumption is approximate. For a design

wavelength λ_d to form constructive interference at focus F_2, the optical path length difference Δl between successive grating facets must satisfy

$$\Delta l = \overline{A_{j+1}F_2} + \overline{A_{j+1}F_1} - \left(\overline{A_jF_2} + \overline{A_jF_1}\right) = 2\Delta a = N_g\lambda_d / n_1, \qquad (4\text{-}3)$$

where N_g is the grating diffraction order, n_1 is the refractive index of the core material in the slab waveguide, and $\Delta a = a_{j+1}$-a_j.

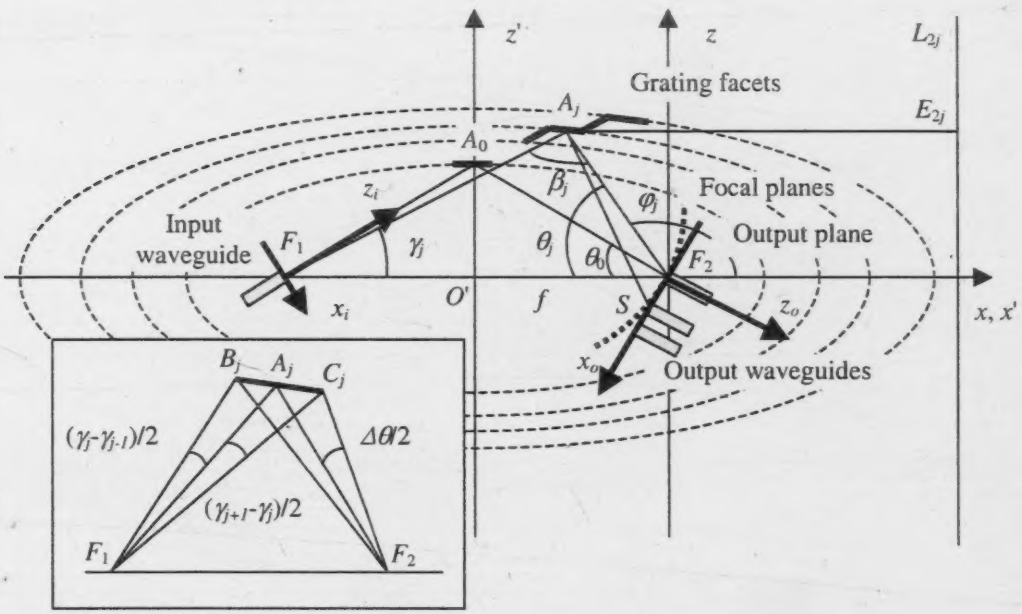

Fig. 4-1. Geometry of elliptic concave grating DMUX.

Choosing a focal length f that gives a sufficiently large grating facet size and a reasonable overall device size, a grating order N_g that gives non-overlapping of the output fields of adjacent grating orders as described later, and a central facet angle θ_0 so that TIR is satisfied on all facets, the semi-major axes of all ellipses can then be determined as

$$a_j = a_0 + j\Delta a, \qquad j = -J_{\min}, \ldots -2, -1, 0, +1, +2, \ldots + J_{\max}, \qquad (4\text{-}4)$$

where $a_0 = f/\cos\theta_0$.

Assume a flat output plane F_2S perpendicular to A_0F_2, and that the output waveguides are evenly located on this plane with a center-to-center spacing of S_1.

For the i^{th} channel (with a wavelength of $\lambda_d+i\delta\lambda$, where $\delta\lambda$ is the channel wavelength spacing), the output waveguide position S is iS_1 from F_2. For triangle $\Delta(A_jF_2S)$,

$$\begin{aligned}\overline{A_jS} &= \sqrt{\overline{A_jF_2}^2 + (iS_1)^2 - 2\overline{A_jF_2}\cdot iS_1\cdot\cos(\theta_j-\theta_0+\pi/2)} \\ &\approx \overline{A_jF}_2 + iS_1\cdot\sin(\theta_j-\theta_0)\end{aligned} \tag{4-5}$$

The above approximation is valid because iS_1 is normally a small dimension (tens to hundreds of micrometers) compared to $\overline{A_jF}_2$ (millimeters to centimeters). The optical path length for facet j is

$$l_j = \overline{A_jF}_1 + \overline{A_jS} \approx 2a_j + iS_1\cdot\sin(\theta_j-\theta_0) \approx 2a_j + iS_1(\theta_j-\theta_0), \tag{4-6}$$

if θ_j-θ_0 is a small angle, say, a few degrees. For constructive interference to happen at S for the i^{th} channel, the optical path length difference Δl between successive facets must satisfy

$$\Delta l = l_{j+1} - l_j = 2\Delta a + iS_1\Delta\theta = N_g(\lambda_d + i\delta\lambda)/n_1, \tag{4-7}$$

where $\Delta\theta = \theta_{j+1}$-$\theta_j$. Combining with Eq. (4-3),

$$\Delta\theta = N_g\delta\lambda/(n_1S_1). \tag{4-8}$$

So the center of grating facet j can be determined with A_jF_2 subtended with an angle $j\Delta\theta$ from A_0F_2. Its intersection with ellipse j gives the center A_j of facet j.

When the focal length $f = 0$, the semi-major axis a_j equals the semi-minor axis b_j and the elliptic concave grating becomes the circular concave grating discussed in Chapter 2 with $a_j = b_j = R_j$ and $\Delta a = \Delta R$. For intrinsic TIR, the angle β_j shown in Fig. 4-1 must be at least twice of the critical angle of TIR. The calculation of the angle β_j is presented below.

The focal parameter p_j is defined as

$$p_j = b_j^2/a_j, \tag{4-9}$$

and the eccentricity as

$$e_j = f/a_j . \tag{4-10}$$

As shown in Fig. 4-1, the directrix L_{2j} is parallel to the minor axis (z') and is a_j/e_j from the center O'. Shift the Cartesian coordinate system x'-z' towards $+x'$ by a displacement of f so that the origin is now moved from O' to F_2. For the facet central point $A_j(x_j, z_j)$ on facet j, under the new shifted Cartesian coordinate system x-z, we have

$$\overline{A_jF_2} = \overline{A_jE_{2j}} \cdot e_j = \left(a_j/e_j - f - x_j\right) \cdot e_j = a_j - fe_j - x_je_j . \tag{4-11}$$

Using a polar coordinate system with its origin at F_2,

$$\overline{A_jF_2} = \frac{p_j}{1 + e_j \cos\varphi_j}, \tag{4-12}$$

So

$$\theta_j = \pi - \varphi_j = \pi - \cos^{-1}\left(\frac{p_j - \overline{A_jF_2}}{\overline{A_jF_2} \cdot e_j}\right). \tag{4-13}$$

Using Eqs. (4-1), (4-12), and (4-13), and triangle $\Delta(A_jF_1F_2)$, angle β_j can be obtained and should satisfy TIR with

$$\begin{aligned}
\beta_j &= \cos^{-1}\left(\frac{\overline{A_jF_1}^2 + \overline{A_jF_2}^2 - 4f^2}{2 \cdot \overline{A_jF_1} \cdot \overline{A_jF_2}}\right) \\
&= \cos^{-1}\left(\frac{2p_j^2 - 4b_j^2 e_j \cos\theta_j \left(1 - e_j \cos\theta_j\right)}{4b_j^2\left(1 - e_j \cos\theta_j\right) - 2p_j^2}\right), \\
&> 2\sin^{-1}\left(\frac{n_0}{n_1}\right)
\end{aligned} \tag{4-14}$$

where n_0 is the refractive index outside the slab and is normally 1 for air.

Since it is not obvious which facet will have the minimum β_j, Eq. (4-14) should be checked for each facet. If the angle θ_0 is small enough, the TIR requirement should always be satisfied. However, a small θ_0 (large incident angles on grating facets) will end up with a large total grating width, and it might

become impossible to construct grating facets without *shadowing*[3]. Also, the distortion of image, as described later in Section 4.3, is more severe with a smaller θ_0. So θ_0 should be chosen as large as possible while still allowing TIR.

4.1.2. Facet Shadowing Elimination

As with the circular grating in Chapter 2, the facet ends can be determined by the intersections of ellipse j with B_jF_2 and C_jF_2, each subtended with an angle $\Delta\theta/2$ around A_jF_2. However, a grating facet so constructed could be partially or even completely shadowed by its left adjacent facet for light emanating from focus F_1. Complete facet shadowing should be avoided by choosing proper design parameters (f, θ_0, N_g, λ_d, N_{ch}, $\delta\lambda$, S_1, n_1, etc.). Angle γ_j shown in Fig. 4-1 should decrease with increasing θ_j. Otherwise, if $\gamma_j > \gamma_{j-1}$ then facet j will be completely shadowed by facet j-1 for light from focus F_1. A closed-form expression of criteria that the design parameters should satisfy to avoid complete facet shadowing could not be obtained. However, this can be checked using Eq. (4-14) when numerically generating grating facets.

Partial shadowing[4] will not affect grating performance but will result in unnecessarily wide facets and acute facet corner angles. It can be eliminated by constructing facet ends from focus F_1 instead of F_2. Each facet center is constructed as described before, but facet ends are constructed as the intersections of B_jF_1 and C_jF_1 with ellipse j, as shown in the inset of Fig. 4-1. C_jF_1 subtends A_jF_1 with an angle of $(\gamma_{j+1}-\gamma_j)/2$, and B_jF_1 subtends A_jF_1 with $(\gamma_j-\gamma_{j-1})/2$. Note that unlike θ_j, γ_j is not a linear function of the facet number j.

4.1.3. Maximum Grating Order

To avoid crosstalk, the output fields of diffraction orders $N_g\pm1$ for one wavelength should not overlap with those of order N_g for other wavelengths. Assume the field peaks of orders $N_g\pm1$ for the design wavelength λ_d are $\pm X$ from F_2 on the flat output plane F_2S. From Eq. (4-7),

---

[3] That is, facet j is hidden from the input by facet j-1.
[4] That is, only part, less than half, of facet j is hidden from input by facet j-1.

$$2\Delta a \pm X\Delta\theta = (N_g \pm 1)\lambda_d / n_1 . \tag{4-15}$$

Combining with Eq. (4-3),

$$X = \lambda_d / (n_1 \Delta\theta). \tag{4-16}$$

Non-overlapping of the output fields of adjacent orders requires that $X > N_{ch}S_1$, where N_{ch} is the number of wavelength channels. From Eqs. (4-8) and (4-16),

$$N_g < \lambda_d / (N_{ch}\delta\lambda). \tag{4-17}$$

Again, the product $N_{ch}\delta\lambda$ is the FSR of the grating and the above requirement is similar for the circular grating and other gratings in general. N_g can take any positive integer satisfying the above inequality. However, since the facet feature size is proportional to the grating order, N_g normally takes the maximum integer allowed for ease of microfabrication.

4.1.4. Total Number of Grating Facets Required

The total grating width should be large enough to capture most of the input optical power. The total number of grating facets required can be first estimated using ray theory. Let φ_N be the incident angle on the core-cladding interface for the highest order horizontal mode of the input waveguide. φ_N is then the minimal among the incident angles of all guided horizontal modes in the input waveguide, and is related to the NA of the input waveguide, as schematically shown in Fig. B-1 in Appendix B. Let the edges of the grating (with facet J_{max} and $-J_{min}$) correspond to this angle φ_N, then

$$\gamma_{\pm J} = \gamma_0 \mp (\pi/2 - \varphi_N) = \theta_0 \mp (\pi/2 - \varphi_N), \tag{4-18}$$

where $\pm J$ denotes J_{max} and $-J_{min}$, respectively. Also for triangle $\Delta(A_j F_1 F_2)$,

$$\begin{aligned} \gamma_{\pm J} &= \pi - \theta_{\pm J} - \beta_{\pm J} \\ &= \pi - (\theta_0 \pm J\Delta\theta) - \sin^{-1}\left(\frac{2f}{A_{\pm J}F_1}\sin(\theta_0 \pm J\Delta\theta)\right), \end{aligned} \tag{4-19}$$

and using Eqs. (4-2), (4-4), (4-9), (4-10), and (4-12)

$$\overline{A_{\pm J}F_1} = 2a_{\pm J} - \frac{p_{\pm J}}{1 - e_{\pm J}\cos\theta_{\pm J}}$$
$$= 2(a_0 \pm J\Delta a) - \frac{(a_0 \pm J\Delta a)^2 - f^2}{a_0 \pm J\Delta a - f\cdot\cos(\theta_0 \pm J\Delta\theta)}, \quad (4\text{-}20)$$

so

$$\theta_0 \mp (\pi/2 - \varphi_N)$$
$$= \pi - \theta_0 \mp J\Delta\theta - \sin^{-1}\left(\frac{2f\cdot\sin(\theta_0 \pm J\Delta\theta)}{2(a_0 \pm J\Delta a) - \frac{(a_0 \pm J\Delta a)^2 - f^2}{a_0 \pm J\Delta a - f\cdot\cos(\theta_0 \pm J\Delta\theta)}}\right). \quad (4\text{-}21)$$

Eq. (4-21) can be used to numerically solve for J_{max} and J_{min}, because the RHS should be a monotonic function of J after grating facet shadowing is eliminated. Unlike the circular grating, $J_{max} \neq J_{min}$. The minimum horizontal mode angle φ_N can be numerically solved as described in Appendix B. In the case of a singlemode device, φ_N is just the mode angle of the fundamental horizontal mode in the input waveguide. The actual facet numbers should be at least those calculated from Eq. (4-21) until the power on the grating approaches the input power.

4.2. Simulation of Elliptic Concave Grating DMUX

To simulate singlemode devices with small-dimension input waveguides, the electromagnetic field in the input waveguide, E_{in}, is rigorously solved following Ref. [35], as is detailed in Appendix B. To save computing time, only the fundamental TE mode is considered in the following simulations, even in the case of a multimode device. Higher order vertical slab modes, if they exist, have longer effective mode wavelengths in the slab region and are shifted linearly toward the longer wavelength side on the output plane, as in the circular grating. Higher order horizontal modes in the input waveguide change the total input field

profile and are expected to affect coupling efficiencies to the output waveguides, but not the functionality of the DMUX.

Similar to the circular concave grating DMUX, the electromagnetic field, E_g, at any point (x_i^g, z_i^g) on the grating facets is calculated using numerical integration with the two-dimensional Fresnel diffraction operator [36] for the slab region and the coordinate system x_i-z_i shown in Fig. 4-1,

$$E_g(x_i^g, z_i^g) = \int E_{in}(x_i^i, 0)\sqrt{\frac{ik_i}{2\pi z_i^g}}\exp\left(-ik_i z_i^g - \frac{ik_i\left(x_i^g - x_i^i\right)^2}{2z_i^g}\right)dx_i^i \quad (4\text{-}22)$$

where $k_i = 2n_1\pi/\lambda_i$ is the wavenumber of the i^{th} channel wavelength λ_i in the slab waveguide. The output field at any point $(x_o^o, 0)$ on the output plane can be calculated similarly, using the grating field as the source and another coordinate system x_o-z_o shown in Fig. 4-1,

$$E_{out}(x_o^o, 0) = \int E_g(x_o^g, z_o^g)\sqrt{\frac{ik_i}{2\pi z_o^g}}\exp\left(-ik_i z_o^g - \frac{ik_i\left(x_o^o - x_o^g\right)^2}{2z_o^g}\right)dx_o^g \quad (4\text{-}23)$$

The simulation codes are implemented in Matlab. A flowchart of the simulation is shown in Fig. 4-2. Given the design and waveguide parameters, the minimal mode angle φ_N is numerically solved following Appendix B and the total numbers of facets on either side of the grating are estimated with Eq. (4-21). The grating facets are then constructed and positions of enough sample points on each facet are calculated. The input field for each channel wavelength is numerically solved following Appendix B and the total optical power is normalized. Alternatively, the input field can be generated with an external optical Beam Propagation Method (BPM) simulation package. The field at each sample point on the grating facets is calculated using Eq. (4-22). The output field is calculated using Eq. (4-23) and its total power is calculated. Both the power of the output field and the power of the nominal field in the output waveguide are normalized and the channel efficiency is calculated using the overlap integral method, as in Eq. (3-3).

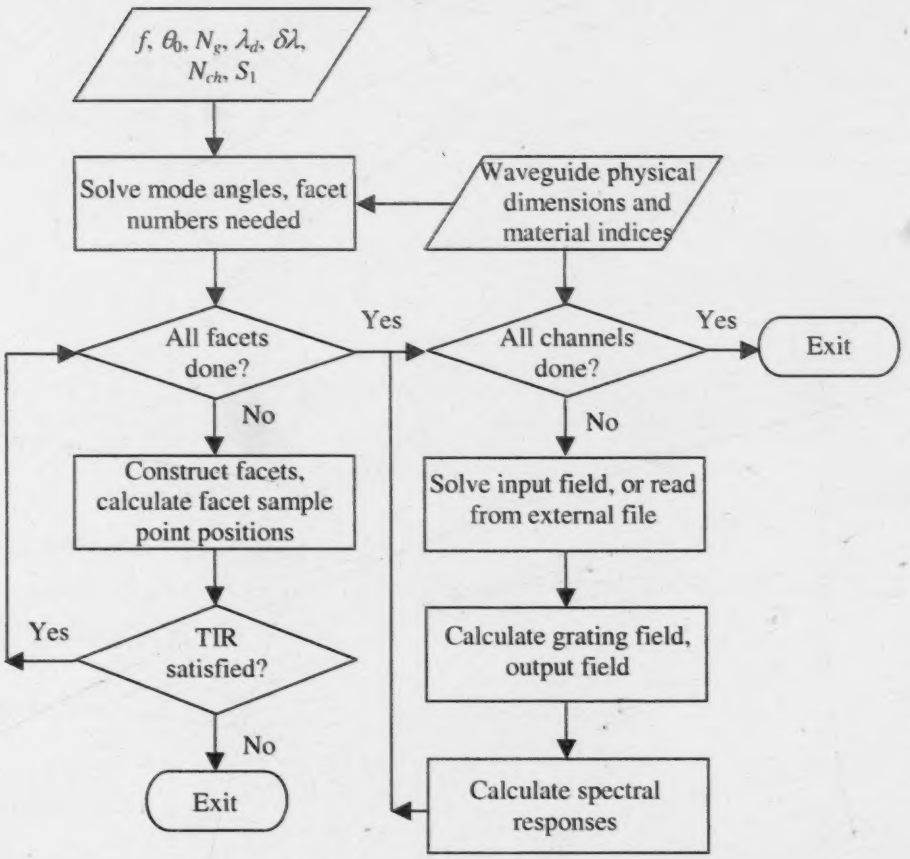

Fig. 4-2. Simulation flowchart for elliptic concave grating DMUX

Rigorous calculation of spectral responses is a time consuming algorithm that requires the calculations of the input field, the grating field, the output field and the coupling efficiency for each wavelength with a fine step between two adjacent channel wavelengths. Since the dispersion along the output plane is linear and the field profiles have little variation for two closely spaced wavelengths, the output field of a channel wavelength is assumed to be similar for all wavelengths between this channel and one of its adjacent channels, and the spectral responses for non-channel wavelengths are obtained by moving the output field of the channel wavelength linearly along the output plane and then calculating its coupling efficiencies to the nominal output waveguide field at the channel wavelength.

4.3. Multimode Elliptic DMUX Design

As with the circular grating, a DMUX based on the elliptic grating was designed for multimode applications. The design parameters are chosen to satisfy TIR and to successfully construct grating facets without facet shadowing. Optimizations have also been carried out to maximize the facet size while keeping the overall chip size reasonable. The device is to be fabricated using the LIGA process described in Chapter 5. Table 4-1 shows the design parameters. The waveguide core material is PMMA polymer and the lower cladding is thermal silica on a silicon substrate. The grating order takes the maximal allowed integer in Eq. (4-17). With the given material indices and the input waveguide dimensions, the minimum mode angle φ_N is solved and the number of grating facets required is calculated. The minimum light incident angle on all facets can be verified to be larger than the critical angle $\beta_{critical}$ and thus TIR is satisfied.

Table 4-1. Design parameters of multimode elliptic concave grating DMUX.

Material indices	$n_1 = 1.49$ (PMMA), $n_2 = 1.45$ (SiO_2)
Focal length	$f = 1\ cm$
Central facet angle	$\theta_0 = 40°$
Waveguide dimensions	$W = 50\ \mu m$, $H = 50\ \mu m$
Output waveguide spacing	$S_1 = 75\ \mu m$
Design wavelength	$\lambda_d = 820\ nm$
Channel wavelength spacing	$\delta\lambda = 20\ nm$
Channel count	$N_{ch} = 4$
Grating order	$N_g = 10$
Number of facets	$J_{max} = 274$, $J_{min} = 131$
Grating facet width	$w_j = 15.0$–$35.1\ \mu m$
Min. incident angle	$\beta_{min}/2 = 42.64° > \beta_{critical} = 42.12°$
Min. mode angle	$\varphi_N = 76.62°$
Number of modes supported	43 vertical slab TE modes.

Although the slab region supports 43 TE modes, only the fundamental mode is simulated. The effective mode wavelengths for all modes in the slab region is between λ/n_1 for the fundamental mode and λ/n_2 for the highest order mode, so the effective mode wavelength variation is

$$\lambda_{eff\_range} = \lambda/n_2 - \lambda/n_1 . \qquad (4\text{-}24)$$

The worst-case scenario is for the channel with the *second longest*[5] wavelength 840 *nm*, for which λ_{eff_range} is 15.55 *nm*. With S_1 = 75 μm and $\delta\lambda$ = 20 *nm*, the highest order mode will be 58.31 μm to the longer wavelength side from the center of the channel output waveguide. With W = 50 μm it should be 8.31 μm within the boundary of the output waveguide of its adjacent channel with a wavelength of 860 *nm*. However, with 43 modes supported, the highest order mode is expected to possess little optical power if the mode power distribution approximately follows the cosine square law. Therefore, the device crosstalk performance will not be affected significantly.

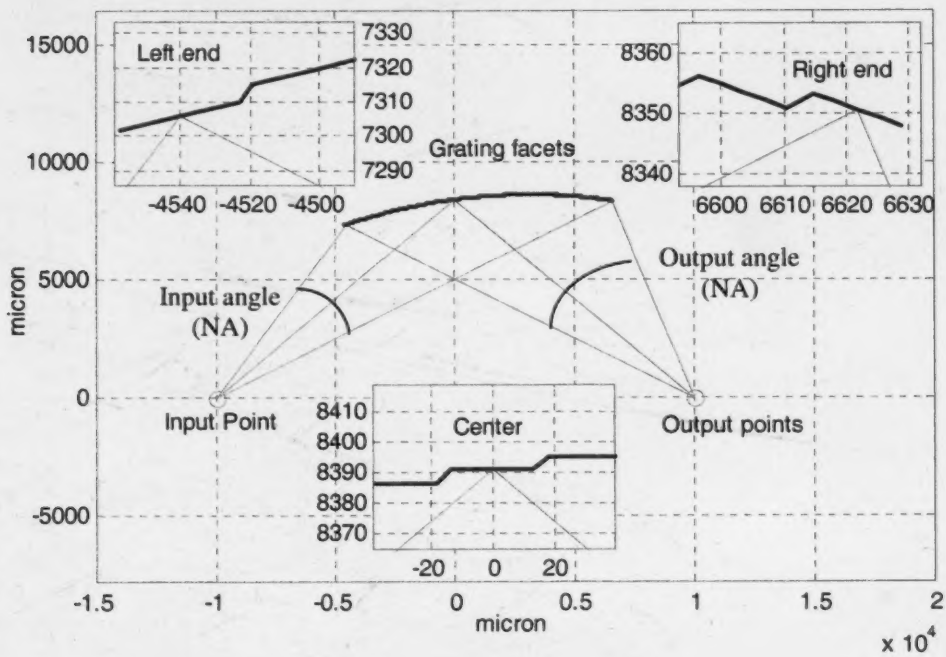

Fig. 4-3. Layout of multimode elliptic concave grating DMUX.

The device layout is shown in Fig. 4-3 with three insets showing the left end, the center and the right end of the grating facets, respectively. Both the facet width and the facet step size vary from facet to facet. The input and output waveguides are not shown in Fig. 4-3. S-bends were used to make the input waveguide horizontal so that an input optical fiber can be coupled to the left

[5] Higher order slab modes of the longest wavelength 860 *nm* have effective mode wavelengths outside of the spectral range of the device and do not contribute to channel crosstalk.

cleaved edge of the device for testing. S-bends were also used to make the output waveguides horizontal to the right edge and to expand their spacing to 1 *mm* so that a MMF fiber array can be butt-coupled to the device edge using a silicon V-groove alignment chip.

Simulation results of the output fields are shown in Fig. 4-4. The input field of the central channel with the design wavelength 820 *nm* is also shown in dashed line for comparison. From Fig. 4-4, it can be confirmed that the elliptic grating does not give a perfect image of the input field, with the output field compressed and its mode size reduced compared to the input field. This distortion of image is due to the unequal angles or NA shown in Fig. 4-3. Channel efficiencies and spectral responses are not available since the higher order modes are not simulated. As with the circular grating, the photomask layout for the device was carried out using the script programming in the mask layout CAD tool Odin™. The overall chip size including S-bends is approximately 3.6 *cm* × 1 *cm*.

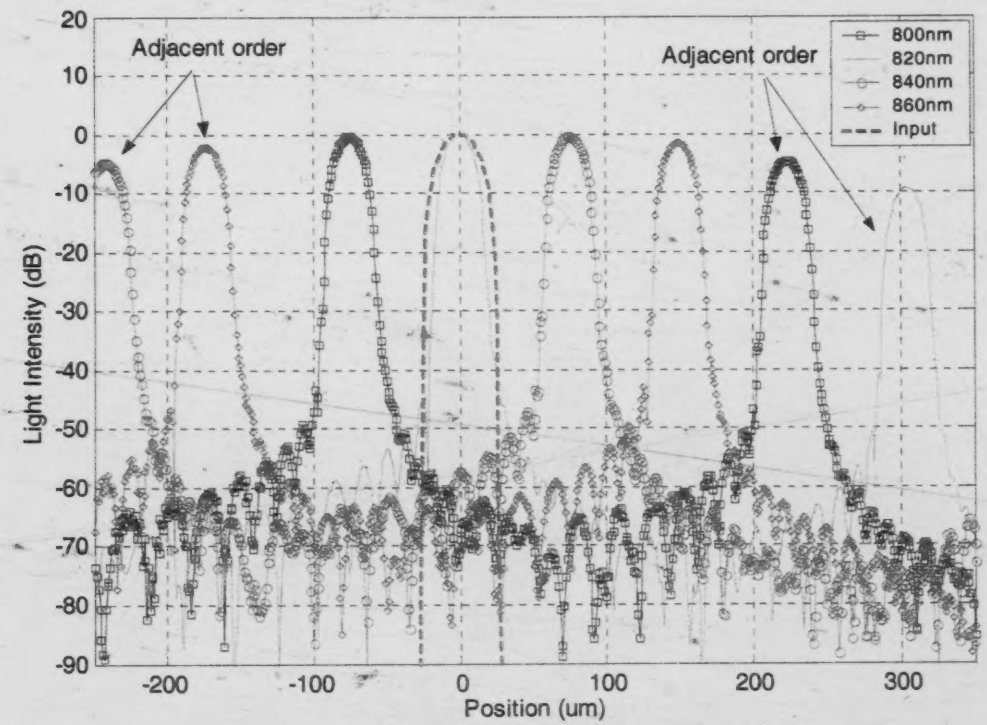

Fig. 4-4. Output fields of multimode elliptic concave grating DMUX with only fundamental modes simulated.

4.4. Singlemode Elliptic DMUX Design

4.4.1. Basic Design

The elliptic concave grating DMUX has also been considered for singlemode standard CWDM applications. Although many applications would initially require only a subset of the 18 channels on the ITU recommended CWDM wavelength grid, it is desirable to have an integrated DMUX that offers all the 18 channels on a single chip. Incorporating all 18 channels with a wavelength span of 340 *nm* into one device presents challenges for device optimizations. The design parameters for the 18-channel singlemode CWDM DMUX are shown in Table 4-2.

Table 4-2. Design parameters of singlemode elliptic CWDM DMUX.

Material indices	$n_1 = 1.5435$, $n_2 = 1.5360$ (at 1430 *nm*)
Focal length	$f = 5mm$
Central facet angle	$\theta_0 = 45°$
Waveguide dimensions	$W = 4\ \mu m$, $H = 4\ \mu m$
Output waveguide spacing	$S_1 = 30\ \mu m$
Design wavelength	$\lambda_d = 1430\ nm$
Channel wavelength spacing	$\delta\lambda = 20\ nm$
Channel count	$N_{ch} = 18$
Grating order	$N_g = 3$
Number of facets	$J_{max} = 77$, $J_{min} = 65$
Grating facet width	$w_j = 8.2–9.8\ \mu m$
Min. incident angle	$\beta_{min}/2 = 43.97° > \beta_{critical} = 40.38°$
Min. mode angle	$\varphi_N = 86.34°$
Number of modes supported	Singlemode.

The waveguide core and cladding materials are photosensitive BCB (Cyclotene™ 4024) polymer and dry-etch BCB polymer (Cyclotene™ 3022), respectively, with their material dispersion functions obtained with linear interpolation from their indices at 1310 *nm* and 1550 *nm* as

$$\begin{aligned} n_1 &= 1.5495 - 0.0042\lambda \\ n_2 &= 1.5479 - 0.0083\lambda \end{aligned}, \qquad (4\text{-}25)$$

where the wavelength λ is in the unit of μm.

Since only the fundamental mode is supported in the slab region, the grating needs only 142 facets and TIR is satisfied on all facets. Although with a

low grating order of 3, the width of the facets is approximately 9 μm and the facet step size 3 μm, well within the capability of conventional microfabrication without going to expensive and time-consuming e-beam lithography. The relatively large facet size is the result of the high blaze angle ($\beta_j/2$ in Fig. 4-1) used (~ 45° in this case). Facet corner angles are approximately 135°. Such obtuse facet corner angles should be less sensitive to the corner rounding effect during photolithography and RIE processes, which introduces loss and crosstalk.

The simulated spectral responses of the device are shown in Fig. 4-5. Efficiencies of all 18 channels are between 2.5 *dB* and 4.5 *dB*. Crosstalk levels between adjacent channels are below 35 *dB*.

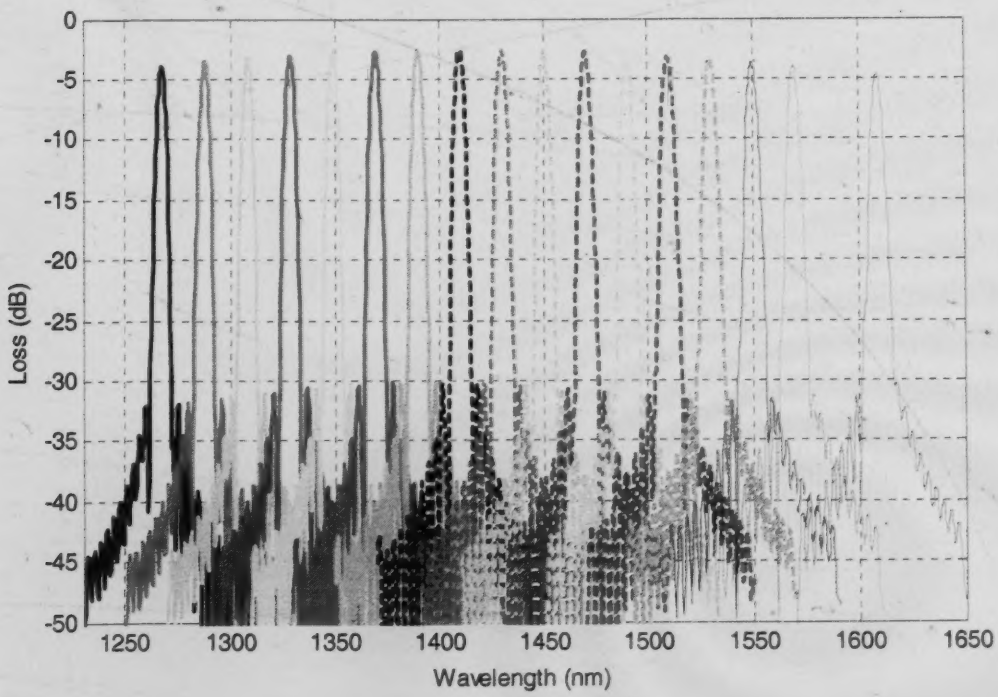

Fig. 4-5. Spectral responses of singlemode elliptic CWDM DMUX without optimization.

However, for CWDM applications the following problems can be identified from Fig. 4-6, which shows the spectral responses of the two extreme channels (1270 *nm* and 1610 *nm*) and the central channel (1430 *nm*) with respect

to their nominal channel wavelengths before (dashed) and after (solid) the focal plane optimization discussed in Section 4.4.2:

- Non-uniform channel efficiencies. Edge channels have lower efficiencies than the central channel, with a uniformity of ~ 2 *dB*. Although a 2 *dB* uniformity is acceptable, it is later found that when the channel passbands are flattened using the technique described in Section 4.4.3, the uniformity becomes as high as 7 *dB*.
- Channel wavelength inaccuracy. The channel wavelengths of the edge channels are shifted up to 2.5 *nm* from designed.
- Gaussian channel passbands. For CWDM, wide flat-top passbands are desired so that source wavelength drift, DMUX thermal wavelength drift, and DMUX PDL can all be accommodated. A greater than 12 *nm* passband is recommended by ITU [6].

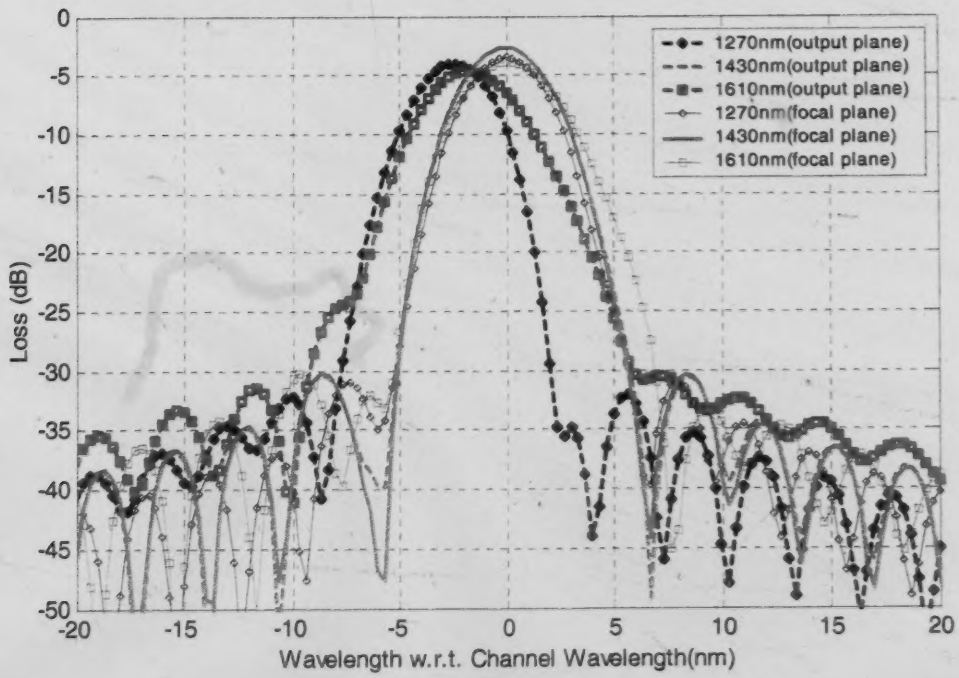

Fig. 4-6. Spectral responses of extreme and central channels on designed flat output plane (dashed) and optimized focal planes (solid).

The first two problems are caused by the fact the designed flat output plane is not necessary the optimal focal curve, and can be reduced by placing the output waveguides on the ideal focal curve instead of the flat output plane. The last problem is typical for all grating-based DMUXes where the output field is close to an image of the Gaussian shaped input mode field. The following sections will address these problems and optimize the design.

4.4.2. Approximate Focal Planes

The designed flat output plane is not the optimal focal curve due to the approximations taken in Eqs. (4-5) and (4-6), as well as the chromatic aberration of the grating. These approximations can cause channel wavelength shift and penalties for channel efficiencies and uniformity. The ideal focal curve can be calculated by (1) searching through positions around the designed output point for each channel, and (2) for each position, searching tilt angles and calculating output field on that tilted plane and finding the position that gives the highest grating efficiency with coupling to the output waveguide considered. However, as shown in Fig. 4-7(a), this algorithm involves a variation of 4 parameters and is very demanding on computing resources.

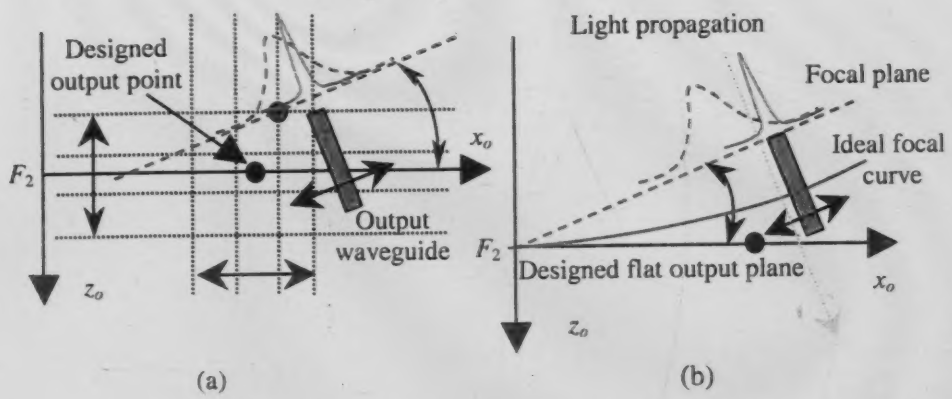

Fig. 4-7. (a) Ideal algorithm and (b) approximate algorithm for channel focal point searching.

An approximate algorithm can be applied based on the facts: (1) that the beam shape evolves slowly along the direction of light propagation in optical waveguides, and (2) that the tilt angle has an exponential effect on the coupling

efficiency, similar to the grating sidewall tilt loss discussed in Section 3.3. Therefore, it can be assumed that the optimal focal curve for each channel is a tilted focal plane going through F_2 with a small tilt angle with respect to the designed flat output plane, as shown in Fig. 4-7(b). By searching through tilt angles, a near ideal focus for each channel can be obtained. This approximate algorithm involves a variation of only 2 parameters and is much faster than the ideal algorithm.

The optimal tilt angles found with the approximate algorithm are shown in Fig. 4-8 for the device in Table 4-2. The tilt angles can be fitted with a degree-2 polynomial of the channel number (and thus x_o of the x_o-z_o coordinate in Fig. 4-1 because of the designed linear dispersion on the output plane along the x_o-axis). Hence, the ideal focal curve is expected to be a cubic curve, although its exact expression cannot be obtained. The tilted focal planes were applied and the spectral responses on the calculated focal planes for the two extreme channels and the central channel with respect to their nominal channel wavelengths are shown in Fig. 4-6. The channel wavelength shift for the edge channels is now corrected and both the channel efficiencies and uniformity are improved.

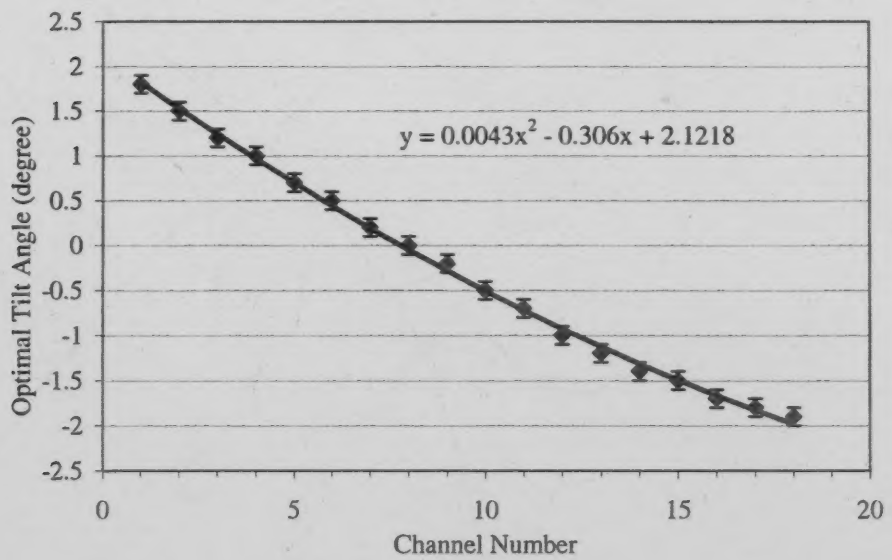

Fig. 4-8. Optimal focal plane tilt angles according to approximate algorithm.

4.4.3. Passband Optimization

To accommodate wavelength drift in CWDM, a greater than 12 *nm* flat-top passband is required [6]. Since the output field in both AWGs and etched planar concave grating DMUXes is an image (Fresnel-Fourier transform) of the input field, flat-top passbands can be achieved by the manipulations of either the input field or the space transformation function. Passband flattening techniques have been reported for AWG optimizations, using MultiMode Interference (MMI) couplers [37], parabolic waveguide horns [38], space filtering [39, 40], double gratings [41, 42], interleave filters [43] and Fabry-Perot filters [44]. A grating with three subsections each having a different focal point has also been reported for planar concave grating DMUXes based on Rowland circles [45]. Elliptic waveguide horns [46, 47] and coherent Y-splitters can also be used to flatten the passband in principle. However, our simulation experiments with MMI couplers and Y-splitters were found to be very wavelength sensitive and not suitable for the wide spectral span of 340 *nm* involved in this 18-channel CWDM DMUX. The single convex parabolic horn used in Ref. [38] was found to be less wavelength-sensitive and could obtain reasonably flat-top passbands for all 18 channels, but crosstalk levels between adjacent channels were found to be around 10 *dB*, much worse than normally acceptable levels of 25 *dB*.

Since a convex parabolic waveguide horn expands and collimates light, a concave parabolic waveguide horn is expected to do the opposite. Therefore, a short concave parabolic horn reverse-coupled to a long convex parabolic horn is expected to compress the near collimated field at the end of the convex parabolic horn, as shown in Fig. 4-9. Since the DMUX output field is close to an image of the input field, the compression of the input field waist is expected to result in waist compression of the output field and reduction of the crosstalk levels. With the optimized dimensions (in micrometer) of the double parabolic waveguide horns shown in Fig. 4-9, optical field cuts calculated using optical BPM simulations are shown for the design wavelength 1430 *nm* at the ends of the straight waveguide, the first convex parabolic horn and the second concave parabolic horn, respectively.

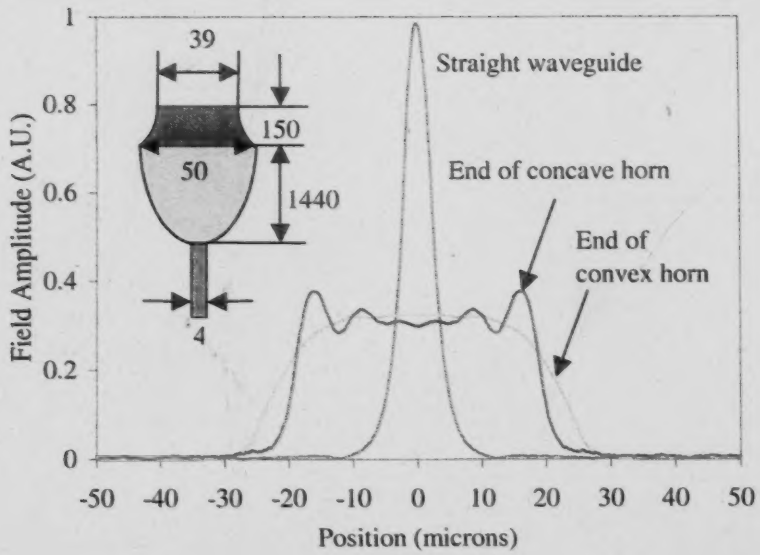

Fig. 4-9. Double parabolic waveguide horns and field cuts at 1430 nm

Fig. 4-10 shows the optical field propagation in the waveguide structure for wavelength 1430 *nm* according to BPM simulation obtained with OptiBPM™. For each wavelength, the field at the end of the concave parabolic horn is used as the input field to our scalar electromagnetic simulation. This double horn structure itself introduces little loss according to the BPM simulations and its sensitivity to wavelengths within the 340 *nm* spectral span is included in the simulation results given below.

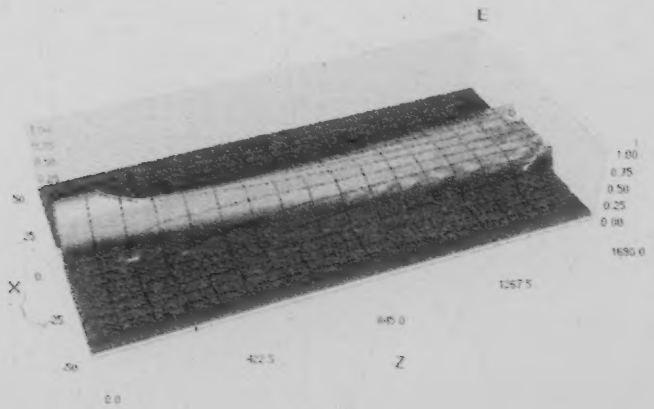

Fig. 4-10. Field propagation of 1430 nm in double parabolic waveguide horns.

The spectral responses for the optimized DMUX with double parabolic horns in the input waveguide are shown in Fig. 4-11, shifted with respect to the nominal channel wavelengths. The inset shows details of the passbands of the two extreme channels and the central channel. All 18 channels have an optimized 1 *dB* passband greater than 12 *nm* and the ripple in each channel passband is less than 0.5 *dB*. Crosstalk levels between adjacent channels are better than 21 *dB* and channel efficiencies for all 18 channels are between 6 *dB* and 7.5 *dB* with a uniformity of 1.5 *dB*. The flat-top passbands are achieved at the price of increased channel losses. The remaining non-uniformity can be attributed to the approximations in the focal planes, and the fact that the grating is designed for a design wavelength of 1430 *nm* and thus chromatic aberration exists. Overall, the simulated performance for a DMUX with 18 channels is promising for CWDM applications.

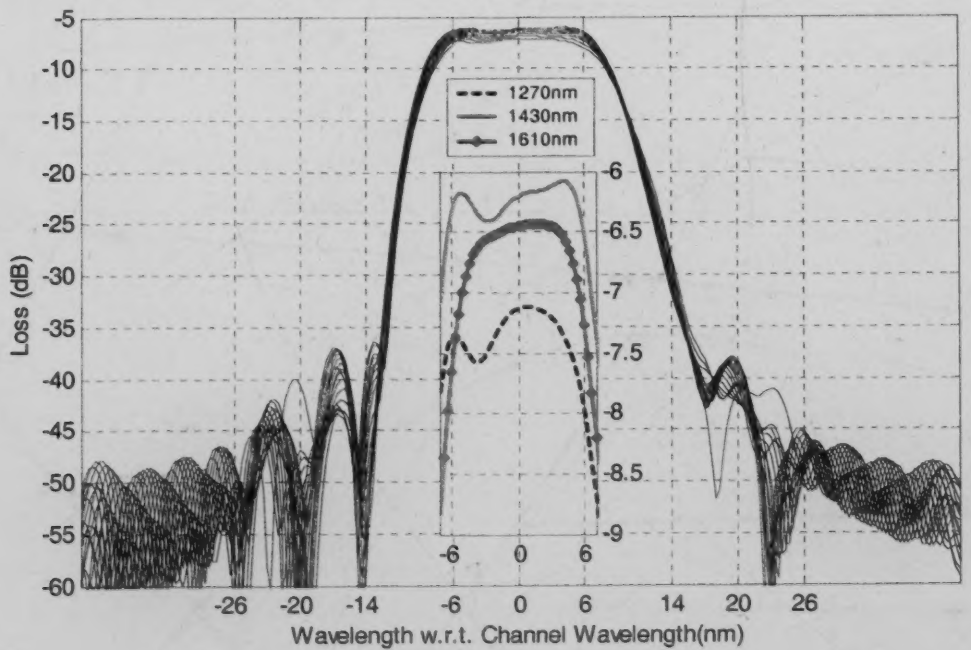

Fig. 4-11. Spectral responses of passband-optimized singlemode elliptic CWDM DMUX w.r.t. nominal channel wavelengths.

If less than 18, for example 4 or 8 channels, are required in a single DMUX device, the device optimizations will be easier and the device

performance including channel efficiencies, channel isolation, passband shapes can all be further improved.

4.5. Elliptic Grating vs. Circular Grating

The elliptic concave grating is designed to minimize its sensitivity to microfabrication imperfections, especially the tilt of etched grating sidewalls, which is the dominant source of grating loss according to Chapter 3, as well as to avoid the image error introduced by retro-reflecting TIR facets. Advantages of the elliptic concave grating DMUX compared to the circular concave grating DMUX include:

- Intrinsic TIR facets: these eliminate the image error associated with retro-reflecting TIR facets and no backside reflective metal coating is needed for the grating facets.
- Minimum number of reflective elements with each facet: only one reflective element is used for each facet and thus the loss caused by etched grating sidewall tilt is minimized.
- Obtuse facet corner angles and large facet size. Unlike the circular grating (Fig. 2-3), grating facets are not perpendicular to grating steps in the elliptic grating (Fig. 4-3). Both the facet width and the facet step size are larger for the elliptic grating. The increased size is the result of the high blaze angle ($\beta_i/2$ in Fig. 4-1) used in the elliptic grating. Both the large size facets and the obtuse facet corner angles are less sensitive to microfabrication imperfections such as the facet corner rounding effect discussed in Section 3.2.
- Separated input waveguide and output waveguides. Separating the waveguides makes fiber coupling and device testing easier. There is no vacant channel as in the circular grating where the central channel with the design wavelength λ_d is unavailable.

Disadvantages of the elliptic concave grating DMUX include:

- Complicated relationship between the device design parameters and the resultant grating facet layout. Unlike the circular grating where facet construction is guaranteed for any design parameters if physical dimensions are not concerned, the elliptic grating requires careful and heuristic selection of the design parameters to satisfy both the TIR requirement and the elimination of facet shadowing.
- Larger overall chip size. An elliptic concave gating DMUX with a focal length f is expected to have a chip size more than twice of that of a circular concave grating DMUX with a central facet radius R_0 equal to f.
- Unlike the circular grating where the input angle (NA) equals to the output angle (NA), the input angle (NA) is smaller than the output angle (NA) in the elliptic grating (Fig. 4-3). Therefore, the mode size of the output field will be smaller than that of the input field, as confirmed in Fig. 4-4. This distortion of image will affect coupling efficiencies to the output waveguides unless the widths of the output waveguides are adjusted accordingly. This distortion of image also requires the central facet angle θ_0 be as small as possible, since the difference between the input angle (NA) and output angle (NA) is small when θ_0 is small.

5. Microfabrication Processing and Optimizations

This chapter describes the microfabrication techniques used to fabricate both the circular and elliptic concave grating DMUXes. The emphasis is on how to achieve deep, smooth and vertical grating sidewalls in polymers, which is the most challenging requirement involved.

5.1. DMUX Fabrication with Dry Etching

For multimode DMUXes, the waveguide core layer thickness ideally needs to be close to the core diameter of MMFs. To achieve good channel isolation performance, the index contrast between the waveguide core and cladding materials needs to be small so that the high order slab modes do not overlap with adjacent channel wavelengths, as required by Eq. (2-4). BCB polymers are chosen based on the considerations of available polymer thickness and index contrast. The multimode circular concave grating DMUX specified in Table 2-1 was fabricated with BCB polymers using conventional photolithography and RIE with a high-density plasma generated in the Inductively Coupled Plasma (ICP) RIE system in the Nanofab of the University of Alberta.

5.1.1. BCB Polymers

BCBs are spin-on polymers containing silicon and thus retain many of the advantages of SiO_2 such as good adhesion to substrates and many other materials, high thermal stability and good patternability. They were initially synthesized as low-k dielectrics for microelectronic applications, but their properties have also made them applicable to optical waveguides. BCB polymers are products of Dow Chemical under the trademark Cyclotene™. Key properties related to optical applications include:

- High thermal stability with a glass transition temperature T_g above 350 $°C$ [48, 49].

- High optical transparency with a theoretical transmittance greater than 90% in the visible and near infrared (IR) range if properly cured [50, 51]. A waveguide transmission loss of 0.81 *dB/cm* has been reported for a 1300 *nm* singlemode waveguide directly patterned in the photosensitive BCB (photo BCB) with the dry-etch BCB as cladding layer [52].
- Cured film thickness up to 26 μm for the dry-etch BCB [48] and 18.5 μm after soft bake and 14.2 μm after development for the photo BCB [49].
- Small index contrast (~ 0.7%) between the dry-etch BCB and the photo BCB [53].

BCB polymers have been used to fabricate optical waveguides [52, 54] and mirrors [55, 56]. Dry-etch BCB can be thermally cured and patterned with RIE. Photo BCB is an Ultra-Violet (UV) sensitive polymer that can be patterned directly with UV exposure and subsequent solvent development. However, it is difficult to achieve vertical profiles with direct patterning. The photo BCB is a similar material to the dry-etch BCB after curing and can also be dry etched with a similar process. Thermally cured dry-etch BCB (Cyclotene™ 3022-63) with a lower refractive index was used as the lower cladding; photo BCB (Cyclotene™ 4024-40) with a higher refractive index was UV cured but without solvent development and was used as the core layer for our fabrication.

5.1.2. Processing Procedures

General processing procedures for the circular grating DMUX fabricated with the BCB polymers are shown in Fig. 5-1. Details of processing parameters are listed in Appendix C, except for the dry etching of BCB polymers, which is discussed in the next section. After the 4 *in* silicon wafers were cleaned, AP3000 [57] was applied to promote adhesion between the dry-etch BCB polymer and the silicon substrate. Since a fully cured polymer leaves few open surface bonds for adhesion, the 10 μm lower cladding layer dry-etch BCB was partially cured (210 $^{\circ}C$ for 40 *min* in a vacuum oven) to enhance adhesion to the subsequent core layer photo BCB. The 10 μm thick photo BCB was then spun on and UV-cured. No

solvent development was applied and the resultant film thickness was thicker than if developed [49].

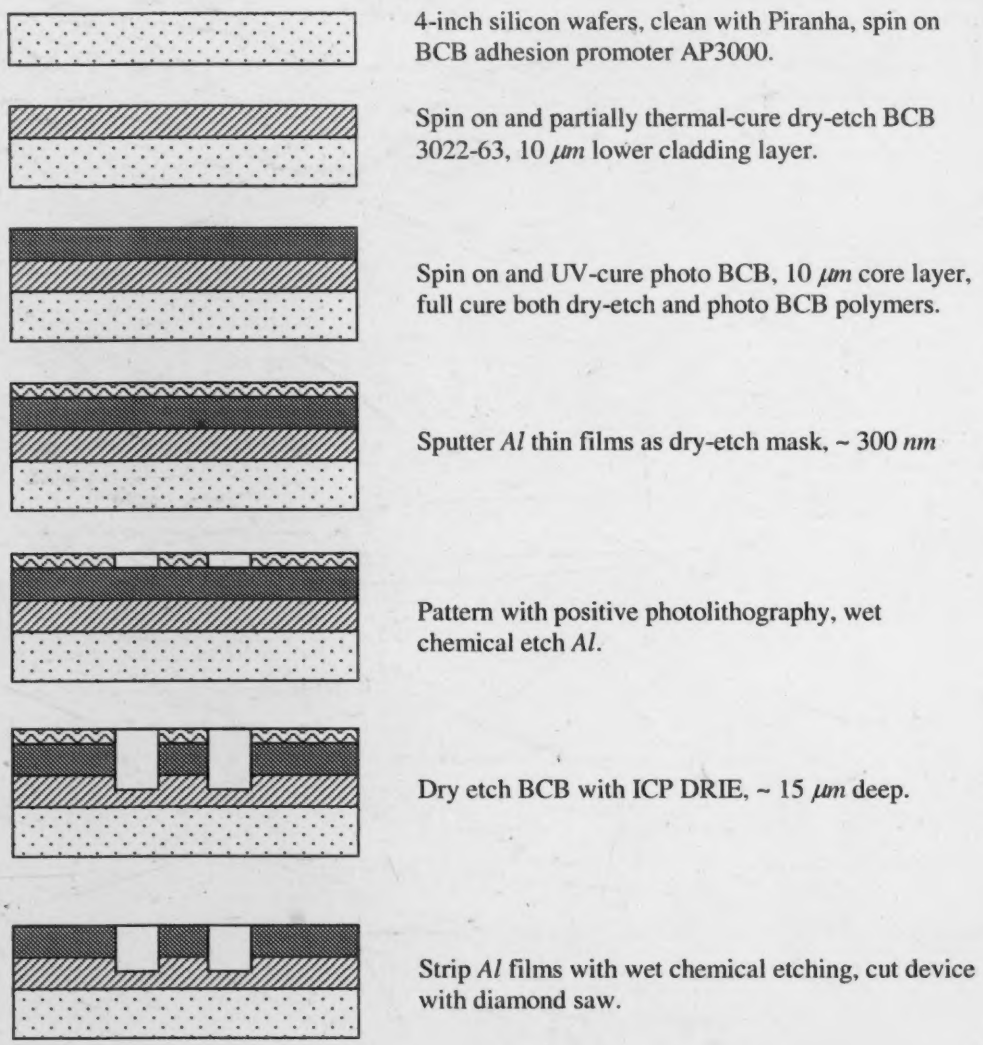
4-inch silicon wafers, clean with Piranha, spin on BCB adhesion promoter AP3000.
Spin on and partially thermal-cure dry-etch BCB 3022-63, 10 μm lower cladding layer.
Spin on and UV-cure photo BCB, 10 μm core layer, full cure both dry-etch and photo BCB polymers.
Sputter Al thin films as dry-etch mask, ~ 300 nm
Pattern with positive photolithography, wet chemical etch Al.
Dry etch BCB with ICP DRIE, ~ 15 μm deep.
Strip Al films with wet chemical etching, cut device with diamond saw.

Fig. 5-1. Process procedures for circular DMUX fabricated with BCB polymers.

An exposure time of 20 *s* was used to over-cure the polymer, since it has been reported that an inadequate dose results in polymers insufficiently cross-linked, with film swelling and peel-off during subsequent processes [58]. After exposure, both the BCB polymers were fully cured at 250 °*C* for 1 *hr* in a vacuum

oven. A long oven temperature ramp time was also applied for both the thermal curing processes to avoid thermal stress in polymers.

Because of the silicon content, dry etching of BCB polymers normally requires the use of either *F*- or *Cl*-based etching gases. Oxygen is also needed to etch the organic contents. These etching gases and the deep etching requirement exclude soft masks (photoresists) and hard masks such as SiN_x [59] and SiO_2 [60], and leave only those metal masks with good adhesion [61, 62] to BCB polymers. Three metal masks were tested and Fig. 5-2 shows the etching depths (including BCB and mask) measured with profilometer after different etching times.

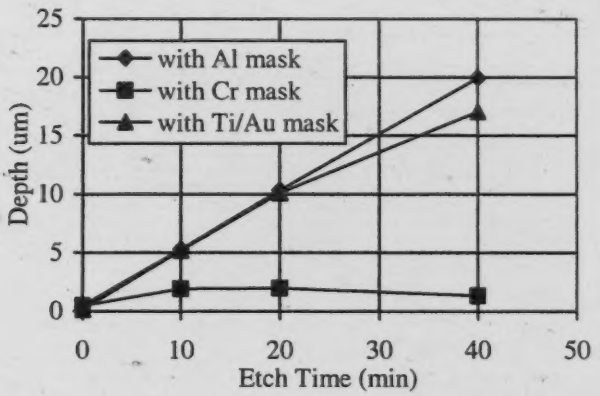

Fig. 5-2. Etching depth vs. etching time with different metal masks.

The original mask thicknesses were 455 *nm*, 465 *nm* and 146 *nm* for *Al*, Chromium (*Cr*), and Titanium/Gold (*Ti/Au*), respectively. The etching was conducted at gas flow rates of 2 *sccm* for SF_6 and 10 *sccm* for O_2, the chamber pressure *P* was set to 4 *mTorr*, the forward RIE RF power was 30 *W*, and the ICP plasma RF power was 750 *W*. From Fig. 5-2, the *Cr* mask cannot endure even 10 *min* of etching. The *Cr* mask is completely etched after 20 *min* and the now uncovered BCB is etched faster than the originally open areas due to the difficulties for the etching species to get into the etched trenches at the originally open areas. Therefore, the etching depth at 40 *min* becomes smaller than that at 20 *min*. The *Ti/Au* mask is etched through between 20 *min* and 40 *min*. The *Al* mask is not completely etched after 40 *min* with a BCB etching depth of approximately

20 μm, based on the constant slope of its curve in Fig. 5-2. Hence, *Al* is chosen for our experiments due to its high etching selectivity to BCB polymers.

A deep etching, at least through the core layer, is required for high reflectivity of the grating facets. The etching depth is 15 μm to form the ridge waveguide shown in Fig. 5-1. A thin *Al* dry-etch mask is desired for easy mask patterning and low stress. However, it must be thick enough to endure the deep etching process because of its finite etching selectivity to BCB polymers.

5.1.3. Optimizations of DRIE for BCB

Plasma etching of dry-etch BCB polymers has been reported with RIE [56, 59, 60 and 63], ICP RIE [64, 65], and Electron Cyclotron Resonance (ECR) RIE [55, 66]. The advantage of the high plasma density etching (ICP [67] and ECR) compared to conventional RIE is the separated plasma generation and plasma sheath electrical potential, controlled by separated RF power sources, so that the chemical component and the physical component of the plasma etching process can be separately controlled and optimized. Due to the similarity between the BCB polymers and the protective polymers used to passivate silicon sidewalls, the Bosch process [68] for deep silicon etching cannot be used for BCB [64]. An Oxford Plasma System 100 (ICP RIE) was used for our experiments. Cryogenic substrate cooling option was not available for this system at the time these experiments were conducted. Although many papers have been published on BCB etching, the etching conditions depend on and need to be optimized for the exact etching system used. According to the best of our knowledge, a vertical etching depth of over 10 micrometers for BCB polymers is the first known attempt.

A series of experiments was conducted at different gas flow compositions. The etching gases were SF_6 and O_2 with a total gas flow rate of 50 *sccm*, sufficiently large to avoid etchant depletion because the blank silicon wafer used to hold the small BCB etching samples is itself etchable in the plasma. The chamber pressure was set to the lowest achievable with the capability of the pumping system. A low chamber pressure is expected to facilitate the transportation of the etching species and etching byproducts, thus increases the

etching rate and affects the etched surface roughness [69]. Lower chamber pressure also means longer mean free paths, thus makes the etching reaction more directional. Fig. 5-3 shows the effect of the percentage of SF_6 gas flow on the measured BCB etching rate. Except for very low SF_6 contents, the BCB etching rate follows the trend of the measured DC bias voltage.

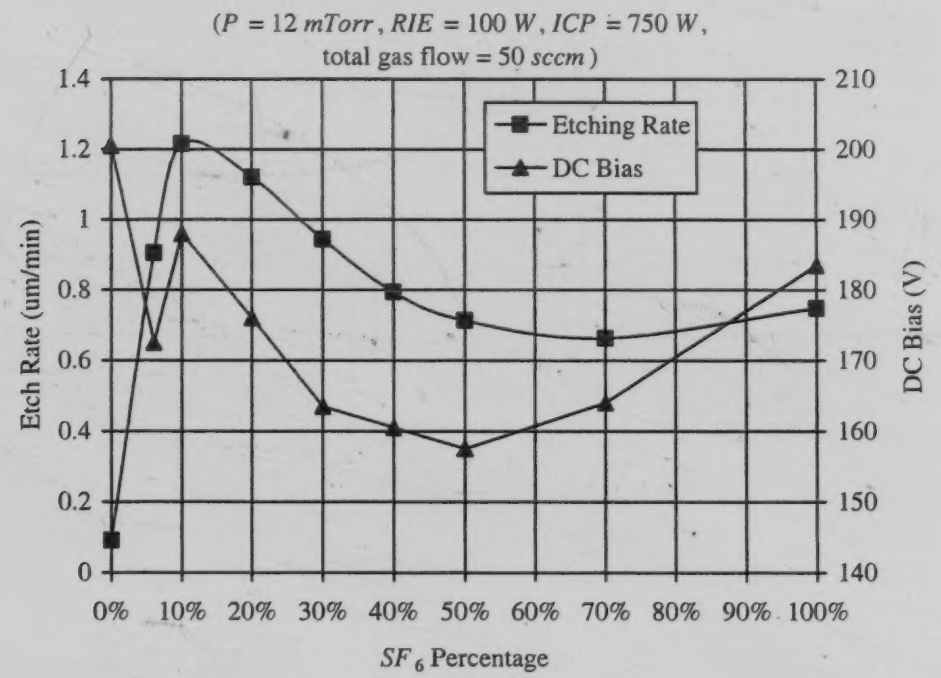

Fig. 5-3. Effect of etching gas composition on BCB etching rate.

Another series of experiments was conducted at different forward RIE powers, as shown in Fig. 5-4. The measured DC bias voltage is found to be approximately linear with the RIE power. Again the etching rate follows the trend of the DC bias voltage but the slope flattens out at high RIE powers. A small total gas flow was used because these experiments were done for whole device wafers with a small total open area exposed to the plasma, so that etchant depletion is not expected to be a problem as in the case where small BCB samples are clued to a blank silicon wafer. It was also found that silicon is etched faster than BCB polymers under these etching conditions.

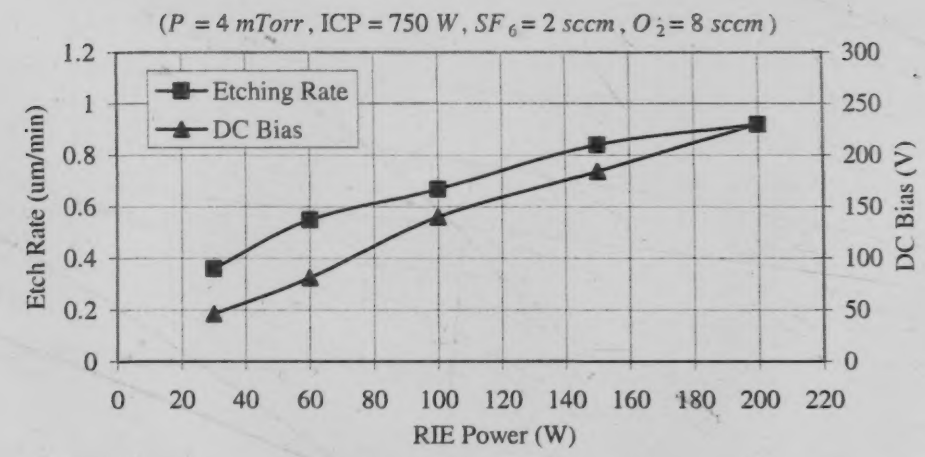

Fig. 5-4. Effect of RIE power on BCB etching rate.

The DC bias voltage is the electrical potential measured between the plasma sheath and the etching samples. It accelerates ions generated in the plasma toward the etching samples. The bombardment of the ions transfers energy to accelerate the reaction of the BCB polymer with the neutral radicals generated in the plasma. With higher DC bias voltages, the trajectories of the ions are more normal to the sample surfaces, hence the etched sidewall is more vertical, as shown in Fig. 5-5, which compares the profiles of the BCB waveguides etched with RIE powers of 30 *W* and 100 *W*, respectively. The sidewall profile angles measured from these SEM pictures are approximately 5° and 1.5°, respectively.

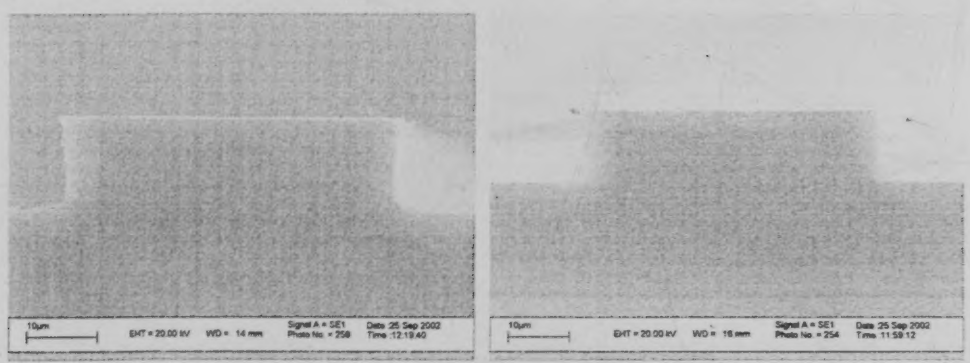

Fig. 5-5. BCB waveguides etched at RIE powers of 30 W (left) and 100 W (right).

However, as shown in Fig. 5-6 which compares the sidewalls of two samples etched with RIE powers of 100 *W* and 200 *W*, respectively, high energy ion bombardment causes physical sputtering of the etching mask and leads to severe mask retreat which leaves a horizontal fracture in the BCB sidewall (right picture of Fig. 5-6). A higher DC bias voltage is also more faithful in translating the mask edge roughness into the BCB sidewall and forms more obvious columnar/needle microstructures, as shown in Fig. 5-6. Other etching conditions for both Fig. 5-5 and Fig. 5-6 were the same as shown in Fig. 5-4.

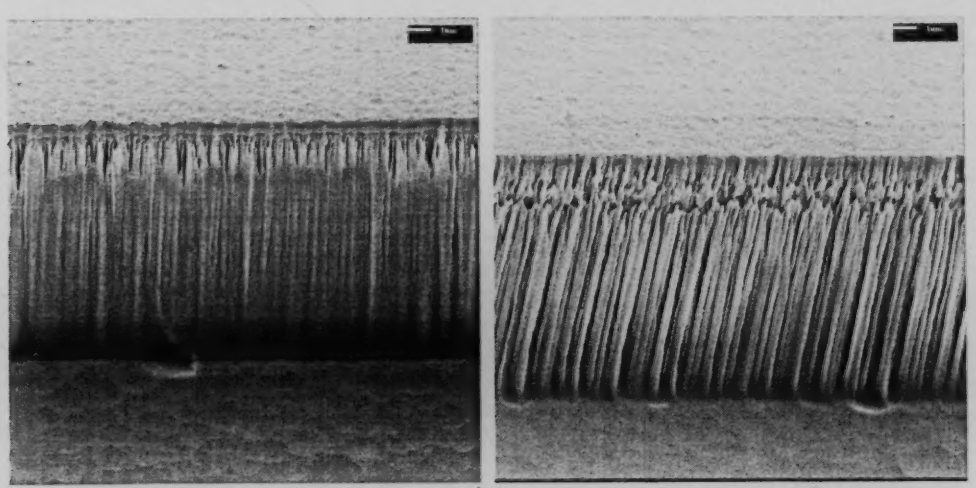

Fig. 5-6. BCB sidewalls etched at RIE power of 100 W (left) and 200 W (right).

The sidewalls etched with SF_6 in our experiments have a positive profile angle as shown in Fig. 5-5, while BCB etched with CF_4 in ECR RIE is reported to have a negative angle [55], which could be the result of sidewall passivation caused by polymer byproducts in the CF_4 etching process. Therefore, both the sidewall smoothness and verticality could be improved by mixing SF_6 and CF_4 gases. To verify this, three samples were etched with $P = 4$ *mTorr*, $ICP = 750$ *W*, $RIE = 60$ *W* with gas flows $SF_6 = 2$ *sccm*, $O_2 = 8$ *sccm*; $CF_4 = 3$ *sccm*, $O_2 = 8$ *sccm*; and $SF_6 = 2$ *sccm*, $CF_4 = 3$ *sccm*, $O_2 = 16$ *sccm*, respectively. The first two sets of gas flow rates have the same *F* content, while the last set is an equal mixture of the gas flows in the first two sets. The etching rates were found to be 0.55, 0.2, and 0.67 $\mu m/min$, respectively, with DC bias at 81, 120, and 113 *V*, respectively. SEM pictures of the etched sidewall profiles and surfaces are shown in Figs. 5-7,

5-8 and 5-9 for the three sets of etching conditions, respectively. The sidewall profile angles are approximately 3.5°, -1.5° and 3°, respectively. Although the improvement in sidewall verticality is not obvious, the sidewall surface is much smoother with the mixture of the etching gases (Fig. 5-9 compared to Fig. 5-7).

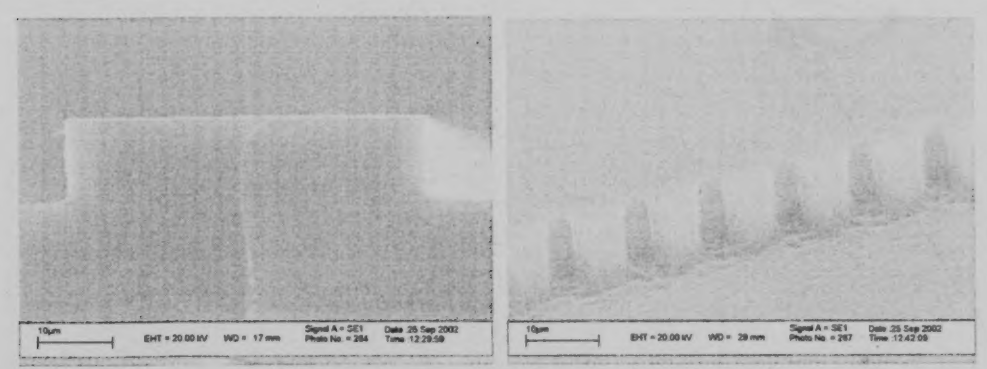

Fig. 5-7. BCB etched with $SF_6 + O_2$.

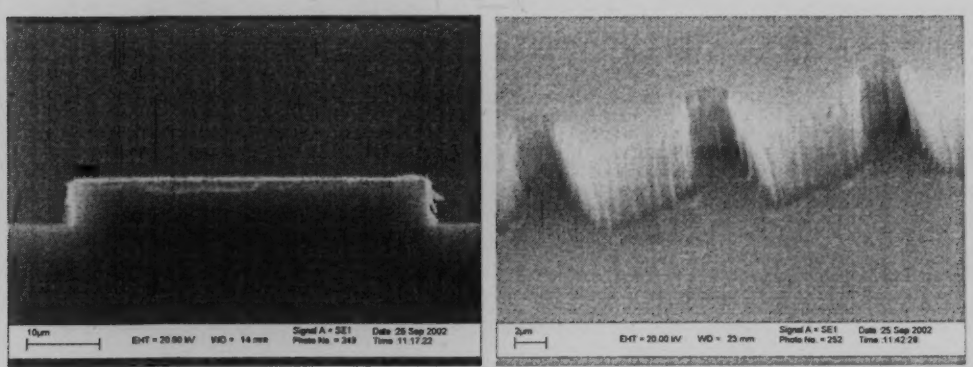

Fig. 5-8. BCB etched with $CF_4 + O_2$.

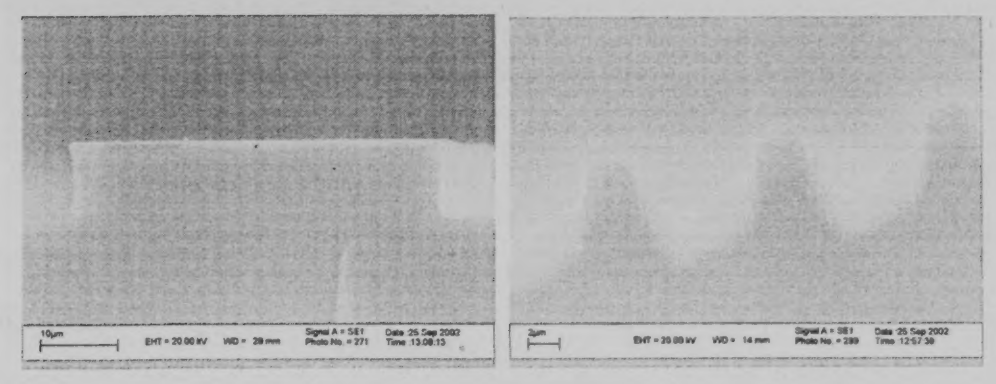

Fig. 5-9. BCB etched with $SF_6 + CF_4 + O_2$.

Based on these experiments, the RIE power should take a low value to avoid mask erosion and to reduce sidewall roughness. As mentioned before, chamber pressure should be as low as possible. The three sets of etching conditions shown in Table 5-1 were used to etch three wafers for device testing. Due to time constrains, the etching conditions for the mixture of SF_6 and CF_4 gases (Set 3) has not been optimized. The flow rates were chosen to simply give a 1:1 content of F from these two etching gases. The O_2 gas flow rate was double compared to Set 2 so that a constant F content is maintained. A high total gas flow rate (Set 1) is found to give little improvement on the etching rate (referring to Fig. 5-4). A higher ICP power of 1000 W was used in Set 3 to obtain a higher plasma density. However, the etching rate was found to be lower than that for Fig. 5-9 due to the reduced DC bias voltage. This confirms that the BCB etching in F-based gases is mainly a chemical process enabled by the neutral radicals but facilitated by the energy transferred from the ion bombardment.

Table 5-1. BCB etching conditions for device testing.

	Set 1	**Set 2**	**Set 3**
Fluorine gas flow (*sccm*)	$SF_6 = 10$	$SF_6 = 2$	$SF_6 = 2$, $CF_4 = 3$
Oxygen gas flow (*sccm*)	$O_2 = 40$	$O_2 = 8$	$O_2 = 16$
Chamber pressure *P* (*mTorr*)	8	4	6
RIE power (*W*)	30	30	60
ICP power (*W*)	750	750	1000
DC bias (*V*)	56	29	69
Actual chamber pressure (*mTorr*)	12.0	5.9	9.4
Etching rate (*μm/min*)	0.383	0.460	0.531
Etching time (*min*)	35	30	25

SEM pictures of the etched BCB samples using the three sets of etching conditions in Table 5-1 are shown in Figs. 5-10, 5-11 and 5-12, respectively. The sample shown in Fig. 5-11 is a circular grating without the retro-reflecting TIR facets while the other two are circular gratings with the retro-reflecting TIR facets. The sidewall tilt angles measured from these SEM pictures are approximately 5°, 2.5° and 1°, respectively. Test results of the samples etched with these three sets of etching conditions will be given in Chapter 6.

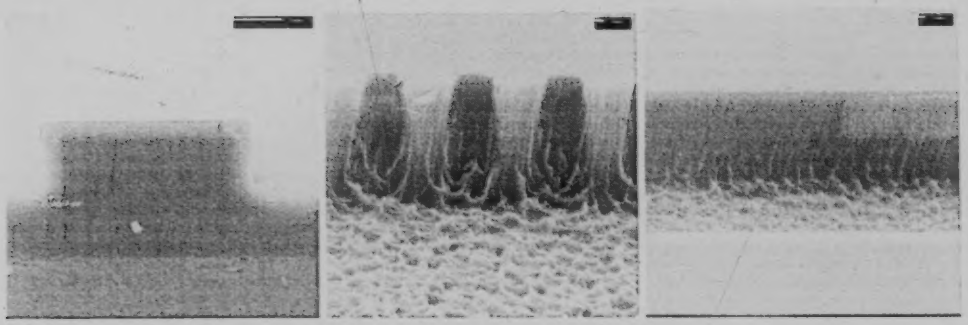

Fig. 5-10. waveguide cross-section (left), grating (middle) and sidewall surface (right) of BCB etched with Set 1 conditions.

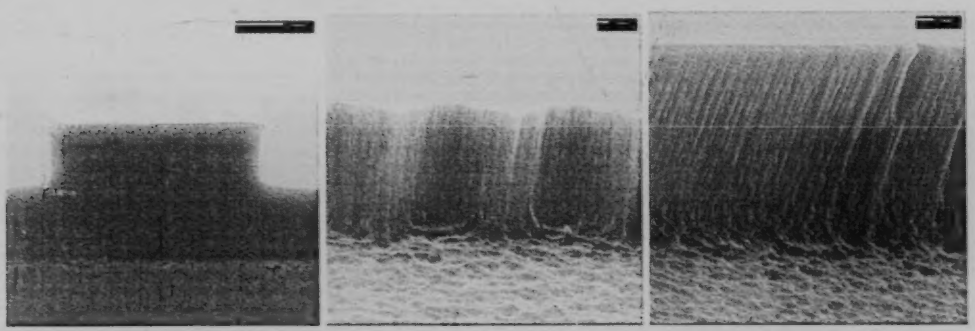

Fig. 5-11. waveguide cross-section (left), grating (middle) and sidewall surface (right) of BCB etched with Set 2 conditions.

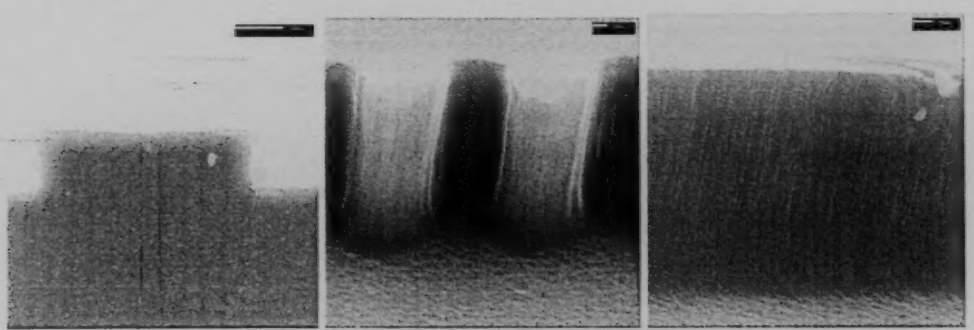

Fig. 5-12. waveguide cross-section (left), grating (middle) and sidewall surface (right) of BCB etched with Set 3 conditions.

5.2. DMUX Fabrication with LIGA Process

LIGA is the German acronym for x-ray lithography (x-ray lithographie), electrodeposition (galvanoformung) and molding (absormetchnik) [70]. It uses

extremely short (2 to 10 $\AA$) wavelength x-rays generated with synchrotron radiation to expose thick resists and obtain tall structures with high aspect ratios, which can then be used to generate metal masks with electroplating for molding such as hot embossment of plastics. The x-ray resists are usually poly(methylmethacrylate) (PMMA) polymers with good optical properties in the visible and near IR range. Due to the short wavelength of the x-rays, which reduces diffraction effects, the exposed resist structures can have vertical sidewalls and the resist thickness can be from micrometers up to millimeters.

The first step in the LIGA process, i.e. the generation of the mask in the PMMA resist, was used for our fabrication of concave grating DMUXes. The processing was conducted in Forschungszentrum Karlsruhe, Germany. The required PMMA optical waveguides with a thickness of 50 μm are thinner than the normal resists used. With thick layers, a polymer tape can be cut and then bonded to the substrate. The first version (LIGA version 1) of the test devices was fabricated with spin-on coating and subsequent on-wafer thermal curing which resulted in thermal cracks in the PMMA polymer as shown in Fig. 5-13. These cracks result in high optical transmission loss in the slab region. However, there is no crack in the input and output waveguides due to their small dimensions, and these waveguides were used for waveguide transmission loss testing in Chapter 6.

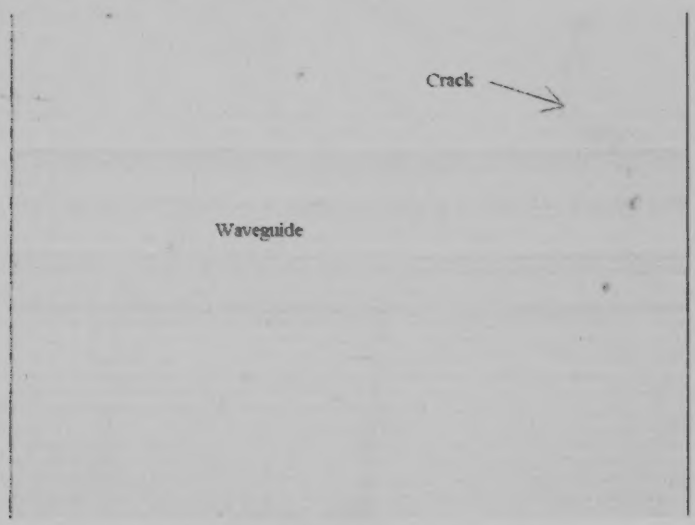

Fig. 5-13. LIGA version 1 process: cracks in PMMA.

A circular concave grating DMUX with retro-reflecting TIR facets (as specified in Table 2-1) was also fabricated with the LIGA process for process evaluation (the actual H = ~ 50 μm, n_1 = 1.49 and n_2 = 1.45). SEM pictures of this circular grating DMUX are shown in Fig. 5-14. The PMMA structure is 58 μm thick measured from the SEM pictures and has a vertical profile and smooth sidewalls.

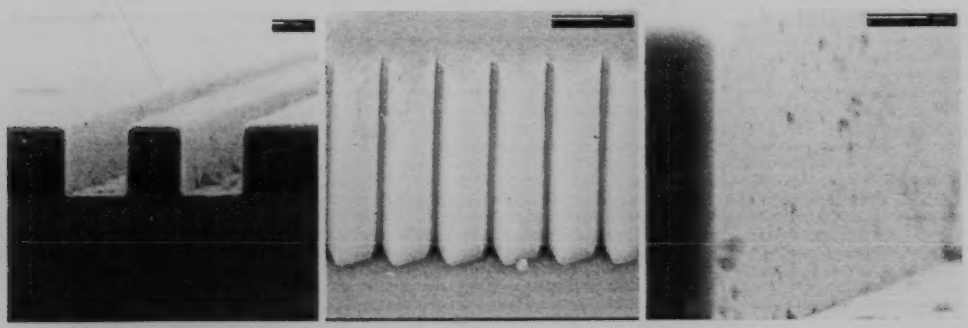

Fig. 5-14. waveguide cross-section (left), grating (middle) and sidewall surface (right) of PMMA fabricated with LIGA version 1 process.

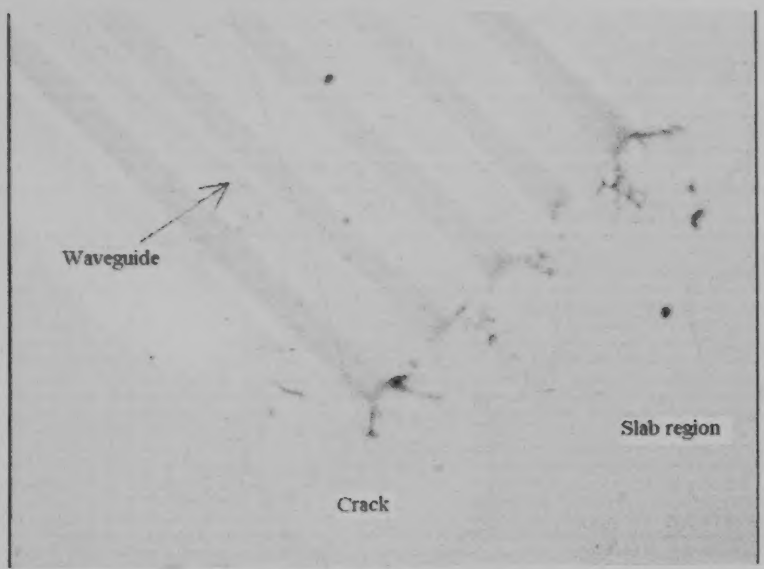

Fig. 5-15. LIGA version 2 process: small cracks in the joints between waveguides and slab region.

A second version (LIGA version 2) of test devices was fabricated with a different polymer thermal curing process and resulted in fewer cracks. There is no

crack observable in the slab region or the input and output waveguides. However, small cracks occurred at the joints between the waveguides and the slab region. A microscope picture is shown in Fig. 5-15. Unfortunately, these joints are critical because it is there that light is coupled to the slab waveguide. These small cracks render the device unusable. The fabricated PMMA structures are similar to those fabricated with the LIGA version 1 process shown in Fig. 5-14.

The PMMA polymer was also found to have poor adhesion to the thermal SiO_2 used as the lower cladding layer. The waveguide peeled away from its original position when cleaned with de-ionized (DI) water and dried with N_2 gas during polishing, as shown in Fig. 5-16. Further work is needed and is underway to solve the polymer crack and adhesion problems in the LIGA process.

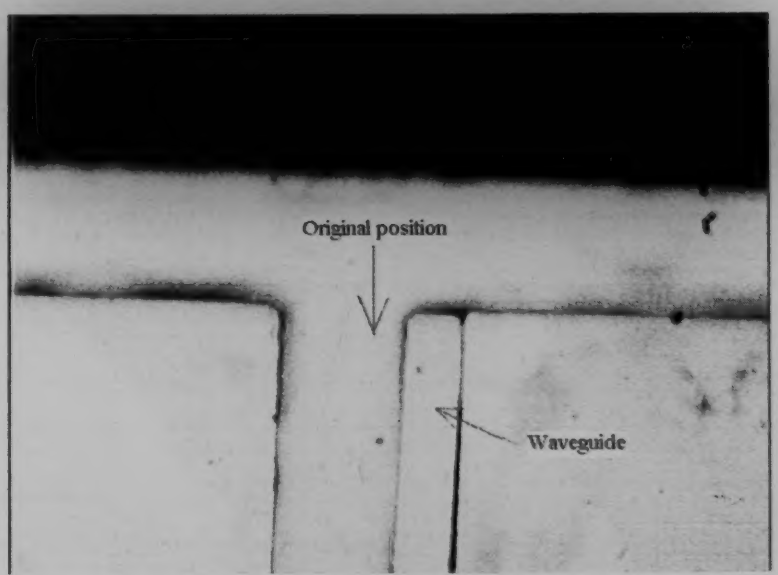

Fig. 5-16. LIGA version 2 process: waveguide moved due to poor adhesion.

5.3. Summary

The thermal crack and poor adhesion of PMMA polymer in the LIGA process are caused by the thermal coefficient dismatch between the polymer and the underlying SiO_2, and can be overcome by optimizing the polymer thermal cure process, using a polymer with a thermal coefficient close to that of PMMA

as the lower cladding layer, or using a thicker PMMA polymer layer which can be bonded to the substrate without on-wafer thermal curing.

The SEM pictures of BCB samples fabricated with DRIE and PMMA samples fabricated with the LIGA process clearly suggest that the LIGA process is preferred for more vertical and smooth sidewalls. However, the LIGA process is expensive and requires specific synchrotron radiation facility, and thus is not ideal for mass production, but is preferred for evaluation of the design concepts. The dry etching process of BCB polymers can be further improved with a systematic experimental approach. However, it is not clear at this stage as to how much further improvement can be gained.

6. Test of Waveguides and Demultiplexers

This chapter presents the testing results of the devices fabricated with DRIE of BCB polymers and with the LIGA process of PMMA polymer. Due to the difficulties in processing, no numeric test results of the DMUX devices can be obtained at this point. Examinations of the fabricated devices and testing of the waveguides suggest directions for future improvements.

6.1. Test Setups

The setup schematically shown in Fig. 6-1 was used to test the circular concave grating DMUX. An array of five MMFs was precisely positioned using a standard silicon V-groove chip with fibers spaced at 1 *mm*, matching the spacing of S-bend waveguides designed on the DMUX chip. A grating based tunable diode laser was used as the light source and the fiber array was butt-coupled to the cleaved and polished device edge using a precision optical coupling stage. Light output from MMFs was measured with an optical detector and power meter.

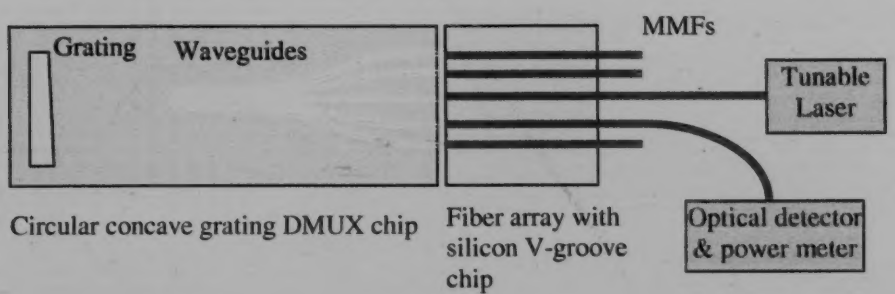

Fig. 6-1. Test setup for circular concave grating DMUX chracterization.

Due to the large difference between the dimensions of the 50 μm core diameter MMFs and the 50 $\mu m \times 10$ μm BCB optical waveguides, a high coupling loss is expected. The coupling loss can be roughly estimated with the geometric area ratio between the MMF core and the waveguide core, and is found to be approximately 6 *dB*. This estimation assumes uniform field distributions on the

waveguide and fiber core areas, and does not take into account the mode-coupling efficiency. The test setup for the elliptic concave grating DMUX was similar, with light launched into the chip through a single MMF on one edge and the same fiber array butt-coupled to the other edge, although only four MMFs are actually needed.

Waveguide transmission losses were measured with the cutback method, which measures optical power transmitted through an optical waveguide at different waveguide lengths with a constant input optical power. The cutback method assumes that the waveguide edges are similar after successive cuts and that the coupling between the fiber and the waveguide is repeatable so that the insertion loss variation is all due to the waveguide transmission loss. Light was butt-coupled into and out of the waveguide using step index MMFs with a core diameter of 50 μm. At each waveguide length, three independent tests were conducted after completely decoupling and then re-coupling the fibers with the waveguide. The average was then taken as the insertion loss. No index matching fluid was used in all tests. Due to the high transmission loss of the fabricated BCB waveguides, only very short (centimeters or shorter) waveguides could be tested. LIGA PMMA waveguides were cut from the input/output waveguides of the DMUX chips and were also short in length.

6.2. Test Results of BCB DMUXes and Waveguides

With an approximate 6 mW of input optical power at 810 nm from a tunable laser, it was seen with an IR camera that light was coupled into the central straight waveguide of the circular DMUX chip. Only weak light spots on the grating facets could be observed. However, there was no output optical power (in the order of nW) measured with the optical power meter for all samples fabricated with the three sets of etching conditions shown in Table 5-1, regardless of the input wavelength from 790 nm to 830 nm. The waveguides appeared to have extremely high transmission loss.

Fig. 6-2 shows the effect of waveguide length on insertion loss for the straight BCB waveguides etched with the Set 2 etching conditions in Table 5-1. The input power was 6.918 *mW* (laser operation current 60 *mA*) at 810 *nm* wavelength. The waveguide edges were not polished after cleaving. The coupling loss is found to be 3.6±0.9 *dB* (7.2 *dB* for two couplings: coupling in and coupling out) from the linear fit in Fig. 6-2 and is better than the geometric area estimation of 6 *dB*, which does not take into account the actual mode field profiles. The transmission loss is extremely high at 18.1±1.5 *dB/cm*. The standard deviations were calculated from the measured and the linearly fitted insertion loss data in Fig. 6-2.

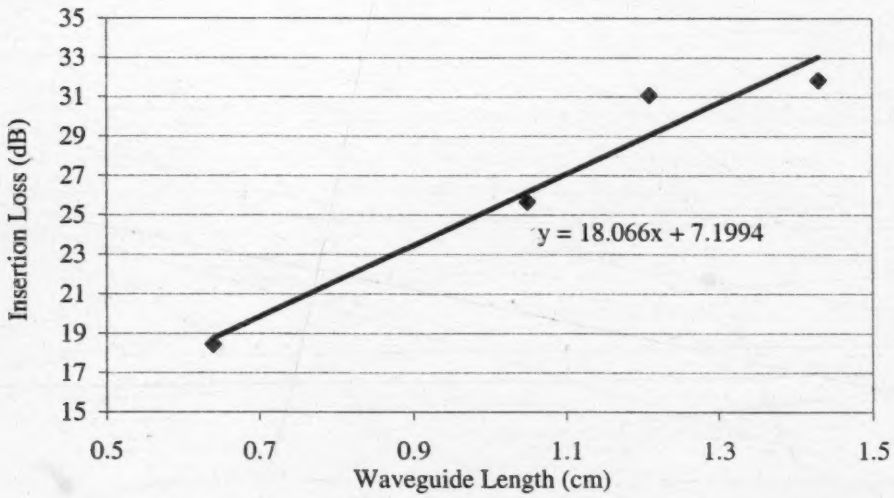

Fig. 6-2. Insertion loss of BCB waveguides etched with Set 2 conditions.

BCB waveguides fabricated with the Set 3 etching conditions in Table 5-1 were also tested and the results are shown in Fig. 6-3. Test conditions were the same as for those etched with the Set 2 conditions (Fig. 6-2) except that the cleaved edges were polished with 9 μm disks. Polishing with finer disks was found to easily cause damage to waveguide corners. The coupling loss read from Fig. 6-3 is 7±0.3 *dB*, higher than that from Fig. 6-2 and this leads to the conclusion that polishing actually increases the coupling loss. This might be due to the micro-cracks created at the edges of the soft polymers during the

mechanical polishing. The waveguide transmission loss is 10.5±0.7 *dB/cm*, lower than in Fig. 6-2. A comparison of Fig. 5-11 (Set 2 etching conditions) and 5-12 (Set 3 etching conditions) reveals that the sidewall surface etched with the Set 3 conditions is smoother than that etched with the Set 2 conditions.

Waveguides etched with the Set 1 etching conditions were not tested due to their high loss. With 2 *cm* long input and output waveguides, the waveguide insertion loss from Figs. 6-2 and 6-3 will cause the DMUX devices to have little output optical power.

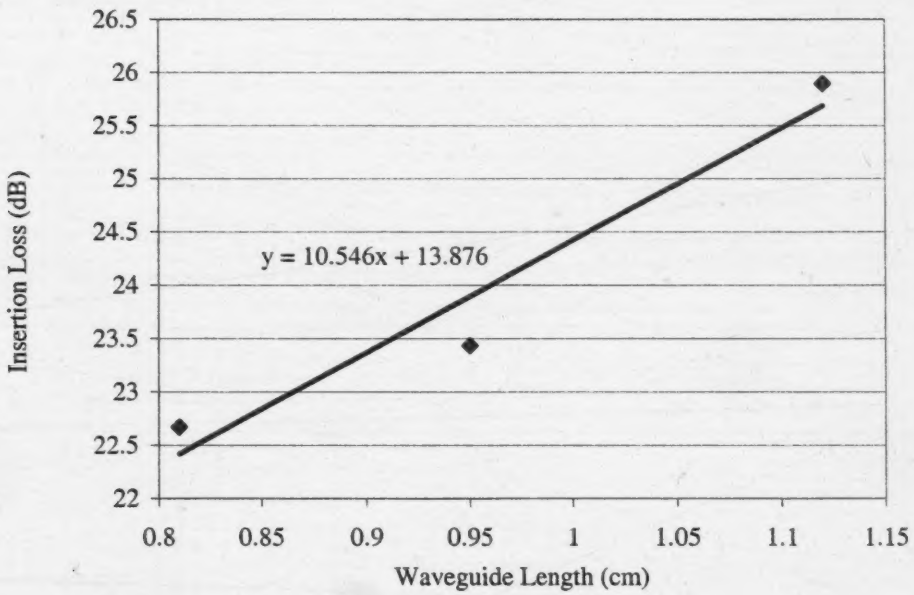

Fig. 6-3. Insertion loss of BCB waveguides etched with Set 3 conditions.

The last cut of the waveguide in Fig. 6-2 (0.64 *cm* long) was also tested at different input wavelengths to observe the relationship between the waveguide transmission loss and the optical wavelength. After the coupling between the input/output MMFs and the waveguide was optimized with a maximum output power at 810 *nm*, the input wavelength was varied by tuning the tunable laser from 790 *nm* to 830 *nm*, and for other wavelengths, by replacing lasers. No further adjustment of the coupling was performed. The results are shown in Fig. 6-4. The insertion loss is lower at longer wavelengths. If the coupling loss of 3.6

dB from Fig. 6-2 is assumed to be constant with wavelengths, then the transmission loss at 1480 *nm* can be calculated from Fig. 6-4 to be 3.4 *dB/cm*, which is much lower than 18 *dB/cm* at 810 *nm*. The transmission loss at 1480 *nm* is expected to be even lower for waveguides fabricated with the Set 3 etching conditions as in Fig. 6-3. This confirms that the transmission loss in the fabricated BCB waveguides is strongly limited by the sidewall surface roughness, since the Rayleigh scattering loss has a wavelength dependence of $1/\lambda^4$. Therefore, waveguides working in shorter wavelength ranges require much smoother etched sidewall surfaces.

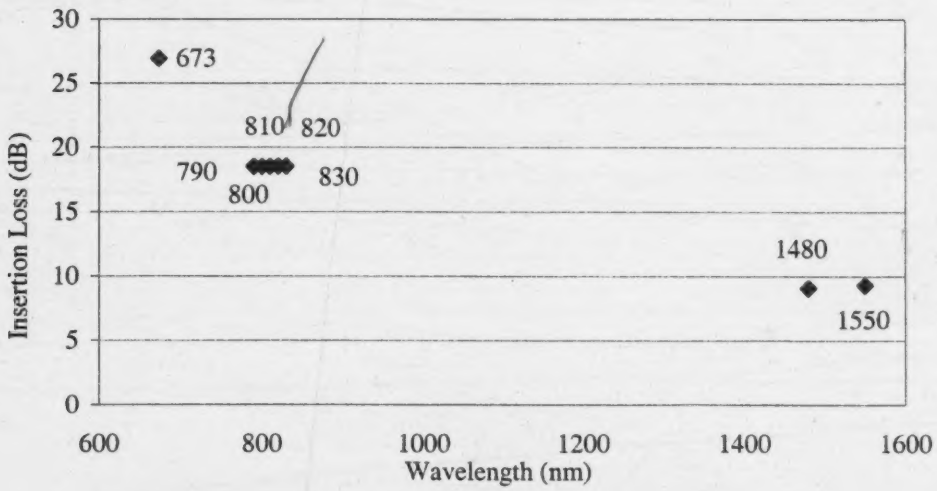

Fig. 6-4. Waveguide insertion loss vs. input wavelength for 0.64 cm long BCB waveguide etched with Set 2 conditions.

An inspection of the fabricated devices shows that the BCB films appear to be dark yellow in color, which means the BCB polymers were oxidized during thermal curing. Oxidation has been reported to result in an increase in optical absorption [71] and a change in refractive index [72]. It is recommended that the thermal curing be conducted in environments with an oxygen level below 100 *ppm*. Vacuum ovens with N_2 purging were not available at the time these devices were fabricated. BCB thermal curing was conducted in a vacuum oven with oxygen levels possibly higher than 100 *ppm*.

Future improvements should include more efforts to optimize the DRIE process for smooth sidewall surfaces, as well as to avoid oxidation of the BCB polymers with N_2 purging during their thermal curing processes.

6.3. Test Results of LIGA PMMA DMUXes and Waveguides

Test results of the LIGA version 1 PMMA waveguides are shown in Fig. 6-5 using the same cutback method. 9 μm disks were used to polish waveguide edges after cleaving. The coupling loss is found to be 1.8±0.0002 *dB* and the transmission loss is 1.4±0.0005 *dB/cm*. Such a low coupling loss is expected with the 57.7 μm × 47.2 μm core PMMA waveguides (measured from the SEM pictures in Fig. 5-14) and the 50 μm core diameter MMFs. An S-bend waveguide on the same sample was also tested and its insertion loss taking into account the total length of its curve is consistent with that of the straight waveguide. This confirms that light transmitted through the short open space and then coupled into the output fiber is negligible, as expected with the dimensions of the fibers and the waveguide.

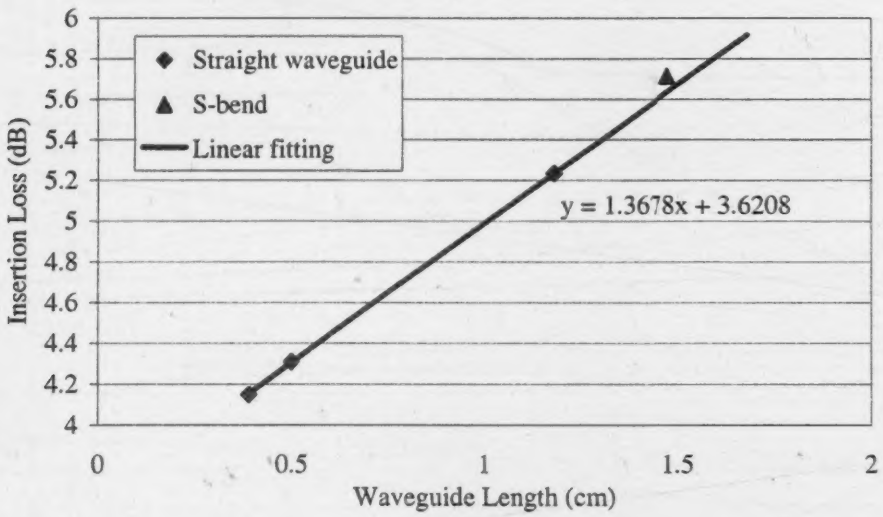

Fig. 6-5. Insertion loss of LIGA PMMA waveguides.

A test of an elliptic DMUX fabricated with the LIGA version 2 process showed a bright input waveguide under a camera and light could be seen reflected from the grating facets and focused at the output plane. However, no light could be detected from the output MMFs, regardless of the input wavelength in the designed wavelength range. In the presence of the micro-cracks shown in Fig. 5-15, coupling into the output waveguides is difficult. The circular DMUX fabricated with the LIGA version 2 process was also tested with its S-bend sections of the waveguides cut out after being damaged during polishing (PMMA films peeled off due to poor adhesion). Fig. 6-6 is a picture of the device under testing at 630 *nm* (visible light so that a good picture can be taken with the available camera).

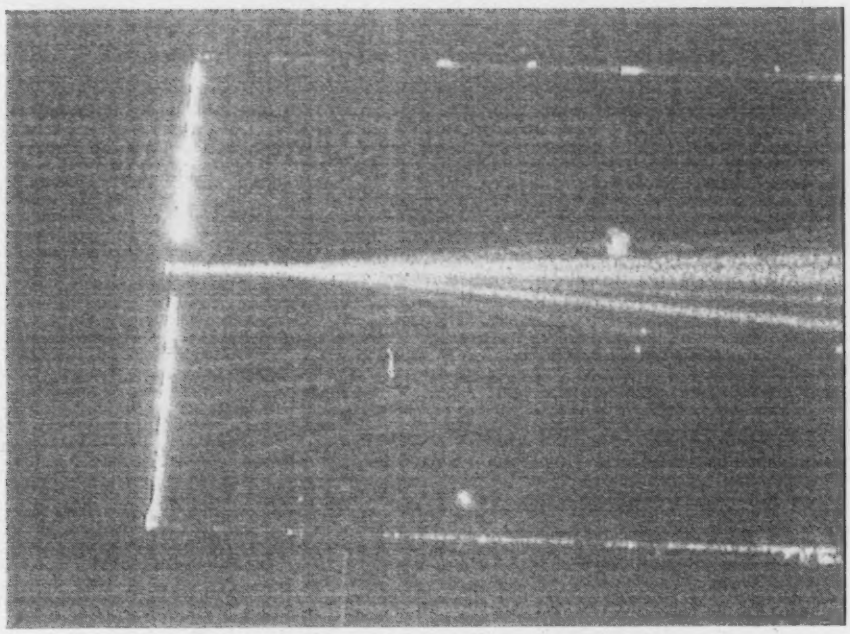

Fig. 6-6. Circular DMUX fabricated with LIGA version 2 process under testing.

The schematics in the bottom of Fig. 6-6 show the overall test setup, with the dashed box indicating the area shown in the camera picture above. Only approximately half of the device is shown in the picture due to the limited field of the camera. The input light can be seen on the left edge and expands in the slab region. As shown in Fig. 6-6, light reflected back from the grating facets forms multiple bright spots on the left edge, which are believed to correspond to the beams of different diffraction orders. Although no spectral test results can be obtained, the diffraction function of the grating can be confirmed from Fig. 6-6.

6.4. Summary

Tests of the fabricated BCB waveguides gives a transmission loss higher than 10.5 *dB/cm* for all fabricated samples. It also suggests that the loss is mainly limited by sidewall surface roughness of the optical waveguides. However, the loss is also found to be reasonable at longer wavelengths such as 1480 *nm* and 1550 *nm*. The short wavelength range (820 *nm*) used for the multimode DMUXes requires extremely smooth waveguide sidewall surfaces and further optimization of the DRIE process of BCB. The high waveguide transmission loss is a natural penalty for working on short wavelength ranges.

The waveguide test gives a transmission loss as low as 1.4 *dB/cm* at 810 *nm* for PMMA waveguides, and confirms the smooth sidewalls obtained with the LIGA process. The LIGA process is expected to give good device performance if the polymer crack and poor adhesion problems can be overcome, and should be preferred for proof-of-concept evaluation of the DMUX designs.

7. Conclusions and Suggestions for Future Work

7.1. Conclusions

Two planar concave grating DMUX configurations have been presented based on concentric circles and confocal ellipses, respectively. The elliptic concave grating DMUX (Chapter 4) is a generalization of the circular concave grating DMUX (Chapter 2). The main advantage with the elliptic DMUX (if TIR is satisfied) is the ease of microfabrication without backside metal coating for the grating facets or the use of retro-reflecting TIR facets, which degrade grating performance as analyzed in Chapter 3. The elliptic grating also has larger facet feature size than the circular grating at the same grating order, and is expected to be less sensitive to microfabrication imperfections. The main disadvantages include larger chip size and the complicated relationship between the design parameters and the resultant facet geometric layout. Theoretical derivations and two-dimensional scalar electromagnetic simulations have been developed and are presented for both grating configurations.

Common microfabrication imperfections for etched planar concave grating DMUXes have been analyzed with scalar electromagnetic modeling. These imperfections include grating facet surface roughness, facet corner rounding, etching undercut, etched sidewall tilt, and material refractive index variation. The analytical results suggest that the main source for performance degradation is the sidewall tilt, and that the elliptic grating is preferred to the circular grating. The analysis models and simulation results are applicable to other planar concave grating DMUXes.

Although most of the work in this thesis is for multimode CWDM applications in the 820 *nm* wavelength range, both the circular and the elliptic grating DMUXes can be used for singlemode CWDM or DWDM. The considerations for FSR and grating facet feature size in Chapter 2 (also applicable to the elliptic grating DMUX), the microfabrication imperfection analysis in

Chapter 3, and the waveguide test results in Chapter 6 all suggest that DMUXes working in long wavelength ranges are easier to design and less sensitive to microfabrication imperfections. For singlemode devices, the waveguide core layer thickness can be much smaller (micrometers) than for multimode CWDM (tens of micrometers). It is also easier to obtain good dry etching results in terms of sidewall roughness and verticality with shallow etching. For thin waveguide layers, other more mature and stable material systems can be used, such as the SiO_2/SiO_xN_y material system [73, 74] with a highly vertical etched profile obtainable in RIE [15]. Therefore, better results can be reasonably expected for DMUXes designed for singlemode CWDM or DWDM applications in long wavelength ranges.

As an example, the elliptic grating has also been designed for singlemode CWDM with 18 channels working in the standard ITU CWDM wavelength grid. Novel double parabolic waveguide horns have been proposed to flatten channel passbands and to reduce channel crosstalk. The simulation results are promising and can be further improved for a DMUX with less than full 18 channels.

A circular grating DMUX has been fabricated in BCB polymers with DRIE for multimode CWDM applications in the 820 *nm* wavelength range. No device test results can be obtained due to processing difficulties, but the inspection of the devices and the test of the waveguides suggest that the input/output waveguides are extremely lossy due to the surface roughness on the dry-etched sidewalls. The test results also suggest that a reasonable waveguide transmission loss much lower than 3.4 *dB/cm* is obtainable with the current process, if working in longer wavelength ranges such as the telecom wavelengths.

An elliptic grating DMUX has been fabricated in PMMA polymer with the LIGA process. Vertical and smooth sidewalls have been obtained. Device testing has confirmed the diffraction function of the circular concave grating. The waveguide testing gives a transmission loss of 1.4 *dB/cm* and a MMF to waveguide coupling loss of 1.8 *dB*.

7.2. Suggestions for Future Work

Further work is needed to optimize the BCB polymer etching process for smooth sidewall surfaces and to avoid polymer oxidation during thermal curing. Due to time constraints, the etching technique using the mixture of SF_6 and CF_4 gases has not been optimized and should have room for further optimizations to achieve smoother sidewalls. Based on the fabrication and test results in Chapters 5 and 6, the LIGA process is more promising to give good device performance and should be preferred for future work. For proof-of-concept, it would also be possible to design and fabricate singlemode DMUXes in other mature material systems such as SiO_2/SiO_xN_y. However, the SiO_2/SiO_xN_y material system is not suitable for multimode DMUXes with tens of micrometers thick waveguide core layers because of the technical difficulties and high cost associated with the deposition of thin films, usually with Plasma Enhanced Chemical Vapor Deposition (PECVD).

Further optimizations of the LIGA process need to be carried out to solve the polymer thermal crack and adhesion problems. One obvious solution would be to use a thicker PMMA layer, for example 100 μm or 200 μm, which is the normal PMMA resist thickness used in the LIGA process. Then both the polymer thermal crack and the poor adhesion can be avoided. Fig. 7-1 compares the spectral responses of the multimode elliptic DMUX in Table 4-1 with the original 50 μm thick PMMA core layer and with a thicker PMMA layer of 100 μm. There is no effect on the spectral responses for the fundamental mode with a thicker PMMA core layer.

A thick PMMA layer will not affect channel crosstalk either, because the effective mode wavelength range, as shown in Eq. (4-24), depends on the material indices but not the waveguide thickness. However, a higher coupling loss to the 50 μm core MMF is expected with a thicker PMMA layer due to the larger dismatch between the dimensions of the slab waveguide and the optical fiber. This alternation is now underway.

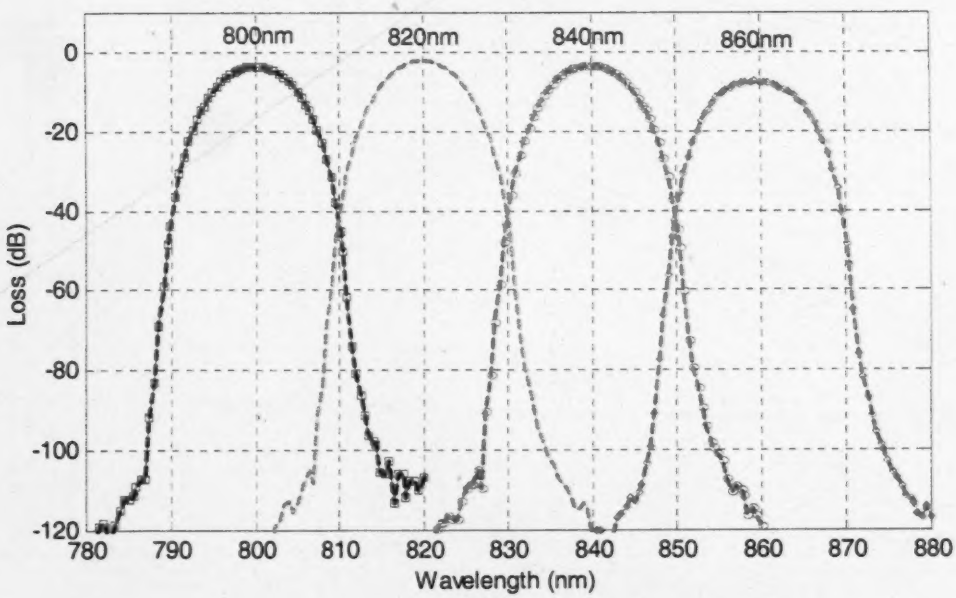

Fig. 7-1. Spectral responses of multimode elliptic concave grating DMUX with 50 μm (dashed) and 100 μm (solid) LIGA PMMA resist thickness, with only fundamental mode considered.

References

[1]. Gerd E. Keiser, "A Review of WDM Technology and Applications", *Optical Fiber Technology*, 5, pp. 3-39, 1999.

[2]. Jeff Hecht, "Coarse WDM: A Cost-effective Choice for the Short Haul", *Laser Focus World*, pp. 153-157, Jan. 2002.

[3]. ITU, *Spectral Grids for WDM Applications: DWDM Frequency Grid*, ITU G.694.1, June 2002.

[4]. Santanu Das, "Coarse Wavelength Division Multiplexing - Riding the Wave of Low Cost for Metro and Access", *Business Briefing: Global Optical Communications*, 2002.

[5]. B. R. Eichenbaum and S. K. Das, "Economics for Choosing a Coarse WDM Wavelength Grid", *Technical Proceedings of the 2001 National Fiber Optics Engineers Conference*, pp. 1444-1448.

[6]. ITU, *Spectral Grids for WDM Applications: CWDM Wavelength Grid*, ITU G.694.2, June 2002.

[7]. Yoshinori Hibino, "Passive Optical Devices for Photonic Networks", *IEICE Transactions on Communication*, Vol. E83-B, N0. 10, pp. 2178-2190, Oct. 2000.

[8]. Bedwyr Humphreys, and Emil Koteles, "Fabrication Challenges for Enabling Metropolitan WDM Network Technologies", *Compound Semiconductor*, pp. 87-94, July 2001.

[9]. Jon G. Bornstein, "Semiconductor Techniques Enhance Production of Planar Lightwave Circuits", *Optical Manufacturing*, pp. 25-29, March 2002.

[10]. P. C. Clemens, G. Heise, R. März, H. Michel, A. Reichelt, and H. W. Schneider, "8-Channel Optical Demultiplexer Realized as SiO_2/Si Flat-Field Spectrograph", *IEEE Photonics Technology Letters*, Vol. 6, No. 9, pp. 1109-1111, Sept. 1994.

[11]. J. B. D. Soole, A. Scherer, H. P. LeBlanc, N. C. Andreadakis, R. Bhat, and M. A. Koza, "Monolithic InP/InGaAsP/InP Grating Spectrometer for the 1.48-1.56 μm Wavelength Range", *Applied Physics Letters*, Vol. 58, No. 18, pp. 1949-1951, May 1991.

[12]. C. Cremer, E. Ebbinghaus, G. Heise, R. Müller-Nawrath, M. Schienle, and L. Stoll, "Grating Spectrograph in InGaAsP/InP for Dense Wavelength Division Multiplexing", *Applied Physics Letters*, Vol. 59, No. 6, pp. 627-629, Aug. 1991.

[13]. Jian-Jun He, Boris Lamontagne, André Delâe, Lynden Erickson, Michael Davies, and Emil S. Koteles, "Monolithic Integrated Waveguide Wavelength Demultiplexer Based on a Waveguide Rowland Circle Grating in InGaAsP/InP", *Journal of Lightwave Technology*, Vol. 16, No. 4, pp. 631-638, April 1998.

[14]. M. Fallahi, K. A. McGreer, A. Delâge, I. M. Templeton, F. Chatenoud, and R. Barber, "Grating Demultiplexer Integrated with MSM Detector Array in InGaAs/AlGaAs/GaAs for WDM", *IEEE Photonics Technology Letters*, Vol. 5, No. 7, pp. 794-797, July 1993.

[15]. Z. J. Sun, K. A. McGreer, and J. N. Broughton, "Demultiplexer with 120 Channels and 0.29-nm Channel Spacing", *IEEE Photonics Technology Letters*, Vol. 10, No. 1, pp. 90-92, Jan. 1998.

[16]. Emilio Gini, Werner Hunziker, and Hans Melchior, "Polarization Independent InP WDM Multiplexer/Demultiplexer Module", *Journal of Lightwave Technology*, Vol. 16, No. 4, pp. 625-630, April 1998.

[17]. J. Mohr, B. Anderer, and W. Ehrfeld, "Fabrication of a Planar Grating Spectrograph by Deep-etch Lithography with Synchrotron Radiation", *Sensors and Actuators A*, 25-27, pp. 571-575, 1991.

[18]. H. A. Rowland, "On Concave Gratings for Optical Purpose", *Philosophy Magazine*, Vol. 16, pp. 197-210, 1883.

[19]. K. A. McGreer, "A Flat-Field Broadband Spectrograph Design", *IEEE Photonics Technology Letters*, Vol. 7, No. 4, pp. 397-399, April 1995.

[20]. Seiji Toyoda, Akimasa Kaneko, Naoki Ooba, Makoto Hikita, Masato Tsukada, Takashi Kurihara and Tohru Maruno, "Polymer Tunable Wavelength Filter for WDM Systems", *IEICE Transactions on Electronics*, Vol. E83-C, No. 7, pp. 1119-1124, July 2000.

[21]. J. M. McMullin, R. G. DeCorby, and C. J. Haugen, "Theory and Simulation of a Concave Diffraction Grating Demultiplexer for Coarse WDM Systems", *Journal of Lightwave Technology*, Vol. 20, No. 4, pp. 758-765, April 2002.

[22]. Shing Man Lee, Weng Cho Chew, Mahta Moghaddam, Muhammad A. Nasir, Shun-Lien Chuang, Robert W. Herrick and Chester L. Balestra, "Modeling of Rough-Surface Effects in an Optical Turning Mirror Using the Finite-Difference Time-Domain Method", *Journal of Lightwave Technology*, Vol. 9, No. 11, pp. 1471-1480, Nov. 1991.

[23]. M. Saillard, E. Popov, L. Tsonev, and N. Kruse, "Light Diffraction from Rough Gratings", *Applied Optics*, Vol. 34, No. 22, pp. 4883-4891, Aug. 1995.

[24]. Peter Buchmann and Hans Kaufmann, "GaAs Single-Mode Rib Waveguides with Reactive Ion-Etched Totally Reflection Corner Mirrors", *Journal of Lightwave Technology*, Vol. LT-3, No. 4, pp. 785-788, Aug. 1985.

[25]. M. Born and E. Wolf, *Principle of Optics*, 6th edition, Pergamon Press, 1980.

[26]. Sonja Engman and Peter Lindblom, "Improving Echelle Grating Efficiencies", *Physica Scripta*, Vol. 28, pp. 86-88, 1983.

[27]. Sonja Engman and Peter Lindblom, "Blaze Characteristics of Echelle Gratings", *Applied Physics*, Vol. 21, No. 23, pp. 4356-4362, Dec. 1982.

[28]. E. Loewen, D. Maystre, E. Popov and L. Tsonev, "Echelles: Scalar, Electromagnetic, and Real-Groove Properties", *Applied Optics*, Vol. 34, No. 10, pp. 1707-1727, April 1995.

[29]. U. U. Graf, D. T. Jaffe, E. J. Kim, J. H. Lacy, H. Ling, J. T. Moore and G. Rebeiz, "Fabrication and Evaluation of an Etched Infrared Diffraction Grating", *Applied Optics*, Vol. 33, No. 1, pp. 96-102, Jan. 1994.

[30]. R. J. Deri, J. S. Kallman and S. P. Dijaili, "Quantitative Analysis of Integrated Optical Waveguide Spectrometers", *IEEE Photonics Technology Letters*, Vol. 6, No. 2, pp. 242-244, Feb. 1994.

[31]. Dietrich Marcuse, "Tilt, Offset and End-Seperation Loss of Lowest-Order Slab Waveguide Mode", *Journal of Lightwave Technology*, Vol. LT-4, No. 11, pp. 1647-1650, Nov. 1986.

[32]. Shaikh Iqbal Hosain, Jean-Pierre Meunier and Zi Hua Wang, "Coupling Efficiency of Butt-Jointed Planar Waveguides with Simultaneous Tilt and Transverse Offset", *Journal of Lightwave Technology*, Vol. 14, No. 5, pp. 901-907, May 1996.

[33]. Rober J Deri, and Eli Kapon, "Low-Loss III-V Semiconductor Optical Waveguides", *IEEE Journal of Quantum Electronics*, Vol. 27, No. 3, March 1991.

[34]. M. A. Cowin, M. Owen, I. H. White, and R. V. Penty, "Polymeric Wavelength Division Multiplexer", *Electronics Letters*, Vol. 35, No. 17, pp. 1464-1465, Aug. 1999.

[35]. Katsunari Okamoto, *Fundamentals of Optical Waveguides*, Ch. 2, Academic Press, 2000.

[36]. H. A. Haus, *Waves and Fields in Optoelectronics*, Ch. 4, Englewood Cliffs, Prentice Hall, N. J., 1984.

[37]. M. R. Amersfoort, J. B. D. Soole, H. P. LeBlanc, N. C. Andreadakis, A. Rajhel and C. Caneau, "Passband Broadening of Integrated Arrayed Waveguide Filters Using Multimode Interference Couplers", *Electronic Letters*, Vol. 32, No. 5, pp. 449-451, Feb. 1996.

[38]. K. Okamoto and A. Sugita, "Flat Spectral Response Arrayed-Waveguide Grating Multiplexer with Parabolic Waveguide Horns", *Electronic Letters*, Vol. 32, No. 18, pp. 1661-1662, Aug. 1996.

[39]. C. Dragone, T. Strasser, G. A. Bogeert, L. W. Stulz and P. Chou, "Waveguide Grating Router with Maximally Flat Passband Produced by Spatial Filtering", *Electronic Letters*, Vol. 33, No. 15, pp. 1312-1333, July 1997.

[40]. Michael C. Parker and Stuart D. Walker, "A Fourier-Fresnel Integral-Based Transfer Function Model for a Near-Parabolic Phase Profile Arrayed-Waveguide Grating", *IEEE Photonics Technology Letters*, Vol. 11, No. 8, pp. 1018-1020, Aug. 1999.

[41]. Y. P. Ho, H. Li and Y. J. Chen, "Flat Channel-Passband-Wavelength Multiplexing and Demultiplexing Devices by Multiple-Rowland-Circle Design", *IEEE Photonics Technology Letters*, Vol. 9, No. 3, pp. 342-344, March 1997.

[42]. C. Dragone, "Planar 1xN Optical Multiplexer with Nearly Ideal Response", *IEEE Photonics Technology Letters*, Vol. 14, No. 11, pp. 1545-1547, Nov. 2002.

[43]. M. Oguma, T. Kitoh, K. Jinguji, T. Shibata, A. Himeno and Y. Hibino, "Passband-Width Broadening Design for WDM Filter with Lattice-Form Interleave Filter and Arrayed-Waveguide Gratings", *IEEE Photonics Technology Letters*, Vol. 14, No. 3, pp. 328-330, March 2002.

[44]. E. G. Churin and P. Bayvel, "Passband Flattening and Broadening Techniques for High Spectral Efficiency wavelength Demultiplexers", *Electronic Letters*, Vol. 35, No. 1, pp. 27-28, Jan. 1999.

[45]. Zhiming Shi and Sailing He, "A Three-Focal-Point Method for the Optimal Design of a Flat-Top Planar Waveguide Demultiplexer", *IEEE Journal of Selected Topics in Quantum Electronics*, Vol. 8, No. 6, pp. 1179-1185, Nov./Dec. 2002.

[46]. C. Wei, J. Haes, I. Moerman, R. Baets and M. K. Smit, "Elliptic Waveguide Beam Focusing and Collimating Elements in InP: Analysis and Experiment", *Electronic Letters*, Vol. 31, No. 25, pp. 2168-2169, Dec. 1995.

[47]. A. Fenner Milton and William K. Burns, "Mode Coupling in Optical Waveguide Horns", *IEEE Journal of Quantum Electronics*, Vol. QE-13, No. 10, pp. 828-835, Oct. 1977.

[48]. "Processing Procedures for Dry-Etch Cyclotene Advanced Electronics Resins (Dry-Etch BCB)", Dow Chemical, Midland, MI, Form No. 618-00200-498 SMG, Nov. 1997.

[49]. "Processing Procedures for Cyclotene™ 4000 Series Photo BCB Resins: Immersion Develop Process", Dow Chemical, Midland, MI, April 2001.

[50]. Cyclotene Home. (March 2003). Transmission Spectrum Graph. Available: http://www.dow.com/cyclotene/over/graph3.htm.

[51]. Cyclotene Home. (March 2003). Infrared Spectrum. Available: http://www.dow.com/cyclotene/over/infra.htm.

[52]. Casey F. Kane and Robert R. Krchnavek, "Processing and Characterization of Benzocyclobutene Optical Waveguides", *IEEE Transactions on Components, Packaging, and Manufacturing Technology - Part B*, Vol. 18, No. 3, pp. 565-571, Aug. 1995.

[53]. Cyclotene Home. (Aug. 2001). Refractive Index vs. Wavelength. Available: http://www.dow.com/cyclotene/over/refra.htm.

[54]. R. Moosburger and K. Petermann, "4×4 Digital Optical Matrix Switch Using Polymeric Oversized Rib Waveguides", *IEEE photonics Technology Letters*, Vol. 10, No. 5, pp. 684-686, May 1998.

[55]. S. Wolff, A. Grosse, H. - J. Schimper, A. R. Giehl, M. Kuhnke, R. Grote, and H. Fouckhardt, "Technology and Realization of Metallic Curved Waveguide Mirrors in Polymer Film Waveguides Based on Anisotropic Plasma Etching", *Journal of Vacuum Science and Technology, A*, Vol. 19, No. 1, pp. 87-89, Jan./Feb. 2001.

[56]. Mothi Madhan Raj, Shunsuke Toyoshima and Shigehisa Arai, "Multiple Micro-Cavity Laser with Benzocyclobutene/Semiconductor High Reflective Mirrors Fabricated by CH_4/H_2-Reactive Ion Etching", *Japanese Journal of Applied Physics, part 2*, Vol. 38, No. 7B, pp. L811-L814, July 1999.

[57]. "Processing Procedures for Adhesion Promoters Used with Photosensitive and Dry-Etch Cyclotene Advanced Electronics Resins", Dow Chemical, Midland, MI, Form No. 618-00201-498 SMG, Nov. 1997.

[58]. Phillip E. Garrou, W. Boyd Rogers, Dan M. Scheck, Andrew J. G. Strandjord, Yasu Ida and Kaoru Ohba, "Stress-Buffer and Passivation Processes for Si and GaAs IC's and Passive Components Using Photosensitive BCB: Process Technology and Reliability Data", *IEEE Transactions on Advanced Packaging*, Vol. 22, No. 3, Aug. 1999.

[59]. Michael Schier, "Reactive Ion Etching of Benzocyclobutene Using a Silicon Nitride Dielectric Etch Mask", *Journal of Electrochemical Society*, Vol. 142, No. 9, pp. 3238-3240, Sept. 1995.

[60]. Robert D. Tacita and Christoph Steinbrüchel, "Patterning of Benzocyclobutene by Reactive Ion Etching", *Journal of Electrochemical Society*, Vol. 143, No. 8, pp. 2695-2697, Aug. 1996.

[61]. Kyung W. Paik, Herbert S. Cole, Richard J. Saia and John J. Chera, "Studies on Metal/Benzocyclobutene (BCB) Interface and Adhesion", *Journal of Adhesion Science and Technology*, Vol. 7, No. 5, pp. 403-415, 1993.

[62]. Chan Kai Chong, Cheong Chu Peng, Lee Guat Ngoh and Mary Teo. (May 2003). Cure Behaviour and Interfacial Adhesion of a Photo-sensitive BCB. MicroFab Technology (S) Pet. Ltd., Singapore. [Online]. Available: http://www.microfabtech.com/icep.pdf.

[63]. Percy B. Chinoy, "Reactive Ion Etching of Benzocyclobutene Polymer Films", *IEEE Transactions on Components, Packaging, and Manufacturing Technology - Part C*, Vol. 20, No. 3, pp. 199-206, July 1997.

[64]. M. R. Baklanov, S. Vanhaelemeersch, H. Bender and K. Maex, "Effects of Oxygen and Fluorine on the Dry Etch Characteristics of Organic Low-*k* Dielectrics", *Journal of Vacuum Science and Technology, B*, Vol. 17, No. 2, pp. 372-379, March/April 1999.

[65]. Steven A. Vitale, Heeyeop Chae and Herbert H. Sawin, "Etching Chemistry of Benzocyclobutene (BCB) low-*k* Dielectric Films in F_2+O_2 and Cl_2+O_2 High Density Plasmas", *Journal of Vacuum Science and Technology, A*, Vol. 18, No. 6, pp. 2770-2778, Nov./Dec. 2000.

[66]. R. J. Shul, C. T. Sullivan and G. B. McClellan, "Anisotropic ECR Etching of Benzocyclobutene", *Electronics Letters*, Vol. 31, No. 22, pp. 1919-1920, Oct. 1995.

[67]. John H. Keller, "Inductive Plasmas for Plasma Processing", *Plasma Sources Science and Technology*, Vol.5, pp. 166-172, 1996.

[68]. Martin J. Walke. (May 2003). Comparison of Bosch and Cryogenic Processes for Patterning High Aspect Ratio Features in Silicon. Oxford Instruments Plasma Technology, UK. [Online]. Available: http://www.oxford-instruments.com/pdf/spie2.pdf

[69]. Navnit Agarwal, Shom Ponoth, Joel Plawsky and P. D. Persans, "Optimized Oxygen Plasma Etching of Polyimide Films for Low Loss Optical Waveguides", *Journal of Vacuum Science and Technology, A*, Vol. 20, No. 5, pp. 1587-1591, Sept./Oct. 2002.

[70]. Marc J. Madou, *Fundamentals of Microfabrication: the Science of Miniaturization*, 2nd Edition, Ch. 6, CRC Press 2002.

[71]. "Cure and Oxidation Measurement for Cyclotene Advanced Electronics Resins", Dow Chemical, Midland, MI, Form No. 618-00219C-198.

[72]. Casey F. Kane and Robert R. Krchnavek, "Benzocyclobutene Optical Waveguides", *IEEE Photonics Technology Letters*, Vol. 7, No. 5, pp. 535-537, May 1995.

[73]. René M. de Ridder, Kerstin Wörhoff, Alfred Driessen, Paul V. Lambeck and Hans Albers, "Silicon Oxynitride Planar Waveguiding Structures for Application in Optical Communication", *IEEE Selected Topics in Quantum Electronics*, Vol. 4, No. 6, pp. 930-937, Nov./Dec. 1998.

[74]. Kerstin Wörhoff, Paul V. Lambeck and Alfred Driessen, "Design, Tolerance Analysis, and Fabrication of Silicon Oxynitride Based Planar Optical Waveguides for Communication Devices", *Journal of Lightwave Technology*, Vol. 17, No. 8, pp. 1401-1407, Aug. 1999.

[75]. T. Börner and K. P. Papathanassiou, "A Model-Based Analysis of Surface Scattering Effects in Polarimetric SAR Interferometry", in Proc. EUSAR 1998 (European Conference on Synthetic Aperture Radar), pp. 61-64.

[76]. Frank Elsholz. (June 2003). Rough Surface Characterization and Determination of the rms Roughness from Coherent Light Scattering. Technische Universität

Berlin, Germany. [Online]. Available: http://wwwnlds.physik.tu-berlin.de/~elsholz/speckle.pdf.

[77]. E. I. Thorsos, "The Validity of the Kirchhoff Approximation for Rough Surface Scattering Using a Gaussian Roughness Spectrum", *Journal of the Acoustical Society of America*, Vol. 83, No.1, pp. 78-92, Jan. 1988.

[78]. Y. Kuga and P. Phu, "Experimental Studies of Millimeter-Wave Scattering in Discrete Random Media and From Rough Surfaces", *Progress in Electromagnetic Research*, Vol. 14, pp. 37-88, 1996.

[79]. K. A. McGreer, "Diffraction from Concave Gratings in Planar Waveguides", ", *IEEE Photonics Technology Letters*, Vol. 7, No. 3, pp. 324-326, March 1995.

[80]. K. A. McGreer, "Theory of Concave Gratings Based on a Recursive Definition of Facet Positions", *Applied Optics*, Vol. 35, No. 30, pp. 5904-5910, Oct. 1996.

[81]. Reinhard März and Cornelius Cremer, "On the Theory of Planar Spectrographs", *Journal of Lightwave Technology*, Vol. 10, No. 12, pp. 2017-2022, Dec. 1992.

[82]. Michael S. Borella, Jason P. Jue, Dhritiman Banerjee, Byrav Ramamurthy and Biswanath Mukherjee, "Optical Components for WDM Lightwave Networks", *Proceedings of the IEEE*, Vol. 85, No. 8, pp. 1274-1307, Aug. 1997.

[83]. Corrado Dragone, "Theory of Wavelength Multiplexing with Rectangular Transfer Functions", *IEEE Journal of Selected Topics on Quantum Electronics*, Vol. 8, No. 6, pp. 1168-1178, Nov./Dec. 2002.

[84]. M. K. Smit and Cor van Dam, "PHASAR-Based WDM-Devices: Principles, Design and Application", *IEEE Journal of Selected Topics on Quantum Electronics*, Vol. 2, No. 2, pp. 236-250, June 1996.

[85]. Yoshinori Hibino, "Recent Advances in High-Density and Large-Scale AWG Multi/Demultiplexers with Higher Index-Contrast Silica-Based PLCs", *IEEE Journal of Selected Topics on Quantum Electronics*, Vol. 8, No. 6, pp. 1090-11101, Nov./Dec. 2002.

[86]. Yuzo Yoshikuni, "Semiconductor Arrayed Waveguide Gratings for Photonic Integrated Devices", *IEEE Journal of Selected Topics on Quantum Electronics*, Vol. 8, No. 6, pp. 1102-1114, Nov./Dec. 2002.

[87]. Stamatios V. Kartalopoulos, *Introduction to DWDM technology: Data in a Rainbow*, SPIE Optical Engineering Press, Bellingham, Washington, 2000.

[88]. Louay Eldada, "Advances in Telecom and Datacom Optical Components", *Optical Engineering*, Vol. 40, No. 7, pp. 1165-1178, July 2001.

[89]. Louay Eldada and Lawrence W. Shacklette, "Advances in Polymer Integrated Optics", *IEEE Journal of Selected Topics on Quantum Electronics*, Vol. 6, No. 1, pp. 54-68, Jan./Feb. 2000.

[90]. Jae-Wook Kang, Joon-Sung Kim and Jang-Joo Kim, "Optimized Oxygen Plasma Etching of Polycarbonate for Low-Loss Optical Waveguide Fabrication", *Japanese Journal of Applied Physics, part 1*, Vol. 40, No. 5A, pp. 3215-3219, May 2001.

[91]. J. H. Kim, E. J. Kim, H. C. Choi, C. W. Kim, J. H. Cho, Y. W. Lee, B. G. You, S. Y. Yi, H. J. Lee, K. Han, W. H. Jang, T. H. Rhee, J. W. Lee, S. J. Pearton, "Evaluation of Fluorinated Polyimide Etching Processes for Optical Waveguide Fabrication", *Thin Solid Films*, Vol. 341, pp. 192-195, 1999.

[92]. Paul Werbaneth "Optimizing Plasma Etch for MEMS Devices", *Solid State Technology*, pp. 135-142, June 2001.

[93]. W. Scot Ruska, *Microelectronic Processing: an Introduction to the Manufacture of Integrated Circuits*, Ch. 6, McGraw-Hill, 1987.

Appendix A. Characterization and Numerical Generation of Random Rough Surfaces

Two parameters, the Root Mean Square (RMS) height *RMS* and the correlation length *CL*, are used to describe the statistical properties of one-dimensional random rough surface $h(x)$, where h is the surface height at position x [75]. The zero-order parameter [76], surface RMS height *RMS*, is defined as

$$RMS = \sqrt{\int \left(h - \bar{h}\right)^2 P(h)dh}\,, \tag{A-1}$$

where $\bar{h}$ is the average surface height and $P(h)$ is the surface height probability distribution function, which is normalized so that

$$\int P(h)dh = 1. \tag{A-2}$$

$P(h)$ is a first-order parameter [76] and its physical meaning is that the probability for a point to have a surface height between h and $h+dh$ is $P(h)dh$. Different probability distribution functions are used for different engineering surfaces. However, the most simple and often used assumption is a Gaussian distribution function in the form of

$$P(h) = \frac{1}{\sqrt{2\pi}RMS}\exp\left(-\frac{h^2}{2RMS^2}\right). \tag{A-3}$$

The first-order parameter only gives information about the statistics at individual positions. To reflect the correlation between two different points on a random rough surface, a second-order parameter [76], the height-height correlation function $C(\tau)$, is defined as

$$C(\tau) = \int h(x+\tau)h^*(x)dx\,, \tag{A-4}$$

where * is the complex conjugation operator. The correlation function describes the spatial coherence between two points on the rough surface separated by a

distance τ. When two points are closer (smaller τ) the correlation between them is stronger. Again, several different correlation functions are used but the most widely used is the Gaussian correlation function

$$C(\tau) = RMS^2 \exp\left(-\frac{\tau^2}{CL^2}\right), \tag{A-5}$$

where the correlation length CL is the distance at which two surface points can not be considered correlated anymore. Statistically, CL is the equivalent to the average "period" of the rough surface.

The power spectral density function $W(s)$ describes the average distribution of each spatial frequency component s of the randomly fluctuated surface profile. $W(s)$ is the Fourier transform of the correlation function $C(\tau)$, and for the Gaussian correlation function,

$$W(s) = \frac{1}{2\pi}\int C(\tau)\exp(-is\tau)d\tau = \frac{RMS^2}{2\sqrt{\pi}}\exp\left(-\frac{s^2 \cdot CL^2}{4}\right). \tag{A-6}$$

The Fourier transform of the surface height function $h(x)$ is

$$F(s) = \frac{1}{2\pi}\int h(x)\exp(-isx)dx. \tag{A-7}$$

From Eqs. (A-4) and (A-6), the power spectral density function $W(s)$ is related to $F(s)$ as

$$W(s) = |F(s)|^2. \tag{A-8}$$

If the power spectral density function $W(s)$ is known, the surface height function $h(x)$ can be calculated with the inverse Fourier transform of $F(s)$ using the spectral method [77],

$$h(x) = \frac{1}{2\pi}\int \sqrt{W(s)}\,\frac{N(0,1)+iN(0,1)}{\sqrt{2}}\exp(isx)ds, \tag{A-9}$$

where $N(0, 1)$ is a normally distributed random number in the range of (0, 1). The random complex term in the above equation modulates the phase of the Fourier

coefficients and governs the first-order statistics of the random surface. The second-order statistics are governed by forcing the magnitude of the Fourier spectrum to follow the surface spectrum $\sqrt{W(s)}$.

For numerical generation of N+1 evenly spaced random rough surface points with a total surface length SL, the Discrete Fourier Transform (DFT) is applied to Eq. (A-9) and the following equations can be obtained [78]:

$$h(x_n) = \frac{1}{SL} \sum_{n=-\frac{N}{2}}^{\frac{N}{2}} T(s_n) \exp(i s_n x_n), \tag{A-10}$$

where N is an even integer and

$$T(s_n) = \sqrt{2\pi \cdot SL \cdot W(s_n)} \begin{cases} \dfrac{N(0,1) + iN(0,1)}{\sqrt{2}}, n \neq 0, \pm\dfrac{N}{2} \\ N(0,1), n = 0, \pm\dfrac{N}{2} \end{cases}, \tag{A-11}$$

$$x_n = \frac{SL}{N} n, \tag{A-12}$$

$$s_n = \frac{2\pi n}{SL}, \tag{A-13}$$

$$W(s_n) = \frac{RMS^2 \cdot CL}{2\sqrt{\pi}} \exp\left(-\frac{s_n{}^2 \cdot CL^2}{4} \right). \tag{A-14}$$

To generate a real sequence, the Fourier coefficient $T(s_n)$ in Eq. (A-10) must satisfy the requirement

$$T(s_n) = T^*(-s_n). \tag{A-15}$$

It is also required that the total surface length $SL > 5CL$ to avoid spectral aliasing [78]. The requirement in Eq. (A-15) is satisfied by using a normally distributed random sequence of a length of N-1 for the N/2 positive frequency components s_n. The random sequence is then flipped left-to-right and applied to the N/2 negative frequency components s_n. The normally distributed random sequence can be generated with the Matlab function *randn*, which generates pseudorandom

numbers in the range of (0, 1) with a Gaussian (i.e., normal) distribution. The generated pseudorandom numbers are repeatable and their sequence is determined by the *state* of the random number generator *randn*. A large number N is required to generate a random sequence with good statistic properties.

Assuming a Gaussian correlation function and a Gaussian power spectral density function, the random rough surface generator is implemented in Matlab using Eqs. (A-10) to (A-14). An example of the generated rough surface is shown in Fig. A-1 for $RMS = 1$, $CL = 3$, $SL = 30$ and $N = 200$. In simulating the surface roughness effect for grating DMUX, the random rough surface generator was called for each grating facet to generate N+1 surface points. The random variations were then individually added to the N+1 sample points on each original facet. After one set of roughness parameters was simulated for all facets, the *state* of the random number generator *randn* was returned to zero so that the random pattern can be repeated for another set of roughness parameters.

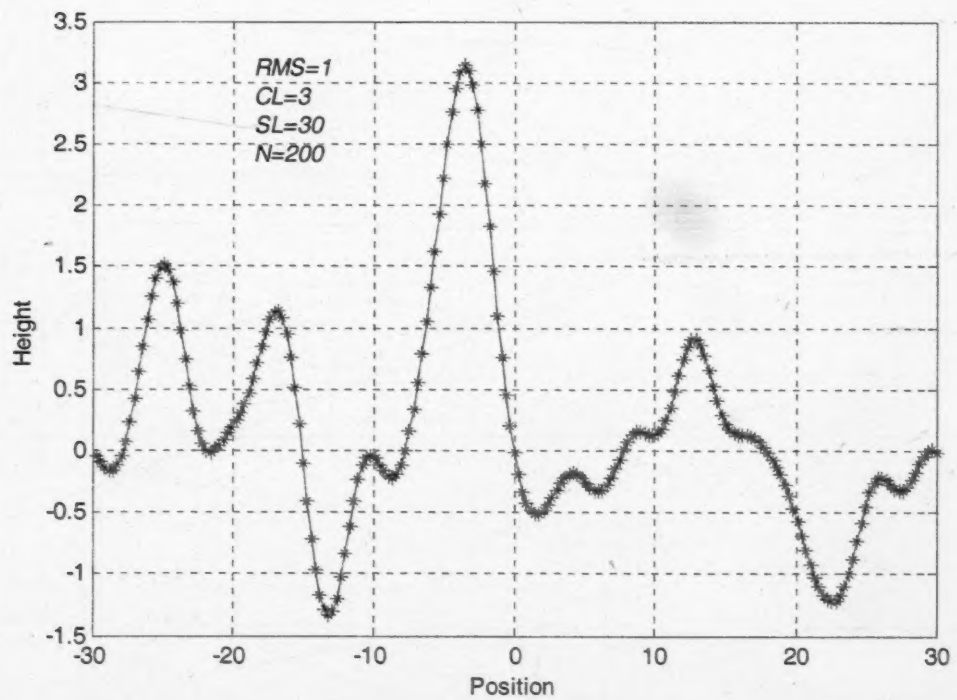

Fig. A-1. An example of random rough surface generated with spectral method.

Appendix B. Numeric Solutions of Electromagnetic Field in Optical Waveguides

Following Ref. [35], for homogenous and lossless dielectric medium, the Maxwell's equations can be written in the following form for the time (t) varying electric field $\tilde{\boldsymbol{E}}$ and magnetic field $\tilde{\boldsymbol{H}}$:

$$\begin{cases} \nabla \times \tilde{\boldsymbol{E}} = -\mu \dfrac{\partial \tilde{\boldsymbol{H}}}{\partial t} \\ \nabla \times \tilde{\boldsymbol{H}} = \varepsilon \dfrac{\partial \tilde{\boldsymbol{E}}}{\partial t} \end{cases}, \tag{B-1}$$

where ε and μ are the permittivity and permeability of the medium, respectively. For plane-wave propagating along the z-axis of the x-y-z coordinate system shown in Fig. B-1, which overlaps with the x_i-z_i coordinate system in Fig. 4-1, the fields can be expressed as

$$\begin{cases} \tilde{\boldsymbol{E}} = \boldsymbol{E}(x, y)\exp(i\varpi t - \beta z) \\ \tilde{\boldsymbol{H}} = \boldsymbol{H}(x, y)\exp(i\varpi t - \beta z) \end{cases}, \tag{B-2}$$

where β is the propagation constant and $\varpi = 2\pi c/\lambda$ is the angular frequency, with c as the light speed in vacuum and λ as the optical wavelength in vacuum.

Taking the slab approximation, which assumes that the electromagnetic field $\boldsymbol{E}$ and $\boldsymbol{H}$ have no z-axis dependency, the following two sets of solutions to the Maxwell's equations can be obtained:

$$\begin{cases} \dfrac{d^2E_y}{dx^2} + \left(k^2 n_1^{\,2} - \beta^2\right)E_y = 0 \\ H_x = \dfrac{-\beta E_y}{\varpi\mu_0} \\ H_z = \dfrac{i}{\varpi\mu_0}\cdot\dfrac{dE_y}{dx} \\ E_x = E_z = H_y = 0 \end{cases} \quad , \tag{B-3}$$

for TE modes and

$$\begin{cases} \dfrac{d}{dx}\left(\dfrac{dH_y}{n_1^{\,2}dx}\right) + \left(k^2 - \beta^2 / n_1^{\,2}\right)H_y = 0 \\ E_x = \dfrac{\beta H_y}{\varpi\varepsilon_0 n_1^{\,2}} \\ E_z = \dfrac{-i}{\varpi\varepsilon_0 n_1^{\,2}}\cdot\dfrac{dH_y}{dx} \\ H_x = H_z = E_y = 0 \end{cases} \tag{B-4}$$

for TM modes, where $k = \varpi/c$ is the wavenumber in vacuum, ε_0 and μ_0 are the permittivity and permeability of vacuum, respectively, and n_1 is the refractive index of the waveguide core material.

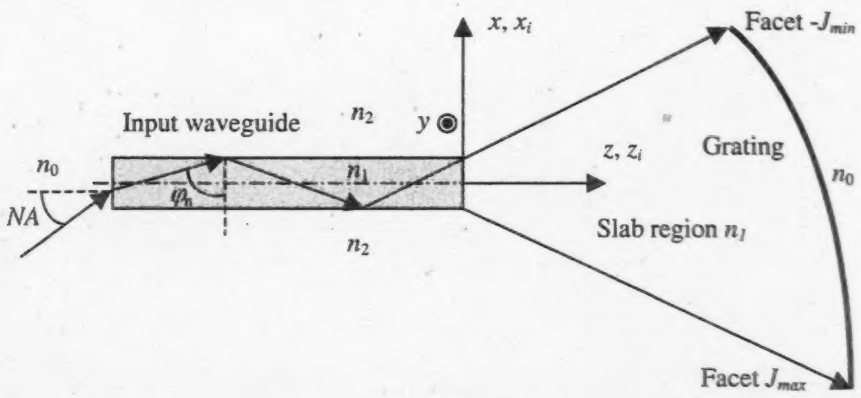

Fig. B-1. Geometry of elliptic grating DMUX used for field calculation.

Based on the fact that the guided fields are confined in the core region and have exponentially decaying tails in the cladding, the horizontal TE mode fields in the symmetric input waveguide can be expressed as

$$E_{in}(x_i^{\,i},0)=\begin{cases}\cos(\kappa W/2-\phi)\cdot e^{-\sigma\left(x_i^{\,i}-W/2\right)}, & \left(\left|x_i^{\,i}\right|>W/2\right)\\ \cos\left(\kappa x_i^{\,i}-\phi\right), & \left(\left|x_i^{\,i}\right|\le W/2\right)\end{cases}, \tag{B-5}$$

where $\phi=n\pi/2$ is the phase for TE_n mode, and W is the width of the input waveguide. κ and σ, the wavenumbers along the x-axis in the core and the cladding, respectively, are defined as

$$\begin{cases}\kappa=\sqrt{k^2 n_1^{\,2}-\beta^2}\\ \sigma=\sqrt{\beta^2-k^2 n_2^{\,2}}\end{cases}, \tag{B-6}$$

where n_2 is the refractive index of the cladding material. The following eigenvalue equation must be satisfied to make the electromagnetic field components E_y and H_z continuous at the boundaries of the core-cladding interfaces ($x=\pm W/2$):

$$\upsilon\sqrt{1-b}=\frac{n\pi}{2}+\tan^{-1}\left(\sqrt{\frac{b}{1-b}}\right), \tag{B-7}$$

where

$$\upsilon=k\frac{W}{2}\sqrt{n_1^{\,2}-n_2^{\,2}} \tag{B-8}$$

is the normalized frequency, and b is the normalized propagation constant defined as

$$b=\frac{n_e^{\,2}-n_2^{\,2}}{n_e^{\,2}-n_2^{\,2}}, \tag{B-9}$$

where $n_e=\beta/k$ is the effective mode index. Using the normalized b and υ, the wavenumbers κ and σ can be rewritten as

$$\begin{cases} \kappa = 2v\sqrt{1-b}/W \\ \sigma = 2v\sqrt{b}/W \end{cases} \tag{B-10}$$

Once the waveguide dimension W, the optical wavelength λ and the material indices n_1 and n_2 are determined, the normalized propagation constant b can be numerically solved using Eq. (B-7) with a numerical method such as the simple bisection method. Any solution of b within the range of (0, 1) constitutes one guided TE mode. Then the horizontal TE mode fields in the input waveguide can be obtained with Eqs. (B-10) and (B-5).

The incident angle φ_n at the core-cladding interface of the input waveguide for the horizontal TEn mode can be obtained by numerically solving the following equation [35]:

$$\tan\left(kn_1 \cos\varphi_n - \frac{n\pi}{2}\right) = \sqrt{\frac{2\Delta}{\cos^2\varphi_n} - 1}\,, \tag{B-11}$$

where Δ is the index contrast of the waveguide materials as defined in Eq. (2-5).

Appendix C. Processing Parameters for DMUX Fabrication in BCB Polymers

The fabrication of DMUXes in BCB polymers using DRIE was conducted in the NanoFab of the University of Alberta. The overall processing procedures for device fabrication and the processing parameters for DRIE of BCB polymers are discussed in Section 5.1.2 and Section 5.1.3, respectively. The following shows details of other processing parameters.

Wafer Cleaning with Piranha

Piranha is a solution of 3:1 sulfuric acid (H_2SO_4) and hydrogen peroxide (H_2O_2) used to remove organic materials on surface of silicon wafers. Each wafer was cleaned by submersion in Piranha solution for 15 *min*, and then rinsed with DI water and dried with nitrogen gas flow. It was then baked at 220 $^{\circ}C$ for 1 *hr* in an oven to drive out moisture.

Application of Adhesion Promoter AP3000

The interface between BCB polymers and underlying layers such as metals, silicon substrate and other polymers usually requires a surface treatment to enhance adhesion. Adhesion promoter AP3000 is a product of Dow Chemical used for BCB polymers [57]. A 0.5 μm filter was used before application to remove particles in the solution. Approximately 4 *ml* of AP3000 solution was dynamically dispensed on the center of a 4 *in* silicon wafer while it was spinning at around 50 *rpm*. The solution was allowed to spread over the wafer at a spinning speed of around 500 *rpm* for 10 *s*. A spinning speed of around 3000 *rpm* was then used to spin-dry the wafer for 50 *s*.

Coating of Dry-Etch BCB Polymer

Dry-etch BCB polymer Cyclotene 3022-63 was dynamically dispensed on the center of a wafer while spinning at around 100 *rpm*, and was allowed to spread out at a spinning speed of 500 *rpm* for 20 *s*. The spinning speed was then increased to 5000 *rpm* in 10 *s* and kept for 30 *s* to get a final film thickness of around 10 μm. The spinning speed was then reduced to 400 *rpm* and polymer solvent T1100 was applied for 5 *s* at the edge of the wafer to remove edge bead (thicker polymer formed at the edge of the wafer). After the edge bead removal, the spinning speed was increased to 1500 *rpm* in 5 *s* and kept for 20 *s* to spin-dry the wafer.

After the polymer coating, the wafer was put in a vacuum oven at room temperature. A gradual temperature change was used in thermal curing of the polymer to avoid thermal stress. The oven was first pumped down to vacuum with wafers inside and its temperature was ramped to 50 °*C* in 40 *min*. After 5 *min* of soaking, the temperature was ramped to 100 °*C* in 30 *min*, followed by soaking of 15 *min*, ramping to 145 °*C* in 40 *min*, and soaking of 15 *min*. The oven was then ramped to a final temperature of 210 °*C* in 40 *min* and soaked for 40 *min*. The oven was allowed to naturally cool down to 160 °*C* in approximately 30 *min*, and the wafers were then taken out and were allowed to cool down in atmosphere. This procedure resulted in partial curing of the dry-etch BCB polymer for good adhesion to the subsequent layer of photo BCB polymer.

Coating of Photosensitive BCB Polymer

Photosensitive BCB polymer Cyclotene 4024-40 has a shelf life of 1 year if stored in a freezer at -15 °*C*. The shelf life is only 7 days if stored in clean room at 20 °*C* [49]. The polymer was stored in a freezer before use and was allowed to equilibrate to -4 °*C* in a refrigerator over night, and to equilibrate to room temperature in 1 *hr*.

The polymer solution was dynamically dispensed on the center of a wafer spinning at 50 *rpm* and was allowed to spread out at a spinning speed of 500 *rpm* for 10 *s*. The spinning speed was then increased to 1500 *rpm* in 5 *s* and kept for 30 *s* to obtain a film thickness of 10.2 μm after soft baking. The spinning speed was reduced to 600 *rpm* to remove edge bead with solvent T1100. The wafer was then spin-dried at 1200 *rpm* for 20 *s* with a ramping time of 5 *s*.

After polymer coating, the wafer was soft-baked at 75 °*C* for 90 *s* on a hot plate. It was then exposed in a photolithography mask aligner for 20 *s* without mask. UV dose for the photo BCB 4024 is 25 mJ/cm^2 per μm of pre-exposure thickness [49] based on broadband exposure at I-line (365 *nm*). At the 1500 *rpm* spinning speed used, the pre-exposure thickness of BCB4024-40 is 10.2 μm [49]. The calibrated average exposure intensity of the photolithography mask aligner used is 30.7 mW/cm^2 at the I-line and the exposure factor is 0.5608. So the exposure time can be calculated as

$$\frac{(25mJ/cm^2/\mu m)\times 10.2\mu m}{(30.7mW/cm^2)\cdot 0.5608} = 14.8s.$$

An actual exposure time of 20 *s* was used to over-cure the polymer.

After exposure, the wafer was put in a vacuum oven that was then pumped down to vacuum at room temperature. The oven temperature was increased to 150 °*C* in 50 *min*, and the wafer was soaked at this temperature for 15 *min*. It was then ramped to 250 °*C* in 1 *hr* and soaked for 1 *hr* to fully cure both the dry-etch BCB polymer and the photo BCB polymer. The wafer was then left in the oven under vacuum to allow natural cool down to room temperature over night.

Sputtering of Aluminum Films

Approximately 300 *nm* thick *Al* thin films were used as the dry-etch mask for BCB polymers. *Al* was sputtered at a chamber base pressure of 1.4×10^{-6} *Torr* and a sputtering pressure of 7.0×10^{-3} *Torr* with an argon gas flow of 10 *sccm*. The

sputtering power was 300 *W*, and the measured voltage was 399 *V*. A sputtering time of 45 *min* was used with a burn-in sputtering of 4 *min*.

Mask Patterning with Positive Photolithography and Wet Etching

The photoresist HPR 504 was dynamically dispensed and spread on top of *Al* thin films at a spinning speed of 500 *rpm* for 10 *s*, and was then spun at 4000 *rpm* for 40 *s* to obtain a resist thickness of around 1 μm. The resist was then baked at 115 $^{\circ}C$ for 90 *s* in a hot plate under vacuum and exposed with mask in the I-line mask aligner for 4 *s* using contact exposure, and subsequently developed in developer Microposit 354. It was then hardened with a post-baking at 120 $^{\circ}C$ for 30 *min* in oven.

After photolithography, the *Al* films were patterned with wet chemical etching using a standard microelectronic grade *Al* etchant. The photoresist was then stripped with acetone.